이학박사 학위논문

Semiclassical Boltzmann transport theory for anisotropic, multi-band systems and its application in Dirac materials

비등방, 다층구조 물질에 적용가능한 준고전적인 볼츠만 수송 이론 및 디락 물질에서의 응용

2021년 8월

서울대학교 대학원

물리천문학부

박상현

Semiclassical Boltzmann transport theory for anisotropic, multi-band systems and its application in Dirac materials

비등방, 다층구조 물질에 적용가능한 준고전적인 볼츠만 수송 이론 및 디락 물질에서의 응용

지도교수 민홍기

이 논문을 이학박사 학위논문으로 제출함

2021년 8월

서울대학교 대학원

물리천문학부

박상현

박상현의 박사 학위논문을 인준함

2021년 8월

위 원 장 _____

부 위 원 장 _____

위 원 _____

위 원 _____

위 원 _____

Abstract

Topologiacal semimetals are novel materials that exhibit many fascinating properties, and they are at the center of the spotlight in the condensed matter physics studies, as their electronic structure near the band touching point gives rise to the unique quasiparticles that does not follow the Drude model of free electrons. Furthermore, their topological nature assures that such quasiparticles are robust against small perturbations, making them great platforms to test various physical behaviors of those non-conventional excitations. With that motivations, this thesis is devoted to studying the semiclassical electronic transport and electron-mediated magnetism of Dirac materials.

First, we derive the semiclassical anisotropic multi-band Boltzmann transport equation that was extensively used throughout the thesis.

Then we turn to investigating the transport properties of multi-Weyl semimetals and the few-layer black phosphorus in various phases using anisotropic multi-band Boltzmann transport equation. Multi-Weyl semimetals are topological semimetals with anisotropic band dispersion (linear on one axis; nonlinear on the other two axes) and their chiral charge is larger than one. Black phosphorus is normally a semiconductor, but recent studies have shown that its band gap can be tuned to show multiple phases (insulator phase, semi-Dirac transition point, and Dirac phase). We studied these materials using anisotropic multi-band Boltzmann transport theory and discovered their characteristic chiral charge, band dispersion, and band gap sign signature on the carrier density-dependent and the temperature-dependent conductivity calculations.

We also examine the magnetic field effect on the semiclassical transport, as

the external magnetic field couples with the Berry curvature, it gives rise to the anisotropy when the system is isotropic.

Finally, we look into the Ruderman–Kittel–Kasuya–Yosida (RKKY) interaction in three-dimensional (3D) isotropic chiral semimetals to study the power-law effect on the charge carrier spin-mediated magnetism in 3D semimetals. We calculated the transition temperature and temperature- and power-law-dependent static susceptibilities, and discovered that the magnetic ordering of dilute magnetic impurities on 3D chiral semimetals are always ferromagnetic.

Keywords: electronic conductivity, semiclassical Boltzmann transport theory, few-layer black phosphorus, Weyl semimetals, multi-Weyl semimetals, RKKY interaction

Student Number: 2014-22366

Contents

List of Figures

Chapter 1

Introduction

We are used to studying a physical system as a simplified model. Making a model (or an assumption) that captures the essence of the system while minimizing the discrepancy between the model and the reality has always been the centerpiece of physics itself. The isotropic band dispersion assumption is one of them; the beauty and ease of the calculation made the isotropic band dispersion assumption into a de facto standard approach when we study any new condensed matter systems. In most cases, the isotropic band assumption is shown to be valid in wide range of materials near the band touching point. A case in point: the semiconductor physics, one of the most predominant applications of the transport studies that shaped the modern civilization, mostly uses a band-insensitive Drude formalism and garnered huge success.

However, when we have a tool that works tremendously well in some conditions, we may succumb to the pitfall of overly trusting it. In this case, the pitfall would be blindly using the isotropic formalism, even when the anisotropic band dispersion is fundamentally governing many physical phenomena such as charge

transport or optical behaviors, i.e. the band dispersion relation is not suitable for the isotropic effective model even at low Fermi energy.

Then when does this fundamental anisotropy prevail in the transport signature? There would be many examples, but the topological materials in general are great examples of anisotropic band dispersion relations as they have symmetry conditions that add in more complexity. On top of that, the symmetry conditions make the band crossing points robust against external perturbations, which means that such anisotropic band structure does not break down easily.

Topological materials include topological insulators and topological crystalline insulators [1, 2], and topological semimetals such as Weyl and Dirac semimetals [3, 4]. Higher-order topological insulator [5] is also recently suggested topological material.

We mainly focused on the topological semimetals, whose band crossing points are protected by various symmetry conditions. Multi-Weyl semimetals are Weyl semimetals with higher chiral charge, and their band crossing points, i.e. multi-Weyl points are protected by point-group symmetries [6].

We also studied the black phosphorus, which is an allotrope of phosphorus that is in sheet-like structure, stacked layer-by-layer with Van der Waals force [7, 8]. In few-layer black phosphorus, one of the most noticeable features is that their band gap size is tunable with various methods [9–20] and in some cases, even be inverted to create stable Dirac points.

Magnetic field-driven anisotropy in the semiclassical transport regime was also examined. In topological materials where a nonvanishing Berry curvature is present, the magnetic field couples with the Berry curvature and this coupling makes the isotropic analysis on the transport unsuitable.

With these motivations, we delve into the extended version of semiclassilcal Boltzmann transport theory with anisotropic, multi-band systems in mind and

demonstrate its capabilities in Dirac materials, where the band crossing point is protected by the symmetry conditions. We then sidetrack a little bit and study the dilute magnetic impurities in a hypothetical Dirac-like materials with arbitrary band dispersion power-law.

This thesis is organized as follows:

In chapter 2, we will briefly review the Boltzmann transport theory and introduce the anisotropic, multi-band extension of the relaxation time approximation.

In chapter 3, we look into the DC conductivity in multi-Weyl semimetals, which are topological semimetals with anisotropic energy dispersion relation. We calculate the conductivity using the formulations that developed above and show the characteristic density and temperature power-law dependence behavior for their conductivity.

In chapter 4, we study the DC conductivity in a few-layer black phosphorus with multi-band, anisotropic Boltzmann transport theory. Again, we calculate the conductivity and examine its Fermi energy, temperature power-law dependence. Additionally, we also consider how the phase of a few-layer black phosphorus that defined by the band-gap tuning parameter sign affects its transport signatures.

In chapter 5, we explore the magnetic field effect in the semiclassical transport equation and investigate the field-driven anisotropy. We formulate the anisotropic Boltzmann transport theory for the magnetotransport, and argue that the magnetic field-driven anisotropy necessitates the usage of anisotropic transport equation even when the original system is isotropic.

In chapter 6, we investigate the Ruderman–Kittel–Kasuya–Yosida (RKKY) interaction in magnetic impurities on a 3D chiral gas, which is a hypothetical extension of 3D Dirac-Weyl semimetals with arbitrary power-law relations. We

found that regardless of the power-law, RKKY magnetization of the magnetic impurities are ferromagnetic.

Finally in chapter 7, we conclude this thesis with a summary.

Chapter 2

Semiclassical Boltzmann transport theory

2.1 Boltzmann transport theory for isotropic, single-band non-magnetic systems

Semiclassical Boltzmann transport theory is essentially a theory of obtaining non-equilibrium distribution function when the external field (be it electric field, magnetic field, or thermal gradient) is applied to the system. The particles in a phase-space volume of $\Delta \boldsymbol{r} \Delta \boldsymbol{k}$ would be "transported" to the new phase-space volume $\Delta \boldsymbol{r}' \Delta \boldsymbol{k}'$ when the field is applied, but the collision between the particles (or impurities) would change the number of particles that were supposed to arrive at the destination in the phase space (some might be scattered out, while others might be scattered in). The charge carrier can be scattered from the impurities, other charge carriers, or phonons, but we mainly focus on the impurity scattering.

The Boltzmann equation is given by

$$\left(\frac{df}{dt}\right)_{\text{coll}} = \frac{\partial f}{\partial t} + \dot{\boldsymbol{r}} \cdot \nabla_{\boldsymbol{r}} f + \dot{\boldsymbol{k}} \cdot \nabla_{\boldsymbol{k}} f, \tag{2.1}$$

where f is the non-equilibrium distribution function, $\dot{\boldsymbol{r}} \cdot \nabla_{\boldsymbol{r}} f$ is the diffusion term, $\dot{\boldsymbol{k}} \cdot \nabla_{\boldsymbol{k}} f$ is the force term, and $\left(\frac{df}{dt}\right)_{\text{coll}}$ is the collision integral term.

When there is no thermal gradient or magnetic field present, the diffusion term vanishes. On top of that, if we assume that the total number of charge is invariant, then the time derivative term would vanish. Equation of motion of the Bloch electrons then can be simplified as

$$\left(\frac{df}{dt}\right)_{\text{coll}} = \dot{\boldsymbol{k}} \cdot \nabla_{\boldsymbol{k}} f_{\boldsymbol{k}}. \tag{2.2}$$

If we assume that $\boldsymbol{k}$ dependence only enters $f_{\boldsymbol{k}} = f_{\boldsymbol{k}}^{(0)} + g_{\boldsymbol{k}}$ ($g_{\boldsymbol{k}} \equiv f_{\boldsymbol{k}} - f_{\boldsymbol{k}}^{(0)}$, $f_{\boldsymbol{k}}^{(0)}$ is the equilibrium Fermi-Dirac distribution) via energy dispersion $\varepsilon(\boldsymbol{k})$ and ignoring the higher-order terms such as $\nabla_{\boldsymbol{k}} g_{\boldsymbol{k}}$, the right-hand side becomes

$$\dot{\boldsymbol{k}} \cdot \nabla_{\boldsymbol{k}} f \approx q\boldsymbol{E} \cdot \frac{\partial f_{\boldsymbol{k}}^{(0)}}{\hbar \partial \boldsymbol{k}} = q\boldsymbol{E} \cdot \boldsymbol{v}_{\boldsymbol{k}} \frac{\partial f_{\boldsymbol{k}}^{(0)}}{\partial \varepsilon_{\boldsymbol{k}}}, \tag{2.3}$$

where we have used $\dot{\boldsymbol{k}} = q\boldsymbol{E}$ for non-magnetic systems. Collision term $\left(\frac{df}{dt}\right)_{\text{coll}}$ is given by

$$\left(\frac{df}{dt}\right)_{\text{coll}} = -\int \frac{d^d k'}{(2\pi)^d} W_{\boldsymbol{k}\boldsymbol{k}'}(f_{\boldsymbol{k}} - f_{\boldsymbol{k}'}), \tag{2.4}$$

where d is the dimension of the system, $W_{\boldsymbol{k}\boldsymbol{k}'} = \frac{2\pi}{\hbar} n_{\text{imp}} |V_{\boldsymbol{k}\boldsymbol{k}'}|^2 \delta(\varepsilon_{\boldsymbol{k}} - \varepsilon_{\boldsymbol{k}'})$ is the transition rate from $\boldsymbol{k}$ to $\boldsymbol{k}'$ for an elastic impurity scattering (which was calculated from Fermi's golden rule) with the impurity potential $V_{\boldsymbol{k}\boldsymbol{k}'}$ and the impurity density n_{imp}.

In isotropic, single-band non-magnetic systems, we can use simple relaxation time approximation. Relaxation time approximation suggests that the non-equilibrium distribution function $f_{\boldsymbol{k}}$ relaxes back to equilibrium after time

$\tau_{\boldsymbol{k}}$ from the collision with the impurities, i.e. $-\frac{f_{\boldsymbol{k}}-f_{\boldsymbol{k}}^{(0)}}{\tau_{\boldsymbol{k}}} = -\frac{g_{\boldsymbol{k}}}{\tau_{\boldsymbol{k}}} = \left(\frac{df}{dt}\right)_{\text{coll}}$. From Eq. (2.3) and Eq. (2.4), we can see that

$$\begin{aligned} g_{\boldsymbol{k}} &= q\boldsymbol{E}\cdot\boldsymbol{v}_{\boldsymbol{k}}\tau_{\boldsymbol{k}}S^{(0)}(\varepsilon_{\boldsymbol{k}}) && (2.5)\\ \frac{1}{\tau_{\boldsymbol{k}}} &= \int\frac{d^dk'}{(2\pi)^d}W_{\boldsymbol{k}\boldsymbol{k}'}(1-\cos\theta_{\boldsymbol{k}\boldsymbol{k}'}), && (2.6)\end{aligned}$$

where $S^{(0)}(\varepsilon_{\boldsymbol{k}}) \equiv -\frac{\partial f_{\boldsymbol{k}}^{(0)}}{\partial\varepsilon_{\boldsymbol{k}}}$, and $\theta_{\boldsymbol{k}\boldsymbol{k}'}$ is the angle between $\boldsymbol{k}$ and $\boldsymbol{k}'$. Only the cosine term remains as the integral cancels out the $\boldsymbol{k}$-perpendicular parts (and we have assumed the isotropic, angle-independent energy dispersion $\varepsilon_{\boldsymbol{k}}$). The $(1-\cos\theta_{\boldsymbol{k}\boldsymbol{k}'})$ term also accounts for the forward- or backward-scattering balancing.

To calculate the conductivity, we now turn to current density equation

$$\boldsymbol{J} = gq\int\frac{d^dk}{(2\pi)^d}\dot{\boldsymbol{r}}f_{\boldsymbol{k}} = gq\int\frac{d^dk}{(2\pi)^d}\boldsymbol{v}_{\boldsymbol{k}}\left(f_{\boldsymbol{k}}^{(0)}+g_{\boldsymbol{k}}\right), \tag{2.7}$$

where g is the degeneracy factor. As the integral of $\boldsymbol{v}_{\boldsymbol{k}}f_{\boldsymbol{k}}^{(0)}$ vanishes, we get

$$\boldsymbol{J} = gq\int\frac{d^dk}{(2\pi)^d}\boldsymbol{v}_{\boldsymbol{k}}g_{\boldsymbol{k}} = gq^2\int\frac{d^dk}{(2\pi)^d}\boldsymbol{v}_{\boldsymbol{k}}\left(\boldsymbol{E}\cdot\boldsymbol{v}_{\boldsymbol{k}}\right)S^{(0)}(\varepsilon_{\boldsymbol{k}})\tau_{\boldsymbol{k}}. \tag{2.8}$$

From the Ohm's law, i.e. $\boldsymbol{J} = \sigma\boldsymbol{E}$, we can calculate the conductivity tensor σ_{ij} as

$$\sigma_{ij} = gq^2\int\frac{d^dk}{(2\pi)^d}v_{\boldsymbol{k}}^{(i)}v_{\boldsymbol{k}}^{(j)}S^{(0)}(\varepsilon_{\boldsymbol{k}})\tau_{\boldsymbol{k}}, \tag{2.9}$$

where i is the direction of the response current, and j is the direction of the electric field $\boldsymbol{E}$. Note that for the DC conductivity where $i=j$, $\sigma_{ii}\sim D(\varepsilon_{\boldsymbol{k}})v_{\boldsymbol{k}}^2\tau_{\boldsymbol{k}}$, which is the Einstein relation ($D(\varepsilon_{\boldsymbol{k}})$ is the density of states).

2.2 Boltzmann transport theory for anisotropic, multi-band non-magnetic systems

In anisotropic, multi-band systems, many assumptions that made the calculations simple as seen in Section. (2.1) do not hold anymore. Instead of using

$\tau_{\boldsymbol{k}}$ defined from the relaxation condition, i.e. $-\frac{g_{\boldsymbol{k}}}{\tau_{\boldsymbol{k}}} = \left(\frac{df}{dt}\right)_{\text{coll}}$, we fall back to making ansatz of solution $g_{\boldsymbol{k}}$ that extends upon the relaxation condition. We assume $g_{\boldsymbol{k}}$ would take a form such as

$$g_{\boldsymbol{k}}^{\alpha} = q\left(\sum_{i=1}^{d} E^{(i)} v_{\boldsymbol{k}\alpha}^{(i)} \tau_{\boldsymbol{k}\alpha}^{(i)}\right) S^{(0)}(\varepsilon_{\boldsymbol{k}\alpha}), \tag{2.10}$$

where α is the band index. Note that the relaxation time τ is now also has the directional dependence, and if we remove the directional dependence and the band-dependence in Eq. (2.10), we would get Eq. (2.5) and it would also satisfy the original relaxation condition $-\frac{g_{\boldsymbol{k}}}{\tau_{\boldsymbol{k}}} = \left(\frac{df}{dt}\right)_{\text{coll}}$. The Boltzmann equation $\dot{\boldsymbol{k}} \cdot \nabla_{\boldsymbol{k}} f_{\boldsymbol{k}} = \left(\frac{df}{dt}\right)_{\text{coll}}$ then becomes

$$q\boldsymbol{E} \cdot \boldsymbol{v}_{\boldsymbol{k}\alpha} S^{(0)}(\varepsilon_{\boldsymbol{k}\alpha}) = \sum_{\alpha'} \int \frac{d^d k'}{(2\pi)^d} W_{\boldsymbol{k}\boldsymbol{k}'}^{\alpha\alpha'} (g_{\boldsymbol{k}}^{\alpha} - g_{\boldsymbol{k}'}^{\alpha'}). \tag{2.11}$$

where we have also extended the collision integral equation to account for multi-band nature of the system. Expanding $g_{\boldsymbol{k}}^{\alpha}$ with ansatz Eq. (2.10), we finally get the relaxation time equation as

$$1 = \sum_{\alpha'} \int \frac{d^d k'}{(2\pi)^d} W_{\boldsymbol{k}\boldsymbol{k}'}^{\alpha\alpha'} \left(\tau_{\boldsymbol{k}\alpha}^{(i)} - \frac{v_{\boldsymbol{k}'\alpha'}^{(i)}}{v_{\boldsymbol{k}\alpha}^{(i)}} \tau_{\boldsymbol{k}'\alpha'}^{(i)}\right). \tag{2.12}$$

We can numerically solve Eq. (2.12) for $\tau_{\boldsymbol{k}\alpha}^{(i)}$ by either angle discretization method or Fourier coefficient method. Both numerical methods would involve making the integral equation into solving linear system (e.g. $P\boldsymbol{\tau} = \mathbf{1}$, where P is a matrix, $\boldsymbol{\tau}$ and $\mathbf{1}$ are vectors), and if there are total N_α of the bands, the dimension of the solution $\boldsymbol{\tau}$ would increase N_α-fold.

The conductivity tensor σ_{ij} for anisotropic, multi-band system then becomes

$$\sigma_{ij} = gq^2 \sum_{\alpha} \int \frac{d^d k}{(2\pi)^d} v_{\boldsymbol{k}\alpha}^{(i)} v_{\boldsymbol{k}\alpha}^{(j)} S^{(0)}(\varepsilon_{\boldsymbol{k}\alpha}) \tau_{\boldsymbol{k}\alpha}^{(j)}. \tag{2.13}$$

Chapter 3

Transport properties of multi-Weyl semimetals

3.1 Introduction

There has been a growing interest in three-dimensional (3D) analogs of graphene called Weyl semimetals (WSMs) where bands disperse linearly in all directions in momentum space around a twofold point degeneracy. Most attention has been devoted to novel response functions in elementary WSMs which exhibit a linear dispersion; however, recently it has been realized that these are just the simplest members of a family of multi-Weyl semimetals (m-WSMs) [6, 21, 22] which are characterized instead by double (triple) Weyl-nodes with a linear dispersion along one symmetry direction but quadratic (cubic) dispersion along the remaining two directions. These multi-Weyl nodes have a topologically protected charge (also referred to as chirality) larger than one, a situation that can be stabilized by point group symmetries [6].

Noting that multilayer graphenes with certain stacking patterns support

two-dimensional (2D) gapless low energy spectra with high chiralities, these m-WSMs can be regarded as the 3D version of multilayer graphenes. One can expect that their modified energy dispersion and spin- or pseudospin-momentum locking textures will have important consequences for various physical properties due both to an enhanced density of states (DOS) and the anisotropy in the energy dispersion, distinguishing m-WSMs from elementary WSMs. In this chapter, we demonstrate that this emerges already at the level of dc conductivity in the strong scattering limit described by semiclassical Boltzmann transport theory. The transport properties of conventional linear WSMs have recently been explored theoretically by several authors [23–32], and there have been theoretical works on the stability of charge-neutral double-Weyl nodes in the presence of Gaussian disorder [33–35] and the thermoelectric transport properties in double-Weyl semimetals[36]. However, as we show below, the density and temperature dependences of the dc conductivity for m-WSMs require an understanding of the effect of anisotropy in the nonlinear dispersion on the scattering. We develop this theory and find that it predicts characteristic power-law dependences of the conductivity on density and temperature that depend on the topological charge of the Weyl node and distinguish m-WSMs from their linear counterparts.

3.2 Model

The low-energy effective Hamiltonian for m-WSMs with chirality J near a single Weyl point is given by [6, 21, 37]

$$H_J = \varepsilon_0 \left[\left(\frac{k_-}{k_0} \right)^J \sigma_+ + \left(\frac{k_+}{k_0} \right)^J \sigma_- \right] + \hbar v_z k_z \sigma_z, \tag{3.1}$$

where $k_\pm = k_x \pm ik_y$, $\sigma_\pm = \frac{1}{2}(\sigma_x \pm i\sigma_y)$, $\boldsymbol{\sigma}$ are the Pauli matrices acting in the space of the two bands that make contact at the Weyl point, and k_0 and ε_0 are the material-dependent parameters in units of momentum and energy, respectively. For simplicity, here we assumed an axial symmetry around the k_z axis. The eigenenergies of the Hamiltonian are given by $\varepsilon_\pm = \pm\varepsilon_0\sqrt{\tilde{k}_\parallel^{2J} + c_z^2\tilde{k}_z^2}$, where $\tilde{\boldsymbol{k}} = \boldsymbol{k}/k_0$, $\tilde{k}_\parallel = \sqrt{\tilde{k}_x^2 + \tilde{k}_y^2}$, and $c_z = \hbar v_z k_0/\varepsilon_0$, thus the Hamiltonian H_J has a linear dispersion along the k_z direction for $k_x = k_y = 0$, whereas a nonlinear dispersion $\sim k_\parallel^J$ along the in-plane direction for $k_z = 0$. Note that the system described by the Hamiltonian in Eq. (3.1) has a nontrivial topological charge characterized by the chirality index J [6]. [See Sec. A.1 in the appendix A for the eigenstates and DOS for m-WSMs.]

3.2.1 Boltzmann transport theory in anisotropic systems

We use semiclassical Boltzmann transport theory to calculate the density and temperature dependence of the dc conductivity, which is fundamental in understanding the transport properties of a system. Here we focus on the longitudinal part of the dc conductivity assuming time-reversal symmetry with vanishing Hall conductivities. The Boltzmann transport theory is known to be valid in the high carrier density limit, and we assume that the Fermi energy is away from the Weyl node, as shown in experiments [38, 39]. The limitation of the current approach will be discussed later.

For a d-dimensional *isotropic* system in which only a single band is involved in the scattering, it is well known that the momentum relaxation time at a wavevector $\boldsymbol{k}$ in the relaxation time approximation can be expressed as [40]

$$\frac{1}{\tau_{\boldsymbol{k}}} = \int \frac{d^d k'}{(2\pi)^d} W_{\boldsymbol{k}\boldsymbol{k}'}(1 - \cos\theta_{\boldsymbol{k}\boldsymbol{k}'}), \tag{3.2}$$

where $W_{\boldsymbol{k}\boldsymbol{k}'} = \frac{2\pi}{\hbar} n_{\text{imp}} |V_{\boldsymbol{k}\boldsymbol{k}'}|^2 \delta(\varepsilon_{\boldsymbol{k}} - \varepsilon_{\boldsymbol{k}'})$, n_{imp} is the impurity density, and $V_{\boldsymbol{k}\boldsymbol{k}'}$

is the impurity potential describing a scattering from $\boldsymbol{k}$ to $\boldsymbol{k}'$. The inverse relaxation time is a weighted average of the collision probability in which the forward scattering ($\theta_{\boldsymbol{k}\boldsymbol{k}'} = 0$) receives reduced weight.

For an *anisotropic* system, the relaxation time approximation Eq. (3.2) does not correctly describe the effects of the anisotropy on transport. Instead, coupled integral equations relating the relaxation times at different angles need to be solved to treat the anisotropy in the nonequilibrium distribution [41, 42]. The linearized Boltzmann transport equation for the distribution function $f_{\boldsymbol{k}} = f^{(0)}(\varepsilon) + \delta f_{\boldsymbol{k}}$ at energy $\varepsilon = \varepsilon_{\boldsymbol{k}}$ balances acceleration on the Fermi surface against the scattering rates

$$(-e)\boldsymbol{E} \cdot \boldsymbol{v}_{\boldsymbol{k}} S^{(0)}(\varepsilon) = \int \frac{d^d k'}{(2\pi)^d} W_{\boldsymbol{k}\boldsymbol{k}'} \left(\delta f_{\boldsymbol{k}} - \delta f_{\boldsymbol{k}'}\right), \tag{3.3}$$

where $S^{(0)}(\varepsilon) = -\frac{\partial f^{(0)}(\varepsilon)}{\partial \varepsilon}$, $f^{(0)}(\varepsilon) = \left[e^{\beta(\varepsilon-\mu)} + 1\right]^{-1}$ is the Fermi distribution function at equilibrium, and $\beta = \frac{1}{k_{\mathrm{B}} T}$. We parametrize $\delta f_{\boldsymbol{k}}$ in the form:

$$\delta f_{\boldsymbol{k}} = (-e) \left(\sum_{i=1}^{d} E^{(i)} v_{\boldsymbol{k}}^{(i)} \tau_{\boldsymbol{k}}^{(i)} \right) S^{(0)}(\varepsilon), \tag{3.4}$$

where $E^{(i)}$, $v_{\boldsymbol{k}}^{(i)}$, and $\tau_{\boldsymbol{k}}^{(i)}$ are the electric field, velocity, and relaxation time along the i-th direction, respectively. After matching each coefficient in $E^{(i)}$, we obtain an integral equation for the relaxation time,

$$1 = \int \frac{d^d k'}{(2\pi)^d} W_{\boldsymbol{k}\boldsymbol{k}'} \left(\tau_{\boldsymbol{k}}^{(i)} - \frac{v_{\boldsymbol{k}'}^{(i)}}{v_{\boldsymbol{k}}^{(i)}} \tau_{\boldsymbol{k}'}^{(i)} \right). \tag{3.5}$$

For the isotropic case [$\tau_{\boldsymbol{k}}^{(i)} = \tau(\varepsilon)$ for a given energy $\varepsilon = \varepsilon_{\boldsymbol{k}}$], Eq. (3.5) reduces to Eq. (3.2). [See Sec. A.2 in Appendix. A for applications of Eq. (3.5) to m-WSMs.] The current density $\boldsymbol{J}$ induced by an electric field $\boldsymbol{E}$ is then given by

$$J^{(i)} = g \int \frac{d^d k}{(2\pi)^d} (-e) v_{\boldsymbol{k}}^{(i)} \delta f_{\boldsymbol{k}} \equiv \sigma_{ij} E^{(j)}, \tag{3.6}$$

where g is the degeneracy factor and σ_{ij} is the conductivity tensor given by

$$\sigma_{ij} = ge^2 \int \frac{d^d k}{(2\pi)^d} S^{(0)}(\varepsilon) v_{\boldsymbol{k}}^{(i)} v_{\boldsymbol{k}}^{(j)} \tau_{\boldsymbol{k}}^{(j)}. \tag{3.7}$$

For the calculation, we set $g = 4$ and $v_z = v_0 \equiv \frac{\varepsilon_0}{\hbar k_0}$.

3.3 Density dependence of dc conductivity

Consider the m-WSMs described by Eq. (3.1) with chirality J and their dc conductivity as a function of carrier density at zero temperature. Due to the anisotropic energy dispersion with the axial symmetry, for $J > 1$ the conductivity also will be anisotropic as $\sigma_{xx} = \sigma_{yy} \neq \sigma_{zz}$.

We consider two types of impurity scattering: short-range impurities (e.g., lattice defects, vacancies, and dislocations) and charged impurities distributed randomly in the background. The impurity potential for short-range scatterers is given by a constant $V_{\boldsymbol{k}\boldsymbol{k}'} = V_{\text{short}}$ in momentum space (i.e., zero-range delta function in real space), whereas for charged Coulomb impurities in 3D it is given by $V_{\boldsymbol{k}\boldsymbol{k}'} = \frac{4\pi e^2}{\epsilon(\boldsymbol{q})|\boldsymbol{q}|^2}$, where $\epsilon(\boldsymbol{q})$ is the dielectric function for $\boldsymbol{q} = \boldsymbol{k} - \boldsymbol{k}'$. Within the Thomas-Fermi approximation, the dielectric function can be approximated as $\epsilon(\boldsymbol{q}) \approx \kappa \left[1 + (q_{\text{TF}}^2/|\boldsymbol{q}|^2)\right]$, where κ is the background dielectric constant, $q_{\text{TF}} = \sqrt{\frac{4\pi e^2}{\kappa} D(\varepsilon_{\text{F}})}$ is the Thomas-Fermi wave vector, and $D(\varepsilon_{\text{F}})$ is the DOS at the Fermi energy ε_{F}. The interaction strength for charged impurities can be characterized by an effective fine structure constant $\alpha = \frac{e^2}{\kappa \hbar v_0}$. Note that $q_{\text{TF}} \propto \sqrt{g\alpha}$.

Figure 3.1 shows the density dependence of the dc conductivity for charged impurity scattering at zero temperature. Because of the chirality J, m-WSMs have a characteristic density dependence in dc conductivity, which can be understood as follows. From Eq. (3.7), we expect $\sigma_{ii} \sim [v_{\text{F}}^{(i)}]^2 / V_{\text{F}}^2$, where $v_{\text{F}}^{(i)}$ is

the Fermi velocity along the ith direction and $V_{\rm F}^2$ is the angle-averaged squared impurity potential at the Fermi energy $\varepsilon_{\rm F}$.

For m-WSMs, the in-plane component with $k_z = 0$ and out-of-plane component with $k_x = k_y = 0$ for the velocity at $\varepsilon_{\rm F}$ are given by $v_{\rm F}^{(\parallel)} = J v_0 r_{\rm F}^{1-\frac{1}{J}}$ and $v_{\rm F}^{(z)} = v_0 c_z$, respectively, where $r_{\rm F} = \varepsilon_{\rm F}/\varepsilon_0$. (See Sec. A.1 in Appendix. A.)

For charged impurities, in the strong screening limit ($g\alpha \gg 1$), $V_{\rm F} \sim q_{\rm TF}^{-2} \sim D^{-1}(\varepsilon_{\rm F}) \sim \varepsilon_{\rm F}^{-\frac{2}{J}}$, thus we find

$$\sigma_{xx} \sim \varepsilon_{\rm F}^{2\left(1-\frac{1}{J}\right)} \varepsilon_{\rm F}^{\frac{4}{J}} \sim n^{\frac{2(J+1)}{J+2}}, \tag{3.8a}$$

$$\sigma_{zz} \sim \varepsilon_{\rm F}^{\frac{4}{J}} \sim n^{\frac{4}{J+2}}. \tag{3.8b}$$

Here, the DOS is $D(\varepsilon) \sim \varepsilon^{\frac{2}{J}}$, thus $\varepsilon_{\rm F} \sim n^{\frac{J}{J+2}}$. In the weak screening limit ($g\alpha \ll 1$), we expect $V_{\rm F} \sim \varepsilon_{\rm F}^{-2\zeta}$ with $\frac{1}{J} \le \zeta \le 1$, because the in-plane and out-of-plane components of the wavevector at $\varepsilon_{\rm F}$ are $k_{\rm F}^{(\parallel)} = k_0 r_{\rm F}^{\frac{1}{J}}$ and $k_{\rm F}^{(z)} = k_0 r_{\rm F}/c_z$, respectively. Thus, we find

$$\sigma_{xx} \sim \varepsilon_{\rm F}^{2\left(1-\frac{1}{J}\right)} \varepsilon_{\rm F}^{4\zeta} \sim n^{\frac{2(J-1)+4J\zeta}{J+2}}, \tag{3.9a}$$

$$\sigma_{zz} \sim \varepsilon_{\rm F}^{4\zeta} \sim n^{\frac{4J\zeta}{J+2}}. \tag{3.9b}$$

(See Sec. A.2 in Appendix. A for the analytic expressions of the dc conductivity for short-range impurities and for charged impurities in the strong screening limit, and a detailed discussion for charged impurities in the weak screening limit.)

Figure 3.2 illustrates the evolution of the power-law density dependence of the dc conductivity as a function of the screening strength characterized by $g\alpha$. Note that $\zeta = \frac{1}{J}$ in Eq. (3.9) gives the same density exponent as in the strong screening limit in Eq. (3.8). Thus, as α increases, the density exponent evolves from that obtained in Eq. (3.9) with decreasing ζ within the range $\frac{1}{J} \le \zeta \le 1$. Here, nonmonotonic behavior in the density exponent originates

from the angle-dependent power law in the relaxation time, which manifests in the weak screening limit. (See Sec. A.2 in Appendix. A for further discussion.)

Similarly, for short-ranged impurities, V_{F} is a constant independent of density; in this case we find

$$\sigma_{xx} \sim \varepsilon_{\mathrm{F}}^{2\left(1-\frac{1}{J}\right)} \sim n^{\frac{2(J-1)}{J+2}}, \tag{3.10a}$$

$$\sigma_{zz} \sim \varepsilon_{\mathrm{F}}^{0} \sim n^{0}. \tag{3.10b}$$

The anisotropy in conductivity can be characterized by σ_{xx}/σ_{zz}. Figure 3.3 shows σ_{xx}/σ_{zz} as a function of density for m-WSMs. Thus, as the carrier density increases, the anisotropy in conductivity increases. Interestingly, σ_{xx}/σ_{zz} for both short-range impurities and charged impurities in the strong screening limit is given by

$$\sigma_{xx}/\sigma_{zz} \sim \varepsilon_{\mathrm{F}}^{2\left(1-\frac{1}{J}\right)} \sim n^{\frac{2(J-1)}{J+2}}. \tag{3.11}$$

Note that for arbitrary screening, ζs for σ_{xx} and σ_{zz} in Eq. (3.9) are actually different, thus not cancelled in σ_{xx}/σ_{zz} and the power-law deviates from that in Eq. (3.11). (See Sec. A.2 in Appendix. A for the analytic/asymptotic expressions of the density dependence of σ_{xx}/σ_{zz}.)

We consider both the short-range and charged impurities by adding their scattering rates according to Matthiessen's rule assuming that each scattering mechanism is independent. At low densities (but high enough to validate the Boltzmann theory) the charged impurity scattering always dominates the short-range scattering, while at high densities the short-range scattering dominates, irrespective of the chirality J and screening strength.

3.4 Temperature dependence of dc conductivity

In 3D materials, it is not easy to change the density of charge carriers by gating, because of screening in the bulk. However, the temperature dependence

of dc conductivity can be used to understand the carrier dynamics of the system. The effect of finite temperature arises from the energy averaging over the Fermi distribution function in Eq. (3.7), and the temperature dependence of the screening of the impurity potential for charged impurities [43, 44].

From the invariance of carrier density with respect to temperature, we obtain the variation of the chemical potential $\mu(T)$ as a function of temperature T. Then the Thomas-Fermi wavevector $q_{\rm TF}(T)$ in 3D at finite T can be expressed as $q_{\rm TF}(T) = \sqrt{\frac{4\pi e^2}{\kappa}\frac{\partial n}{\partial \mu}}$. In the low- and high-temperature limits, the chemical potential is given by

$$\frac{\mu}{\varepsilon_{\rm F}} = \begin{cases} 1 - \frac{\pi^2}{3J}\left(\frac{T}{T_{\rm F}}\right)^2 & (T \ll T_{\rm F}), \\ \frac{1}{2\eta\left(\frac{2}{J}\right)\Gamma\left(2+\frac{2}{J}\right)}\left(\frac{T}{T_{\rm F}}\right)^{-\frac{2}{J}} & (T \gg T_{\rm F}), \end{cases} \tag{3.12}$$

whereas the Thomas-Fermi wave vector is given by

$$\frac{q_{\rm TF}(T)}{q_{\rm TF}(0)} = \begin{cases} 1 - \frac{\pi^2}{6J}\left(\frac{T}{T_{\rm F}}\right)^2 & (T \ll T_{\rm F}), \\ \sqrt{2\eta\left(\frac{2}{J}\right)\Gamma\left(1+\frac{2}{J}\right)}\left(\frac{T}{T_{\rm F}}\right)^{\frac{1}{J}} & (T \gg T_{\rm F}), \end{cases} \tag{3.13}$$

where $T_{\rm F} = \varepsilon_{\rm F}/k_{\rm B}$ is the Fermi temperature, and Γ and η are the gamma function and the Dirichlet eta function [45], respectively. (See Sec. B.4 in Appendix. A for the temperature dependence of the chemical potential and Thomas-Fermi wave vector.) In a single-band system, $q_{\rm TF}(T)$ always decreases with T^{-1} at high temperatures, whereas in m-WSMs, $q_{\rm TF}(T)$ increases with $T^{\frac{1}{J}}$ because of the thermal excitation of carriers that participate in the screening.

Figure 3.4 shows the temperature dependence of dc conductivity for charged

impurities. We find

$$\frac{\sigma_{xx}(T)}{\sigma_{xx}(0)} = \begin{cases} 1 + C_{xx}\left(\frac{T}{T_{\rm F}}\right)^2 & (T \ll T_{\rm F}), \\ D_{xx}\left(\frac{T}{T_{\rm F}}\right)^{2+4\zeta-\frac{2}{J}} & (T \gg T_{\rm F}), \end{cases} \tag{3.14a}$$

$$\frac{\sigma_{zz}(T)}{\sigma_{zz}(0)} = \begin{cases} 1 + C_{zz}\left(\frac{T}{T_{\rm F}}\right)^2 & (T \ll T_{\rm F}), \\ D_{zz}\left(\frac{T}{T_{\rm F}}\right)^{4\zeta} & (T \gg T_{\rm F}). \end{cases} \tag{3.14b}$$

As discussed, ζ varies within $\frac{1}{J} \leq \zeta \leq 1$ and approaches $\frac{1}{J}$ in the strong screening limit ($g\alpha \gg 1$). Here, the high-temperature coefficients $D_{ii} > 0$, whereas the low-temperature coefficients C_{ii} change sign from negative to positive as α increases. For short-range impurities, we find

$$\frac{\sigma_{xx}(T)}{\sigma_{xx}(0)} = \begin{cases} 1 + C_{xx}^{\rm short}\left(\frac{T}{T_{\rm F}}\right)^2 & (T \ll T_{\rm F}), \\ D_{xx}^{\rm short}\left(\frac{T}{T_{\rm F}}\right)^{\frac{2(J-1)}{J}} & (T \gg T_{\rm F}), \end{cases} \tag{3.15a}$$

$$\frac{\sigma_{zz}(T)}{\sigma_{zz}(0)} = \begin{cases} 1 - e^{-T_{\rm F}/T} & (T \ll T_{\rm F}), \\ \frac{1}{2} + D_{zz}^{\rm short}\left(\frac{T}{T_{\rm F}}\right)^{-\frac{2+J}{J}} & (T \gg T_{\rm F}). \end{cases} \tag{3.15b}$$

Here, $C_{xx}^{\rm short} < 0$ and $D_{ii}^{\rm short} > 0$. Note that for $J = 1$, Eq. (3.15a) becomes constant, and reduces to Eq. (3.15b) if next order corrections are included. (See Sec. A.4 in Appendix. A for the analytic/asymptotic expressions of the temperature coefficients, and the evolution of C_{ii} as a function of $g\alpha$.)

To understand the temperature dependence, we can consider a situation where the thermally induced charge carriers participate in transport. Then the temperature dependence in the high-temperature limit can be obtained simply by replacing the $\varepsilon_{\rm F}$ dependence with T in Eqs. (3.8)-(3.10), which describe the density dependence of dc conductivity. Similarly as in Fig. 3.3, $\sigma_{xx}(T)/\sigma_{zz}(T)$ also increases with T at high temperatures.

For the charged impurities at high temperatures, and neglecting the effect of phonons, the conductivity increases with temperature, and mimics an insulating behavior. By contrast, for short-range impurities at high temperatures, $\sigma_{zz}(T)$ decreases with temperature and approaches $0.5\sigma_{zz}(0)$, thus showing a metallic behavior. Interestingly, $\sigma_{xx}(T)$ shows contrasting behavior for $J > 1$ and $J = 1$, increasing (decreasing) with temperature for $J > 1$ ($J = 1$) showing insulating (metallic) behavior at high temperatures.

3.5 Discussion

We find that the dc conductivities in the Boltzmann limit show characteristic density and temperature dependences that depend strongly on the chirality of the system, revealing a signature of m-WSMs in transport measurements, which can be compared with experiments. In real materials with time reversal symmetry, multiple Weyl points with compensating chiralities will be present. The contributions from the individual nodes calculated by our method are additive when the Weyl points are well separated and internode scattering is weak. Our analysis is based on the semiclassical Boltzmann transport theory with the Thomas-Fermi approximation for screening and corrected for the anisotropy of the Fermi surface in m-WSMs. The Boltzmann transport theory is known to be valid in the high density limit. At low densities, inhomogeneous impurities induce a spatially varying local chemical potential, typically giving a minimum conductivity when the chemical potential is at the Weyl node [31] and the problem is treated within the effective medium theory. Note that the Thomas-Fermi approximation used in this work is the long-wavelength limit of the random phase approximation (RPA), and neglects interband contributions to the polarization function [31], thus deviating from the RPA result at low densities.

Both simplifications become important in the low-density limit, which will be considered in our future work.

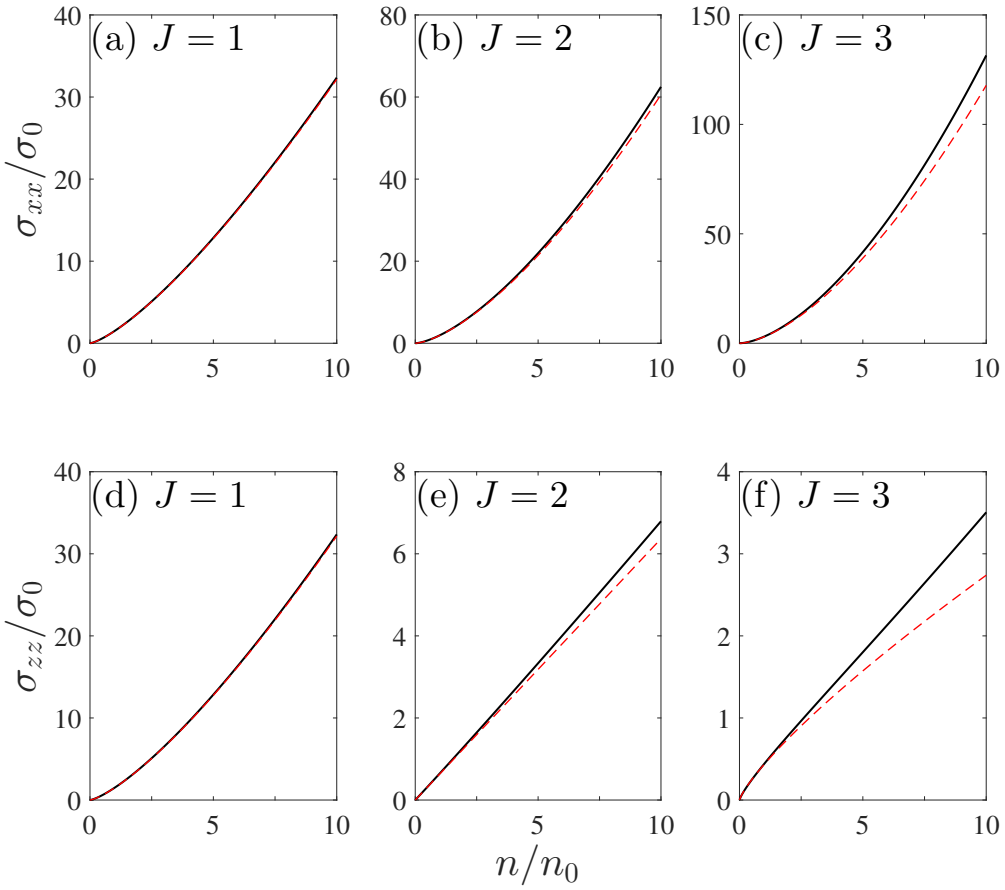

Figure 3.1 Density dependence of dc conductivity (a)-(c) σ_{xx} and (d)-(f) σ_{zz} for charged impurities with $g\alpha = 1000$. Here, σ_0 and n_0 are density-independent normalization constants in units of conductivity and density, respectively, defined in Appendix. A. Red dashed lines represent analytic forms in the strong screening limit given by Eq. (A.24) in Appendix. A.

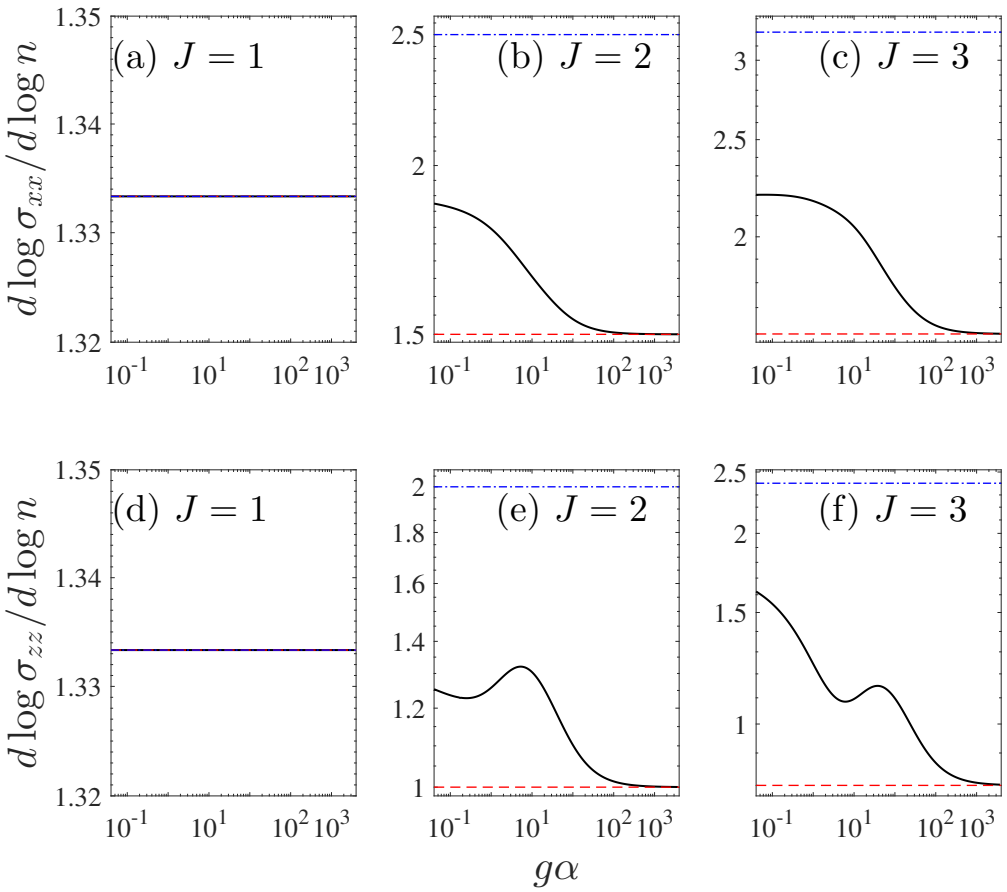

Figure 3.2 (a)-(c) $d \log \sigma_{xx} / d \log n$ and (d)-(f) $d \log \sigma_{zz} / d \log n$ as a function of the screening strength $g\alpha$ for charged impurities. Red dashed and blue dashed-dotted lines represent the density exponents obtained from $\zeta = \frac{1}{J}$ (or in the strong screening limit) and $\zeta = 1$ in Eq. (3.9), respectively. Here, $n = n_0$ is used for the calculation.

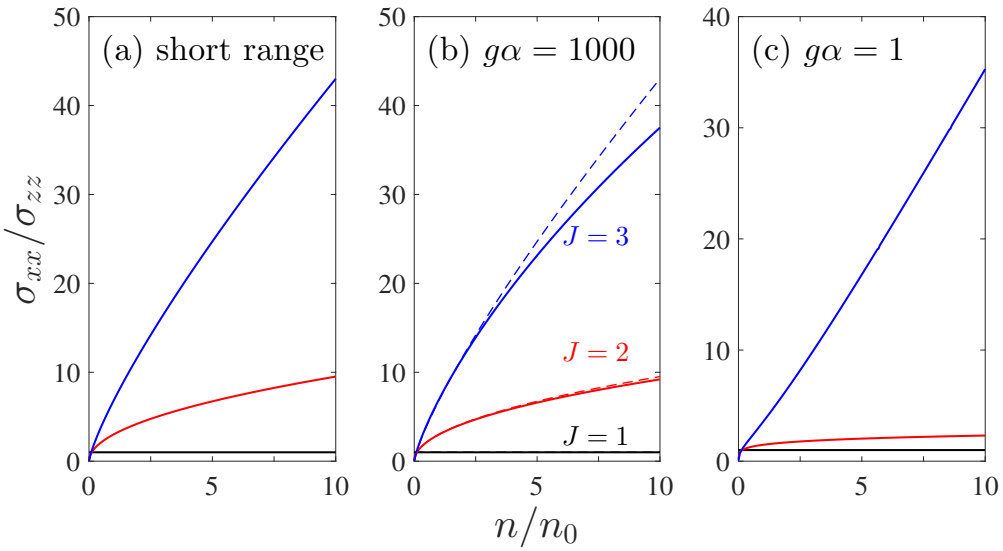

Figure 3.3 σ_{xx}/σ_{zz} as a function of density for m-WSMs with $J = 1, 2, 3$ for (a) short-range impurities, (b) charged impurities with $g\alpha = 1000$, and (c) charged impurities with $g\alpha = 1$. Dashed lines in (b) represent analytic forms in the strong screening limit given by Eq. (A.24) in Appendix. A.

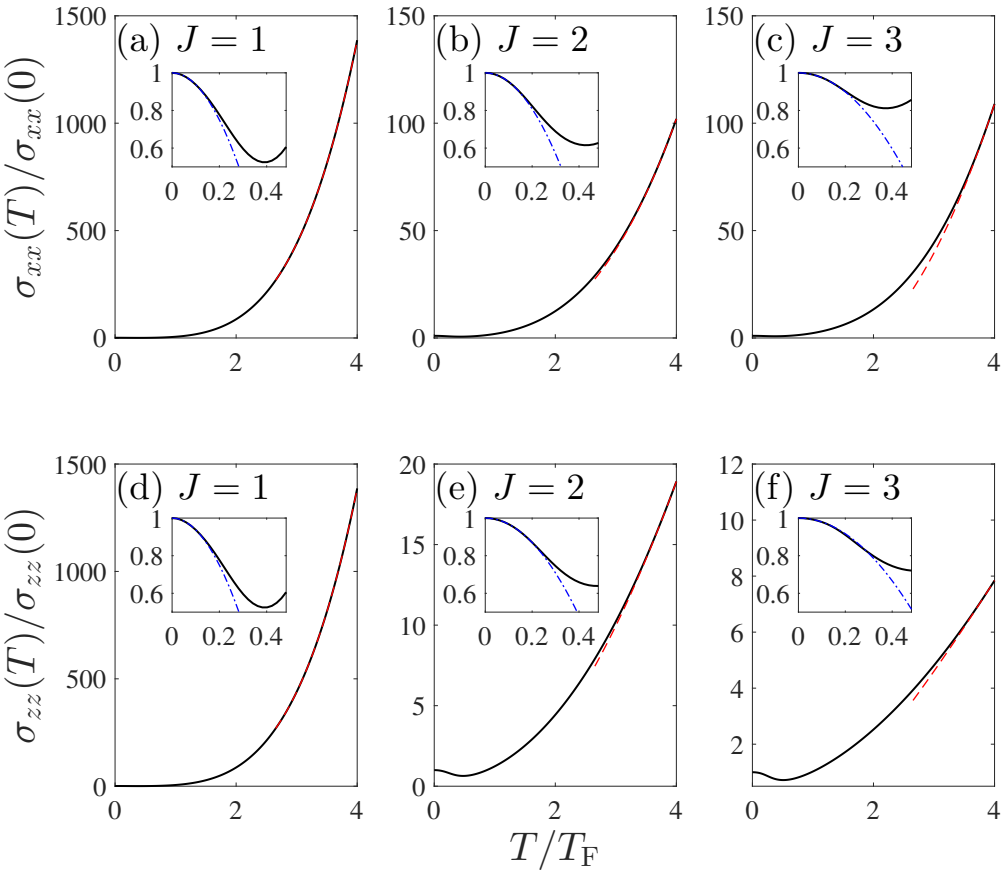

Figure 3.4 Temperature dependence of dc conductivity (a)-(c) σ_{xx} and (d)-(f) σ_{zz} for charged impurities with $g\alpha = 1000$. The insets in each panel show the low temperature behavior. Red dashed and blue dashed-dotted lines represent fitting by Eq. (3.14) with $\zeta = \frac{1}{J}$ in the high- and low- temperature limits, respectively.

Chapter 4

Transport properties of few-layer black phosphorus in various phases

4.1 Introduction

Since the discovery of graphene [44, 46], which is a carbon allotrope of two-dimensional (2D) honeycomb lattice, 2D materials have been one of the most active research areas in condensed matter physics. Black phosphorus (BP) is a 2D material with van der Waals layered structure composed of phosphorus atoms, and it has recently attracted considerable attention [7, 8]. As a layered semiconductor in its natural form, BP has a tunable band gap, and manipulation of its band gap through various methods has been validated by multiple theoretical and experimental reports [9]. Notable examples of the band gap tuning include thickness change [10, 11], strain control [12], pressure [13], electronic gating [14–16], and chemical doping [17]. Some of the band gap manipulation methods [13, 17] demonstrated that the band gap can be tuned to zero, showing

the semi-Dirac state with a combination of linear and quadratic dispersions [47], which is also predicted in TiO_2/VO_2 heterostructures [48, 49]. Furthermore, the band gap can be inverted, leading to the Dirac semimetal phase [18–20].

Due to its anisotropic electronic band structure, BP shows many peculiar transport properties such as large in-plane anisotropic transport [50, 51]. The effects of temperature [14, 52, 53], the number of layers [14], and substrate [52] on the anisotropic transport properties of BP have been studied experimentally. Furthermore, the transport properties of BP have been studied theoretically [54–59], demonstrating its anisotropic nature in energy- and temperature-dependent transport. However, there has been no systematic study on the anisotropic transport of BP in each phase, fully considering the anisotropy of the system and the interband scattering. In this study, we theoretically investigate the transport properties of BP in the gapped insulator phase, gapless semi-Dirac transition point, and Dirac semimetal phase. Using the semiclassical Boltzmann transport theory generalized to anisotropic multiband systems, we calculate the dc conductivity as a function of the carrier density and temperature for each phase. We determine that each phase shows the characteristic density and temperature dependence, which can be used as a transport signature of BP in different phases.

The rest of this chapter is organized as follows. In Sec. 4.2, we describe our model Hamiltonian and develop the Boltzmann transport theory in anisotropic multiband systems. In Sec. 4.3, we present the dc conductivity of BP in each phase as a function of density at zero temperature. In Sec. 4.4, we provide the temperature dependence of dc conductivity at a fixed density. We conclude our chapter in Sec. 5.5 with discussions on the dominant scattering source, the effect of potential fluctuations at low densities, and the effect of the parabolic term omitted in the current model.

4.2 Methods

4.2.1 Model

By expanding the tight-binding lattice model of few-layer BP [8, 60, 61], the corresponding low-energy effective Hamiltonian can be obtained as [62–66]

$$H = \left(\frac{\hbar^2 k_x^2}{2m^*} + \frac{\varepsilon_{\mathrm{g}}}{2} \right) \sigma_x + \hbar v_0 k_y \sigma_y, \tag{4.1}$$

where m^* is the effective mass along the zigzag (x) direction, v_0 is the band velocity along the armchair (y) direction, ε_{g} is the size of the band gap (which will be used as a tuning parameter), and σ_x and σ_y are the Pauli matrices. The eigenenergies of the Hamiltonian are given by $\varepsilon_{\pm} = \pm\sqrt{\left(\frac{\hbar^2 k_x^2}{2m^*} + \frac{\varepsilon_{\mathrm{g}}}{2} \right)^2 + \hbar^2 v_0^2 k_y^2}$; thus, the Hamiltonian H has a direct band gap for $\varepsilon_{\mathrm{g}} > 0$, a semi-Dirac band touching point at $(k_x, k_y) = (0, 0)$ for $\varepsilon_{\mathrm{g}} = 0$, or two Dirac points at $(k_x, k_y) = (\pm\sqrt{\frac{m^*|\varepsilon_{\mathrm{g}}|}{\hbar^2}}, 0)$ for $\varepsilon_{\mathrm{g}} < 0$. The characteristic energy scales along the zigzag and armchair directions are given by $\varepsilon_0 = \frac{\hbar^2 k_0^2}{2m^*}$ and $\hbar v_0 k_0$, respectively, where $k_0 = a^{-1}$ and a is the lattice constant. We introduce the dimensionless parameters $\Delta = \frac{\varepsilon_{\mathrm{g}}}{2\varepsilon_0}$ and $c = \frac{\hbar v_0 k_0}{\varepsilon_0}$, which represent a gap tuning parameter and the ratio of the characteristic energy scales along the zigzag and armchair directions, respectively. Throughout the chapter, we use $c = 1$ and the spin degeneracy $g = 2$ for the calculation. We will discuss the effect of higher-order terms omitted in Eq. (4.1) in Sec. 5.5.

Figure 4.1 shows the energy dispersion and the corresponding Fermi surface of few-layer BP in each phase. Initially, few-layer BP without band gap tuning is in the gapped insulator phase, as shown in Fig. 4.1(a). As the band gap ε_{g} decreases (for example, upon applying a perpendicular electric field), eventually it vanishes and the system is described by the semi-Dirac Hamiltonian in Eq. (4.1) with $\varepsilon_{\mathrm{g}} = 0$, as shown in Fig. 4.1(b). If the band gap decreases even

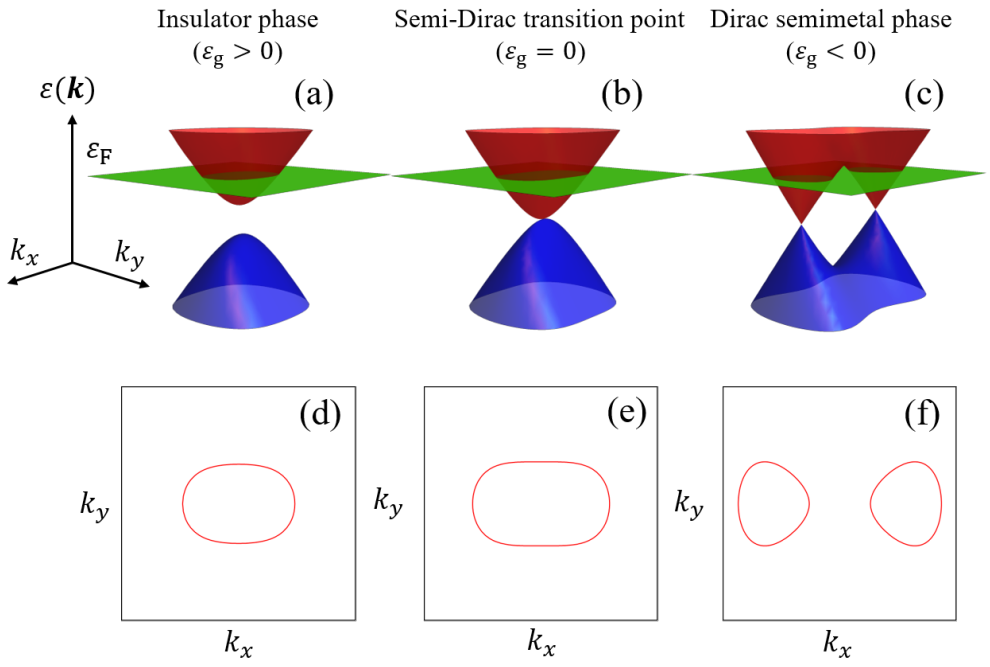

Figure 4.1 (a)-(c) Energy dispersions and (d)-(f) the corresponding Fermi surfaces of few-layer BP for the (a), (c) insulator phase, (b), (e) semi-Dirac transition point, and (c), (f) Dirac semimetal phase.

further and becomes negative ($\varepsilon_g < 0$), band inversion occurs, which has been achieved experimentally using surface doping [18, 19] and external pressure [20]

In the gapped insulator phase, the inherent anisotropy of the system is less evident and the system at low densities resembles typical semiconductors with a different effective mass in each direction. At the semi-Dirac transition point, the energy dispersion becomes linear (quadratic) along the armchair (zigzag) direction, as shown in Fig. 4.1(e). At the Dirac semimetal phase, the anisotropy in the energy dispersion becomes more pronounced and the Fermi surface vastly changes its shape depending on the value of the Fermi energy ε_F. For $\varepsilon_F < \varepsilon_g/2$, the Fermi surface becomes two distinct lines, as shown in Fig. 4.1(f), whereas

for $\varepsilon_{\rm F} > \varepsilon_{\rm g}/2$, the two Fermi surfaces become joined completely, forming a closed line. At $\varepsilon_{\rm F} = \varepsilon_{\rm g}/2$, a van Hove singularity occurs in the density of states (DOS), as explained below.

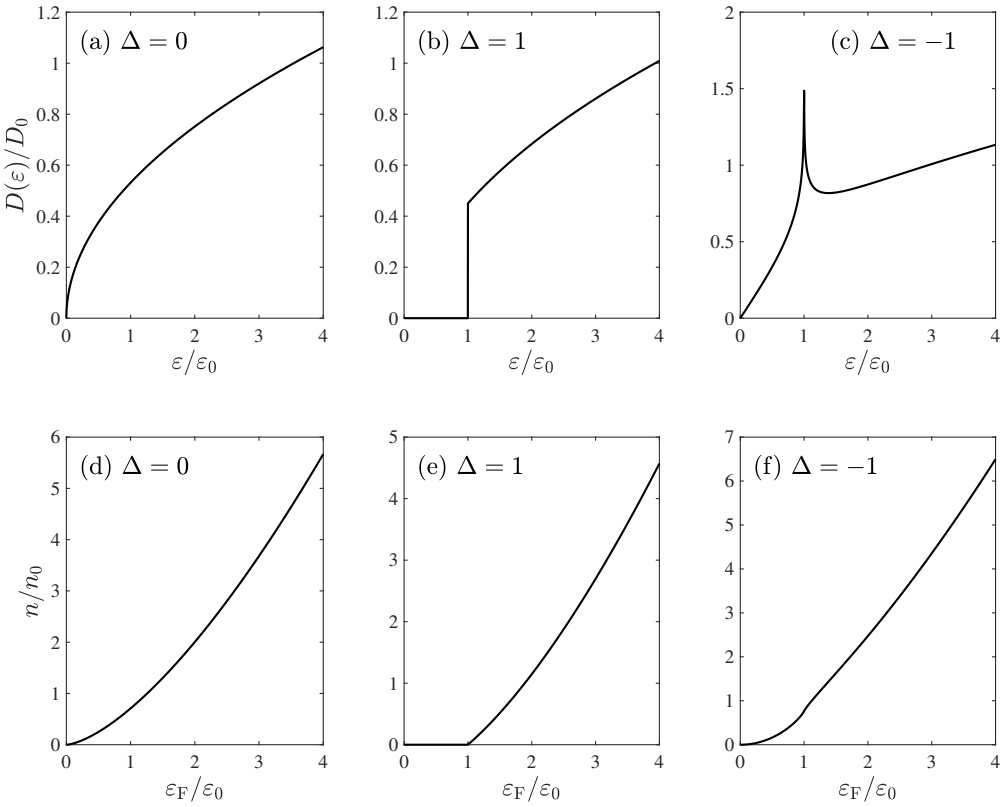

Figure 4.2 (a)-(c) Calculated DOS and (d)-(e) the carrier density as a function of Fermi energy for the (a), (c) insulator phase, (b), (e) semi-Dirac transition point, and (c), (f) Dirac semimetal phase. Here, $\Delta \equiv \frac{\varepsilon_{\rm g}}{2\varepsilon_0}$ is the band gap tuning parameter, and $g = 2$ and $c = 1$ are used for calculation.

Figure 4.2 shows the DOS and the carrier density as a function of Fermi energy for each phase. At the semi-Dirac transition point, the DOS is simply given by $D(\varepsilon) \sim \varepsilon^{1/2}$ [Fig. 4.2(a)], and the carrier density (which is an en-

ergy integral of the DOS up to ε_{F}) is given by $n \sim \varepsilon_{\mathrm{F}}^{3/2}$ [Fig. 4.2(d)]. (See Appendix A.1 for the detailed derivations of the DOS and the carrier density.) In the gapped insulator phase, both DOS at ε_{F} and carrier density vanish for $\varepsilon_{\mathrm{F}} < \varepsilon_{\mathrm{g}}/2$, whereas for $\varepsilon_{\mathrm{F}} > \varepsilon_{\mathrm{g}}/2$, they follow those of the semi-Dirac transition point as ε_{F} increases [Figs. 4.2(b) and 4.2(e)]. In the Dirac semimetal phase, when ε_{F} is very small, the system resembles a typical 2D Dirac semimetal such as graphene; thus, $D(\varepsilon) \sim \varepsilon^1$. As ε_{F} increases and approaches $\varepsilon_{\mathrm{g}}/2$ near the top of the inverted band, the band dispersion effectively becomes hyperbolic paraboloid with a different sign in each direction in momentum space. Subsequently, a van Hove singularity occurs in the DOS, diverging logarithmically with $D(\varepsilon) \sim -\log(|\Delta| - \varepsilon)^{-1}$ [67]. If ε_{F} increases further, the DOS and the carrier density follow those of the semi-Dirac transition point with a discontinuous energy derivative in the DOS at the van Hove singularity [Figs. 4.2(c) and 4.2(f)].

Notably, as the energy dispersion and the Fermi surface are anisotropic, and the Fermi energy can cross multiple bands, we cannot naively use the conventional Boltzmann transport theory assuming an isotropic single-band system. Thus, the anisotropic multiband Boltzmann transport theory is necessary to calculate the dc conductivity of such systems, as explained in Sec. 4.2.2.

4.2.2 Boltzmann transport theory in anisotropic multiband systems

We use semiclassical Boltzmann transport theory to calculate the density and temperature dependence of the dc conductivity of few-layer BP in each phase in the presence of impurities, assuming elastic scattering (see Sec. 5.5 for the limitation of the current approach). In the Boltzmann transport theory, electron states are described by the non-equilibrium distribution function $f = f(\boldsymbol{r}, \boldsymbol{k}; t)$.

Its time rate of change is balanced out by the collision term, which represents the total scattering probability per unit time, i.e., $\frac{df}{dt} = \left(\frac{df}{dt}\right)_{\rm coll}$.

We assume a spatially homogeneous system without explicit time dependence in the distribution function, i.e., $f = f_{\boldsymbol{k}}$. Thus, the time derivative of the distribution function is given by $\frac{df}{dt} = \dot{\boldsymbol{k}} \cdot \frac{\partial f_{\boldsymbol{k}}}{\partial \boldsymbol{k}}$, whereas the collision term is given by

$$\left(\frac{df}{dt}\right)_{\rm coll} = -\int \frac{d^d k'}{(2\pi)^d} W_{\boldsymbol{k}\boldsymbol{k}'}(f_{\boldsymbol{k}} - f_{\boldsymbol{k}'}), \tag{4.2}$$

where $W_{\boldsymbol{k}\boldsymbol{k}'} = \frac{2\pi}{\hbar} n_{\rm imp} |V_{\boldsymbol{k}\boldsymbol{k}'}|^2 \delta(\varepsilon_{\boldsymbol{k}} - \varepsilon_{\boldsymbol{k}'})$ is the transition rate from $\boldsymbol{k}$ to $\boldsymbol{k}'$ for an elastic scattering with the impurity potential $V_{\boldsymbol{k}\boldsymbol{k}'}$ and the impurity density $n_{\rm imp}$. In the presence of a uniform electric field $\boldsymbol{E}$, $\hbar\dot{\boldsymbol{k}} = (-e)\boldsymbol{E}$, and to the leading order in $\boldsymbol{E}$,

$$\frac{df_{\boldsymbol{k}}}{dt} \approx (-e)\boldsymbol{E} \cdot \frac{\partial f^{(0)}_{\boldsymbol{k}}}{\hbar \partial \boldsymbol{k}} = (-e)\boldsymbol{E} \cdot \boldsymbol{v}_{\boldsymbol{k}} \frac{\partial f^{(0)}_{\boldsymbol{k}}}{\partial \varepsilon_{\boldsymbol{k}}}, \tag{4.3}$$

where $\boldsymbol{v}_{\boldsymbol{k}} = \frac{1}{\hbar}\frac{\partial \varepsilon_{\boldsymbol{k}}}{\partial \boldsymbol{k}}$ and $f^{(0)}_{\boldsymbol{k}} = f^{(0)}(\varepsilon_{\boldsymbol{k}}) = \left[e^{\beta(\varepsilon_{\boldsymbol{k}} - \mu)} + 1\right]^{-1}$ is the Fermi–Dirac distribution function at equilibrium with $\beta = \frac{1}{k_{\rm B}T}$ and the chemical potential μ. Assume that, to the leading order in $\boldsymbol{E}$, the non-equilibrium distribution function $f_{\boldsymbol{k}}$ is given by $f_{\boldsymbol{k}} \equiv f^{(0)}(\varepsilon) + \delta f_{\boldsymbol{k}}$ at energy $\varepsilon = \varepsilon_{\boldsymbol{k}}$. Thus, from $\frac{df}{dt} = \left(\frac{df}{dt}\right)_{\rm coll}$, we obtain

$$(-e)\boldsymbol{E} \cdot \boldsymbol{v}_{\boldsymbol{k}} S^{(0)}(\varepsilon) = \int \frac{d^d k'}{(2\pi)^d} W_{\boldsymbol{k}\boldsymbol{k}'}(\delta f_{\boldsymbol{k}} - \delta f_{\boldsymbol{k}'}), \tag{4.4}$$

where $S^{(0)}(\varepsilon) = -\frac{\partial f^{(0)}(\varepsilon)}{\partial \varepsilon}$. If the Fermi energy crosses multiple energy bands, Eq. (4.4) is generalized to [68, 69]

$$(-e)\boldsymbol{E} \cdot \boldsymbol{v}_{\boldsymbol{k}\alpha} S^{(0)}(\varepsilon) = \sum_{\alpha'} \int \frac{d^d k'}{(2\pi)^d} W^{\alpha\alpha'}_{\boldsymbol{k}\boldsymbol{k}'} \left(\delta f^{\alpha}_{\boldsymbol{k}} - \delta f^{\alpha'}_{\boldsymbol{k}'}\right), \tag{4.5}$$

where α and α' are band indices.

We parameterize $\delta f^{\alpha}_{\boldsymbol{k}}$ in the following form [41, 42, 70]:

$$\delta f^{\alpha}_{\boldsymbol{k}} = (-e)\left(\sum_{i=1}^{d} E^{(i)} v^{(i)}_{\boldsymbol{k}\alpha}\tau^{(i)}_{\boldsymbol{k}\alpha}\right) S^{(0)}(\varepsilon), \tag{4.6}$$

where $E^{(i)}$, $v^{(i)}_{\boldsymbol{k}\alpha}$, and $\tau^{(i)}_{\boldsymbol{k}\alpha}$ are the electric field, velocity, and relaxation time, respectively, along the ith direction for each band. After matching each coefficient in $E^{(i)}$, we obtain the following integral equation for the relaxation time:

$$1 = \sum_{\alpha'}\int \frac{d^d k'}{(2\pi)^d} W^{\alpha\alpha'}_{\boldsymbol{k}\boldsymbol{k}'}\left(\tau^{(i)}_{\boldsymbol{k}\alpha} - \frac{v^{(i)}_{\boldsymbol{k}'\alpha'}}{v^{(i)}_{\boldsymbol{k}\alpha}}\tau^{(i)}_{\boldsymbol{k}'\alpha'}\right). \tag{4.7}$$

This is a coupled integral equation relating the relaxation times at different angles in different bands, which correctly considers the anisotropy and multiple bands of the system. Note that, for an isotropic single-band system [$\tau^{(i)}_{\boldsymbol{k}\alpha} = \tau(\varepsilon)$ for a given energy $\varepsilon = \varepsilon_{\boldsymbol{k}\alpha}$], Eq. (4.7) is reduced to the well-known expression for the relaxation time given by [40]

$$\frac{1}{\tau_{\boldsymbol{k}}} = \int \frac{d^d k'}{(2\pi)^d} W_{\boldsymbol{k}\boldsymbol{k}'}(1 - \cos\theta_{\boldsymbol{k}\boldsymbol{k}'}). \tag{4.8}$$

The current density $\boldsymbol{J}$ induced by an electric field $\boldsymbol{E}$ is thus given by

$$J^{(i)} = g\sum_{\alpha}\int \frac{d^d k}{(2\pi)^d}(-e) v^{(i)}_{\boldsymbol{k}\alpha}\delta f_{\boldsymbol{k}\alpha} \equiv \sum_{j}\sigma_{ij}E^{(j)}, \tag{4.9}$$

where σ_{ij} is the conductivity tensor given by

$$\sigma_{ij} = ge^2\sum_{\alpha}\int \frac{d^d k}{(2\pi)^d} S^{(0)}(\varepsilon) v^{(i)}_{\boldsymbol{k}\alpha} v^{(j)}_{\boldsymbol{k}\alpha}\tau^{(j)}_{\boldsymbol{k}\alpha}. \tag{4.10}$$

We find that the Hall conductivity ($i \neq j$) vanishes, thus we consider only the diagonal part of the dc conductivity ($i = j$).

4.3 Density dependence of dc conductivity

Using the anisotropic multiband Boltzmann transport theory developed in Sec. 4.2.2, we calculate the dc conductivity of few-layer BP as a function of the carrier

density or Fermi energy at zero temperature for each phase: the semi-Dirac transition point ($\Delta = 0$), gapped insulator phase ($\Delta > 0$), and Dirac semimetal phase ($\Delta < 0$), all of which can be expressed by Eq. (4.1).

As for the impurity potential, we consider two types of impurity scattering: short-range impurities and long-range Coulomb impurities (or charged impurities). Short-range impurities originate from lattice defects, vacancies, dislocations, etc., and their potential form is given by a constant in momentum space, $V_{\boldsymbol{k}\boldsymbol{k}'} = V_{\text{short}}$, as they are approximately represented by the delta function in real space. For charged impurities distributed randomly in the background, the impurity potential is given by $V_{\boldsymbol{k}\boldsymbol{k}'} = \frac{2\pi e^2}{\epsilon(\boldsymbol{q})|\boldsymbol{q}|}$ in 2D, where $\epsilon(\boldsymbol{q})$ is the dielectric function for $\boldsymbol{q} = \boldsymbol{k} - \boldsymbol{k}'$. Within the Thomas–Fermi approximation, $\epsilon(\boldsymbol{q})$ can be approximated as $\epsilon(\boldsymbol{q}) \approx \kappa\,(1 + q_{\text{TF}}/|\boldsymbol{q}|)$, where κ is the background dielectric constant, $q_{\text{TF}} = \frac{2\pi e^2}{\kappa} D(\varepsilon_{\text{F}})$ is the Thomas–Fermi wave vector, and $D(\varepsilon_{\text{F}})$ is the total DOS at the Fermi energy ε_{F} (including all the contributions from the bands crossing ε_{F} and the spin degeneracy). The interaction strength for charged impurities can be characterized by an effective fine structure constant $\alpha_0 = \frac{e^2}{\kappa\hbar v_0}$. Note that $q_{\text{TF}} \propto g\alpha_0$. Thus, the screening strength for Coulomb impurities is also characterized by α_0.

4.3.1 Semi-Dirac transition point

First, let us consider the semi-Dirac transition point ($\Delta = 0$). Figure 4.3 shows the Fermi energy dependence of dc conductivity at the semi-Dirac transition point. The characteristic density or Fermi energy dependence of the dc conductivity can be understood as follows. From Eq. (4.10) with $\tau_{\text{F}}^{(i)} \sim D^{-1}(\varepsilon_{\text{F}})/V_{\text{F}}^2$, we expect $\sigma_{ii} \sim D(\varepsilon_{\text{F}})[v_{\text{F}}^{(i)}]^2\tau_{\text{F}}^{(i)} \sim [v_{\text{F}}^{(i)}]^2/V_{\text{F}}^2$, where $\tau_{\text{F}}^{(i)}$ and $v_{\text{F}}^{(i)}$ are the relaxation time and velocity, respectively, at the Fermi energy along the ith direction, and V_{F}^2 is the angle-averaged squared impurity potential at the Fermi energy.

At the semi-Dirac transition point, $D(\varepsilon_{\rm F}) \sim \varepsilon_{\rm F}^{1/2}$, and the Fermi velocity in each direction is given by $v_{\rm F}^{(x)} \sim \varepsilon_{\rm F}^{1/2}$ and $v_{\rm F}^{(y)} \sim \varepsilon_{\rm F}^{0}$, from which we can deduce the power-law behavior of the dc conductivity. (See Appendix A.1 for the detailed derivations of the power-law dependences.)

For short-range impurities, $V_{\rm F}$ is a constant independent of density; in this case, we obtain

$$\sigma_{xx} \sim \varepsilon_{\rm F} \sim n^{\frac{2}{3}}, \tag{4.11a}$$

$$\sigma_{yy} \sim \varepsilon_{\rm F}^{0} \sim n^{0}. \tag{4.11b}$$

For charged impurities, in the strong screening limit ($g\alpha_0 \gg 1$), $V_{\rm F} \sim q_{\rm TF}^{-1} \sim D^{-1}(\varepsilon_{\rm F}) \sim \varepsilon_{\rm F}^{-\frac{1}{2}}$; thus, we obtain

$$\sigma_{xx} \sim \varepsilon_{\rm F}^{2} \sim n^{\frac{4}{3}}, \tag{4.12a}$$

$$\sigma_{yy} \sim \varepsilon_{\rm F} \sim n^{\frac{2}{3}}. \tag{4.12b}$$

At general screening strength, the power-law behavior is determined by the competition between the screening wave vector and the momentum transfer. We present the numerically calculated power-law behavior for the semi-Dirac transition point and for the other phases in Fig. 4.6.

4.3.2 Insulator phase

Figure 4.4 shows the Fermi energy dependence of the dc conductivity in the insulator phase ($\Delta > 0$). In the insulator phase, the power-law dependence of the dc conductivity at low densities becomes similar to that of 2D electron gas (2DEG) with a different effective mass in each direction. (See Appendix B.3.1 for detailed derivations.)

For short-range impurities, the power-law dependence of the dc conductivity

at low densities is given by

$$\sigma_{xx} \sim \varepsilon_{\mathrm{F}}, \tag{4.13a}$$

$$\sigma_{yy} \sim \varepsilon_{\mathrm{F}}. \tag{4.13b}$$

For charged impurities, in the strong screening limit, at low densities, we obtain

$$\sigma_{xx} \sim \varepsilon_{\mathrm{F}}, \tag{4.14a}$$

$$\sigma_{yy} \sim \varepsilon_{\mathrm{F}}. \tag{4.14b}$$

Note that, as the Fermi energy or the carrier density increases, the power-law dependence becomes similar to that of the semi-Dirac transition point.

4.3.3 Dirac semimetal phase

Figure 4.5 shows the Fermi energy dependence of the dc conductivity in the Dirac semimetal phase ($\Delta < 0$). In the Dirac semimetal phase, the power-law dependence of the dc conductivity at low densities becomes similar to that of graphene but with a different Fermi velocity in each direction. (See Appendix B.3.2 for detailed derivations.)

For short-range impurities, the power-law dependence of the dc conductivity at low densities is given by

$$\sigma_{xx} \sim \varepsilon_{\mathrm{F}}^{0}, \tag{4.15a}$$

$$\sigma_{yy} \sim \varepsilon_{\mathrm{F}}^{0}. \tag{4.15b}$$

For charged impurities, in the strong screening limit, at low densities, we obtain

$$\sigma_{xx} \sim \varepsilon_{\mathrm{F}}^{2}, \tag{4.16a}$$

$$\sigma_{yy} \sim \varepsilon_{\mathrm{F}}^{2}. \tag{4.16b}$$

Near the van Hove singularity, $\varepsilon_{\mathrm{F}} \approx \pm\varepsilon_{\mathrm{g}}/2$, the DOS diverges logarithmically [67] and it dominates the overall power-law behavior of conductivity [69]. Therefore, for short-range impurities, the conductivity becomes

$$\sigma_{xx} \sim [-\log(|\Delta| - \varepsilon_{\mathrm{F}})]^{-1}, \tag{4.17a}$$

$$\sigma_{yy} \sim [-\log(|\Delta| - \varepsilon_{\mathrm{F}})]^{-1}. \tag{4.17b}$$

For charged impurities, due to the dominant contribution from the diverging Thomas–Fermi wave vector $q_{\mathrm{TF}} \propto D(\varepsilon_{\mathrm{F}})$, the conductivity is largely given by the square of the DOS as follows:

$$\sigma_{xx} \sim [\log(|\Delta| - \varepsilon_{\mathrm{F}})]^{2}, \tag{4.18a}$$

$$\sigma_{yy} \sim [\log(|\Delta| - \varepsilon_{\mathrm{F}})]^{2}. \tag{4.18b}$$

As the Fermi energy or the carrier density increases further, the power-law dependence of the dc conductivity becomes similar to that of the semi-Dirac transition point, as in the insulator phase.

Figure 4.6 shows the evolution of the Fermi-energy power law of the dc conductivity as a function of the screening strength α_0 for each phase in the low carrier density limit. For the insulator phase and the semi-Dirac transition point, the Fermi-energy exponent decreases, whereas for the Dirac semimetal phase, it shows a non-monotonic behavior with a dip structure, which originates from the interband-like scattering between two distinct Fermi surfaces shown in Fig. 4.1(f). As the screening strength increases, all the Fermi-energy exponents approach the corresponding power law estimated in the strong screening limit.

4.4 Temperature dependence of dc conductivity

We can apply the anisotropic multiband Boltzmann transport theory developed in Sec. 4.2.2 to the dc conductivity at finite temperature. In Eq. (4.10), the fi-

nite temperature affects the conductivity through the Fermi distribution and the temperature-dependent screening for the charged impurity potential. At finite temperatures, the chemical potential of the system also deviates from the Fermi energy ε_{F} due to the broadening of the Fermi distribution function. From the invariance of carrier density n with respect to temperature T, we obtain the temperature dependence of the chemical potential $\mu(T)$. For charged impurities, the finite temperature Thomas–Fermi screening wave vector is given by $q_{\mathrm{TF}}(T) = \frac{2\pi e^2}{\kappa}\frac{\partial n}{\partial \mu}$ for 2D systems. (See Appendix B.4 for the detailed derivation of the temperature dependence of the chemical potential and Thomas–Fermi wave vector). In this section, we calculate the dc conductivity of few-layer BP as a function of the temperature for each phase. The detailed derivation of the temperature-dependent conductivity is presented in Appendices B.5 and B.6.

4.4.1 Semi-Dirac transition point

From the power-law dependence of the DOS, $D(\varepsilon) \sim \varepsilon^{1/2}$ at the semi-Dirac transition point [Fig. 4.2(a)], we can obtain the asymptotic behaviors of $\mu(T)$ and $q_{\mathrm{TF}}(T)$ in a relatively straightforward manner. In the low- and high-temperature limits, the chemical potential at the semi-Dirac transition point is given by

$$\frac{\mu}{\varepsilon_{\mathrm{F}}} = \begin{cases} 1 - \frac{\pi^2}{12}\left(\frac{T}{T_{\mathrm{F}}}\right)^2 & (T \ll T_{\mathrm{F}}), \\ \frac{1}{2\eta\left(\frac{1}{2}\right)\Gamma\left(\frac{5}{2}\right)}\left(\frac{T}{T_{\mathrm{F}}}\right)^{\frac{1}{2}} & (T \gg T_{\mathrm{F}}), \end{cases} \tag{4.19}$$

whereas the Thomas–Fermi wave vector is given by

$$\frac{q_{\mathrm{TF}}(T)}{q_{\mathrm{TF}}(0)} = \begin{cases} 1 - \frac{\pi^2}{12}\left(\frac{T}{T_{\mathrm{F}}}\right)^2 & (T \ll T_{\mathrm{F}}), \\ 2\eta\left(\frac{1}{2}\right)\Gamma\left(\frac{3}{2}\right)\left(\frac{T}{T_{\mathrm{F}}}\right)^{\frac{1}{2}} & (T \gg T_{\mathrm{F}}), \end{cases} \tag{4.20}$$

where Γ is the Gamma function and η is the Dirichlet eta function [45]. In a single-band system, $q_{\mathrm{TF}}(T)$ typically decreases with the temperature at high

temperatures, whereas at the semi-Dirac transition point, $q_{\mathrm{TF}}(T)$ increases with the temperature due to the thermal excitation of carriers participating in the screening.

Figure 4.7 shows the temperature dependence of the dc conductivity at the semi-Dirac transition point, normalized by the zero-temperature conductivity value in each direction. For short-range impurities, we determine that the asymptotic behavior is given by

$$\frac{\sigma_{xx}(T)}{\sigma_{xx}(0)} = \begin{cases} 1 - \frac{\pi^2}{12}\left(\frac{T}{T_{\mathrm{F}}}\right)^2 & (T \ll T_{\mathrm{F}}), \\ \log 2 \left(\frac{T}{T_{\mathrm{F}}}\right) & (T \gg T_{\mathrm{F}}), \end{cases} \tag{4.21a}$$

$$\frac{\sigma_{yy}(T)}{\sigma_{yy}(0)} = \begin{cases} 1 - e^{-T_{\mathrm{F}}/T} & (T \ll T_{\mathrm{F}}), \\ \frac{1}{2} + \frac{1}{8\eta\left(\frac{1}{2}\right)\Gamma\left(\frac{5}{2}\right)}\left(\frac{T}{T_{\mathrm{F}}}\right)^{-\frac{3}{2}} & (T \gg T_{\mathrm{F}}). \end{cases} \tag{4.21b}$$

For charged impurities, the asymptotic behavior is given by

$$\frac{\sigma_{xx}(T)}{\sigma_{xx}(0)} = \begin{cases} 1 + C_{xx}\left(\frac{T}{T_{\mathrm{F}}}\right)^2 & (T \ll T_{\mathrm{F}}), \\ D_{xx}\left(\frac{T}{T_{\mathrm{F}}}\right)^2 & (T \gg T_{\mathrm{F}}), \end{cases} \tag{4.22a}$$

$$\frac{\sigma_{yy}(T)}{\sigma_{yy}(0)} = \begin{cases} 1 + C_{yy}\left(\frac{T}{T_{\mathrm{F}}}\right)^2 & (T \ll T_{\mathrm{F}}), \\ D_{yy}\left(\frac{T}{T_{\mathrm{F}}}\right) & (T \gg T_{\mathrm{F}}), \end{cases} \tag{4.22b}$$

where C_{ii} (D_{ii}) indicates the low- (high-) temperature coefficients. In the strong screening limit, the coefficients become $C_{xx} = 0$, $D_{xx} = \frac{\pi^2}{6}$, $C_{yy} = -\frac{\pi^2}{4}$, and $D_{yy} = \log 2$. As the screening strength decreases, the high-temperature coefficients D_{ii} remain positive, whereas the low-temperature coefficients C_{ii} decrease and we expect that the initially negative or vanishing C_{ii} would eventually become positive in the weak screening limit. (See Appendix B.5 for the detailed derivations of the coefficients C_{ii} and D_{ii}.)

The temperature dependence in the high-temperature limit can be easily

understood by replacing ε_{F} with T in the Fermi energy dependence of dc conductivity [Eqs. (4.11) and (4.12)]. At high temperatures, $\sigma_{yy}(T)$ for short-range impurities decreases with the temperature, showing a metallic behavior. Otherwise, the conductivities increase with the temperature, showing an insulating behavior. Note that the high-temperature asymptotic form for charged impurities is obtained by considering the effect of the energy averaging and that of the temperature-dependent screening separately. It correctly predicts the temperature power-law dependence but not the coefficients in the asymptotic form, showing a discrepancy with the numerical result, as the effect of temperature cannot be simply separated into the energy averaging and the temperature-dependent screening at high temperatures.

4.4.2 Insulator phase

Figure 4.8 shows the temperature dependence of the dc conductivity in the insulator phase with the fixed Fermi energy of $\varepsilon_{\mathrm{F}} = 1.1\varepsilon_0$, which corresponds to the low-density limit. At zero temperature, the insulator phase in the low-density limit can be effectively considered as a gapped 2DEG (with anisotropic effective masses). Similarly, at finite temperatures, the temperature-dependent conductivity of the insulator phase in the low-density limit resembles that of the gapped 2DEG system (blue dash-dotted lines in Fig. 4.8), especially in the low-temperature limit. In the high-temperature limit, the power-law behavior of the temperature-dependent conductivity for the insulator phase becomes similar to that of the semi-Dirac transition point [Eqs. (4.21) and (4.22)], because thermally excited carriers above the gap contribute to the conductivity. (See Appendix B.6 for the temperature dependence of the chemical potential, Thomas–Fermi screening wave vector, and conductivity of the gapped 2DEG system.)

In the high-density limit, the temperature dependence of dc conductivity in the insulator phase resembles that of the semi-Dirac transition point.

4.4.3 Dirac semimetal phase

Figure 4.9 shows the calculated temperature-dependent conductivity in the Dirac semimetal phase, with the fixed Fermi energy of $\varepsilon_{\mathrm{F}} = 0.01\varepsilon_0$, which corresponds to the low-density limit. At low densities, the Dirac semimetal phase can be effectively considered as graphene (with anisotropic velocities); thus, we can understand its temperature-dependent conductivity behavior using the result of graphene. (See Appendix B.6 for the temperature dependence of the chemical potential, Thomas–Fermi screening wave vector, and conductivity of graphene.) For graphene with short-range impurities, the asymptotic form of the temperature-dependent conductivity becomes

$$\frac{\sigma_{\mathrm{gp}}(T)}{\sigma_{\mathrm{gp}}(0)} = \begin{cases} 1 - e^{-T_{\mathrm{F}}/T} & (T \ll T_{\mathrm{F}}), \\ \frac{1}{2} + \frac{1}{16\log 2}\left(\frac{T}{T_{\mathrm{F}}}\right)^{-2} & (T \gg T_{\mathrm{F}}), \end{cases} \tag{4.23}$$

whereas for charged impurities in the strong screening limit, the asymptotic form of the temperature-dependent conductivity becomes

$$\frac{\sigma_{\mathrm{gp}}(T)}{\sigma_{\mathrm{gp}}(0)} = \begin{cases} 1 - \frac{\pi^2}{3}\left(\frac{T}{T_{\mathrm{F}}}\right)^2 & (T \ll T_{\mathrm{F}}), \\ \frac{\pi^2}{6}\left(\frac{T}{T_{\mathrm{F}}}\right)^2 & (T \gg T_{\mathrm{F}}). \end{cases} \tag{4.24}$$

Similar to the result of the semi-Dirac transition point, the high-temperature asymptotic form for charged impurities correctly captures the temperature power-law dependence (but not the exact coefficient value, as discussed in Sec. 4.4.1).

Figure 4.10 shows the temperature dependence of the dc conductivity in the Dirac semimetal phase immediately below the van Hove singularity point,

exhibiting a nonmonotonic behavior with temperature. As explained earlier, the temperature dependence of the dc conductivity is determined by the energy averaging with $S^{(0)}(\varepsilon)$ broadened by temperature, and by the temperature-dependent screening for charged impurities. Thus, if the Fermi energy is near the van Hove singularity, the distance between the Fermi energy and the van Hove singularity sets an important energy scale for the temperature dependence, $k_{\rm B}T_1 \equiv ||\varepsilon_{\rm F}| - |\varepsilon_{\rm g}||$. For charged impurities, the conductivity first increases, showing a peak at T_1, and thereafter decreases, showing a dip at $T_2^{\rm ch} \sim 0.5T_{\rm F}$ corresponding to the minimum of $q_{\rm TF}(T)$, mainly following the temperature dependence of the screening wave vector $q_{\rm TF}(T)$ [Fig. B.3(e) in the Appendix]. For short-range impurities, the conductivity first decreases, showing a dip at T_1, and thereafter increases, showing a peak at $T_2^{\rm sh} \sim 0.25T_{\rm F}$. These dips and peaks are from the temperature-dependent evolution of the chemical potential $\mu(T)$ [Fig. B.3(b) in the Appendix], shifting the central point of the energy averaging.

In the high-density limit, the temperature dependence of dc conductivity in the Dirac semimetal phase resembles that of the semi-Dirac transition point.

4.5 Discussion and conclusion

When we consider both short-range and charged impurities, assuming that each scattering mechanism is independent, the total scattering rate is obtained by adding their scattering rates in accordance with Matthiessen's rule. Note that the scattering mechanism with a higher scattering rate (or equivalently a lower conductivity) dominates the resulting conductivity. From the obtained Fermi-energy power-law dependence of dc conductivity, we can determine the dominant scattering mechanism. At the semi-Dirac transition point, we can ob-

serve from Eq. (4.11) and Figs. 4.6(a) and (d) that, for both σ_{xx} and σ_{yy}, the Fermi-energy power law for short-range impurities is always smaller than that of charged impurities. This indicates that, at low densities, charged impurities are dominant over short-range impurities, whereas at high densities, short-range impurities are dominant over charged impurities. In the insulator phase, at low densities, the system can be approximated as a 2DEG and the Fermi-energy power laws for short-range and charged impurities are almost comparable (except in the no-screening limit) as shown in Eq. (4.13) and Figs. 4.6(b) and (e). At high densities, the power-law dependence follows that of the semi-Dirac transition point; thus, short-range impurities dominate over charged impurities. In the Dirac semimetal phase, at low densities, the Fermi-energy power law for short-range impurities is always smaller than that of charged impurities as shown in Eq. (4.15) and Figs. 4.6(c) and (f); thus, charged impurities are dominant over short-range impurities as in the case of graphene. At high densities, short-range impurities become dominant over charged impurities, following the trend of the semi-Dirac transition point. Note that, near the van Hove singularities, charged impurities are highly screened due to the enhanced DOS, and thus, short-range impurities are dominant over charged impurities [69].

Our analysis is based on the semiclassical Boltzmann transport theory, which is known to be valid in the high-density limit. At low densities, the effect of potential fluctuations induced by spatially inhomogeneous impurities becomes important, which is not captured by our approach assuming a spatially homogeneous system. At the semi-Dirac transition point or in the Dirac semimetal phase, the potential fluctuation is expected to result in a minimum conductivity [31, 71, 72]. In the insulator phase, if the band gap is sufficiently large, the effect of the potential fluctuation might be limited. The interplay

of the impurity potential fluctuation, temperature, and band gap would be an interesting future research direction.

Finally, we wish to mention the additional parabolic term $\gamma\frac{\hbar^2 k_y^2}{2m^*}\sigma_x$ omitted in Eq. (4.1) along the armchair (y) direction beyond the lowest order [73]. This term could affect the dc conductivity, especially at high densities above the crossover Fermi energy $\varepsilon_{\rm F}^{\rm cr} = \frac{2m^* v^2}{\gamma}$, where the effective Hamiltonian in Eq. (4.1) is no longer valid. For example, at the semi-Dirac transition point with $\varepsilon_{\rm F} \gg \varepsilon_{\rm F}^{\rm cr}$, the parabolic term becomes dominant over the linear term along the armchair direction; thus, σ_{xx} and σ_{yy} will follow those of (anisotropic) 2DEG.

In summary, we calculate the dc conductivity of few-layer BP as a function of the density and temperature using the anisotropic multiband Boltzmann transport theory, which is essential when the effect of anisotropic energy dispersion or interband scattering becomes important. We find that the dc conductivities in the Boltzmann limit show characteristic density and temperature dependence in each phase, which could be used as a signature of the tunable electronic structure of BP in transport measurements.

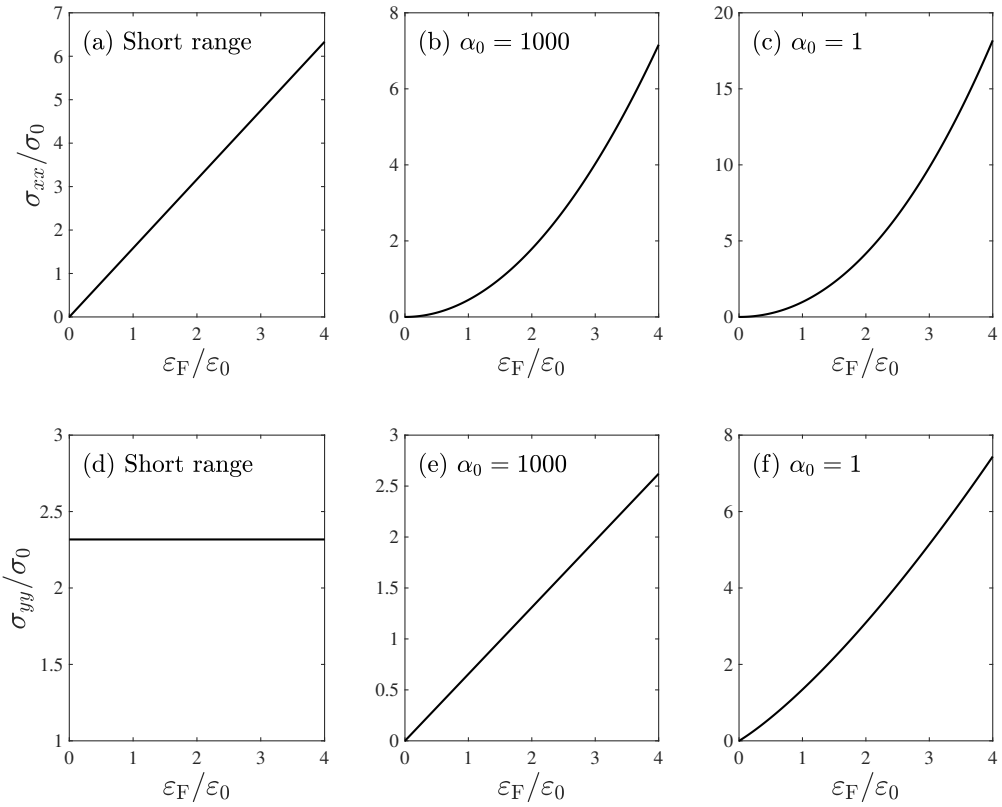

Figure 4.3 Calculated dc conductivities (a)-(c) σ_{xx} and (d)-(f) σ_{yy} as a function of Fermi energy at the semi-Dirac transition point ($\Delta = 0$) for (a), (d) short-range impurities, (b), (d) charged impurities with $\alpha_0 = 1000$, and (c), (f) charged impurities with $\alpha_0 = 1$. Here, $\sigma_0 = \frac{ge^2k_0^2c^2}{2\pi\hbar n_{\rm imp}}$.

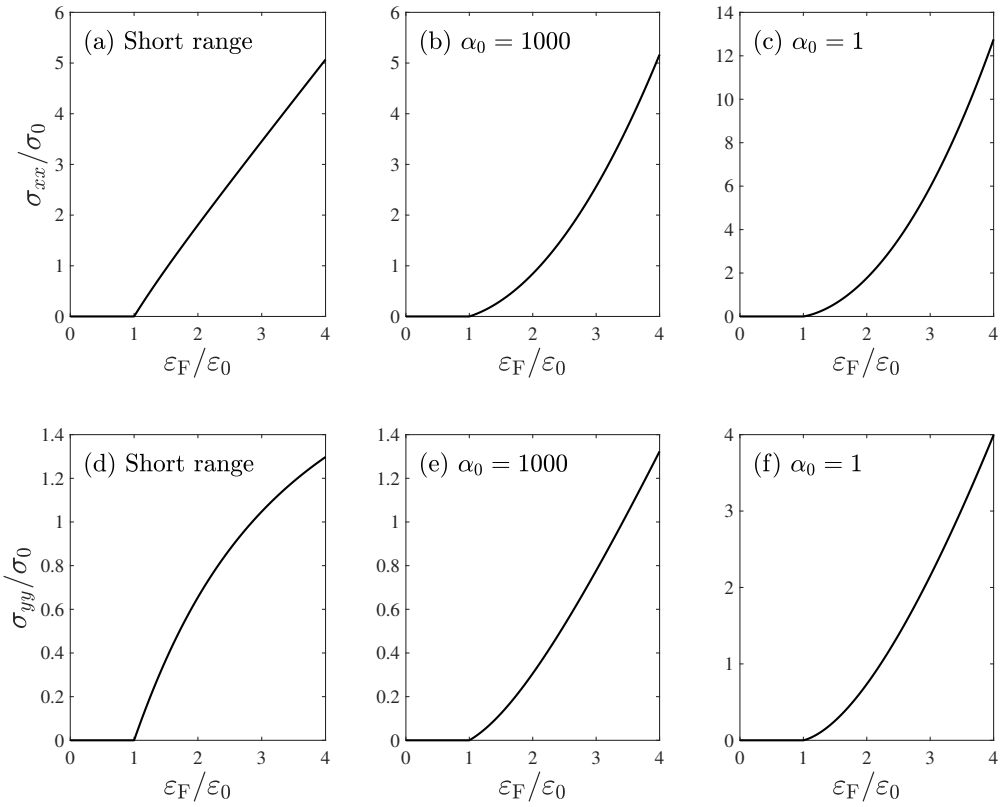

Figure 4.4 Calculated dc conductivities (a)-(c) σ_{xx} and (d)-(f) σ_{yy} as a function of Fermi energy in the insulator phase with $\Delta = 1$ for (a), (d) short-range impurities, (b), (d) charged impurities with $\alpha_0 = 1000$, and (c), (f) charged impurities with $\alpha_0 = 1$.

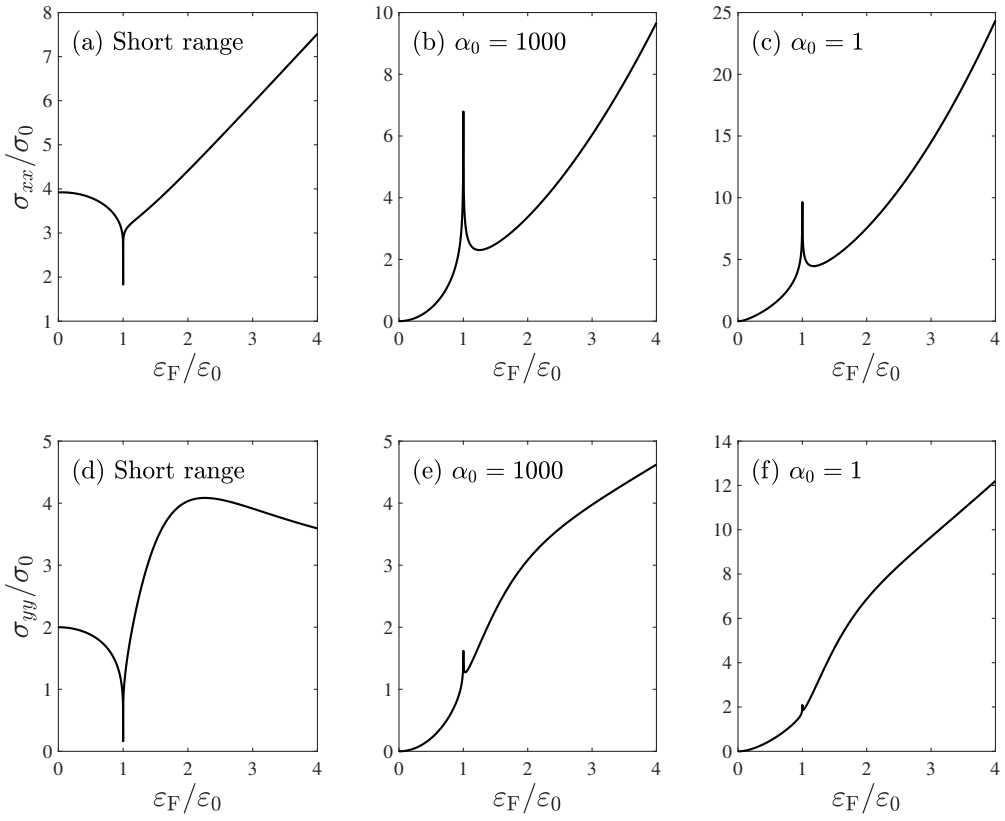

Figure 4.5 Calculated dc conductivities (a)-(c) σ_{xx} and (d)-(f) σ_{yy} as a function of Fermi energy in the Dirac semimetal phase with $\Delta = -1$ for (a), (d) short-range impurities, (b), (d) charged impurities with $\alpha_0 = 1000$, and (c), (f) charged impurities with $\alpha_0 = 1$.

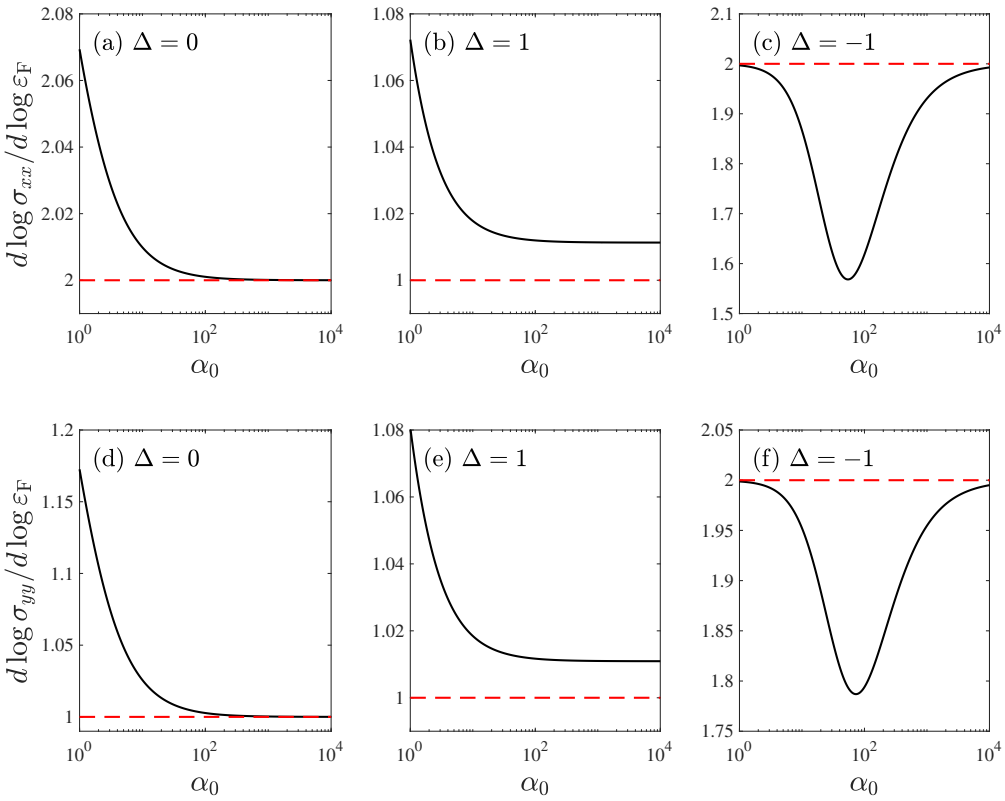

Figure 4.6 (a)-(c) $d\log\sigma_{xx}/d\log\varepsilon_{\mathrm{F}}$ and (d)-(f) $d\log\sigma_{yy}/d\log\varepsilon_{\mathrm{F}}$ as a function of α_0 for charged impurities in each phase. The red dashed lines represent the Fermi energy exponents obtained in the strong screening limit. Here, $\varepsilon_{\mathrm{F}} = \varepsilon_0$ for the semi-Dirac transition point, $\varepsilon_{\mathrm{F}} = 1.01\varepsilon_0$ for the gapped insulator phase, and $\varepsilon_{\mathrm{F}} = 0.01\varepsilon_0$ for the Dirac phase are used for the calculation.

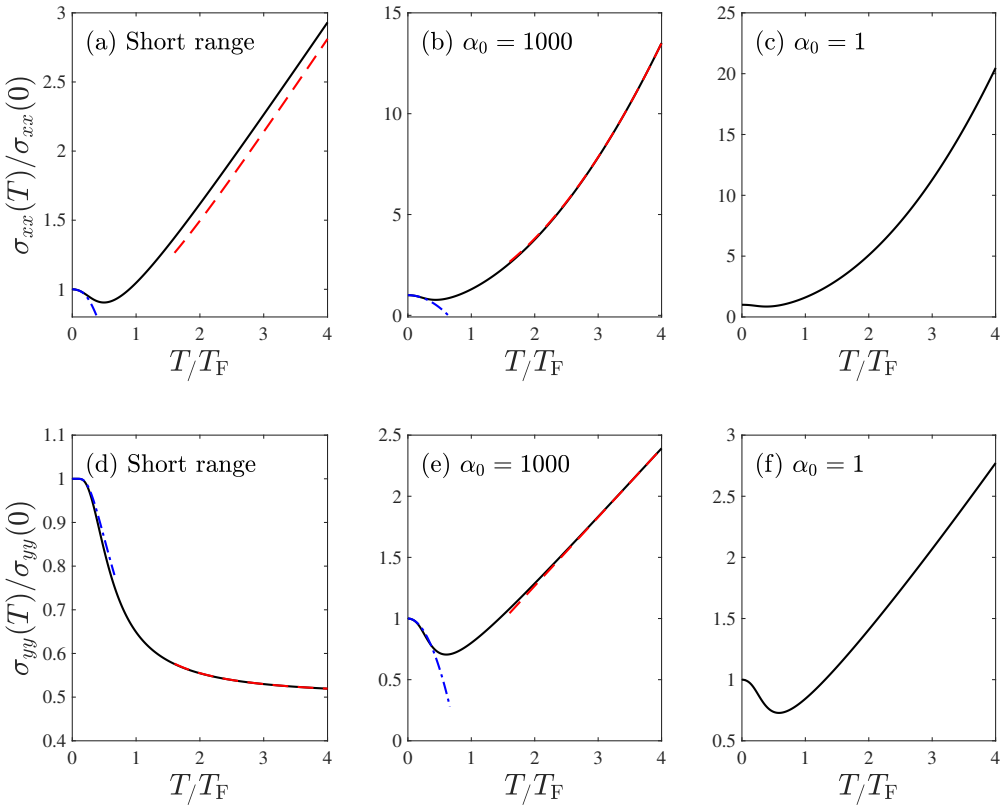

Figure 4.7 Calculated dc conductivities (a)-(c) σ_{xx} and (d)-(f) σ_{yy} as a function of the temperature at the semi-Dirac transition point ($\Delta = 0$) for (a), (d) short-range impurities, (b), (d) charged impurities with $\alpha_0 = 1000$, and (c), (f) charged impurities with $\alpha_0 = 1$. Here, if the temperature is normalized by $T_{\mathrm{F}} = \varepsilon_{\mathrm{F}}/k_{\mathrm{B}}$, the result is independent of ε_{F} at the semi-Dirac transition point. The blue dashed-dotted lines and red dashed lines represent fitting by the corresponding asymptotic form [Eqs. (4.21) and (4.22)] in the low- and high-temperature limits, respectively.

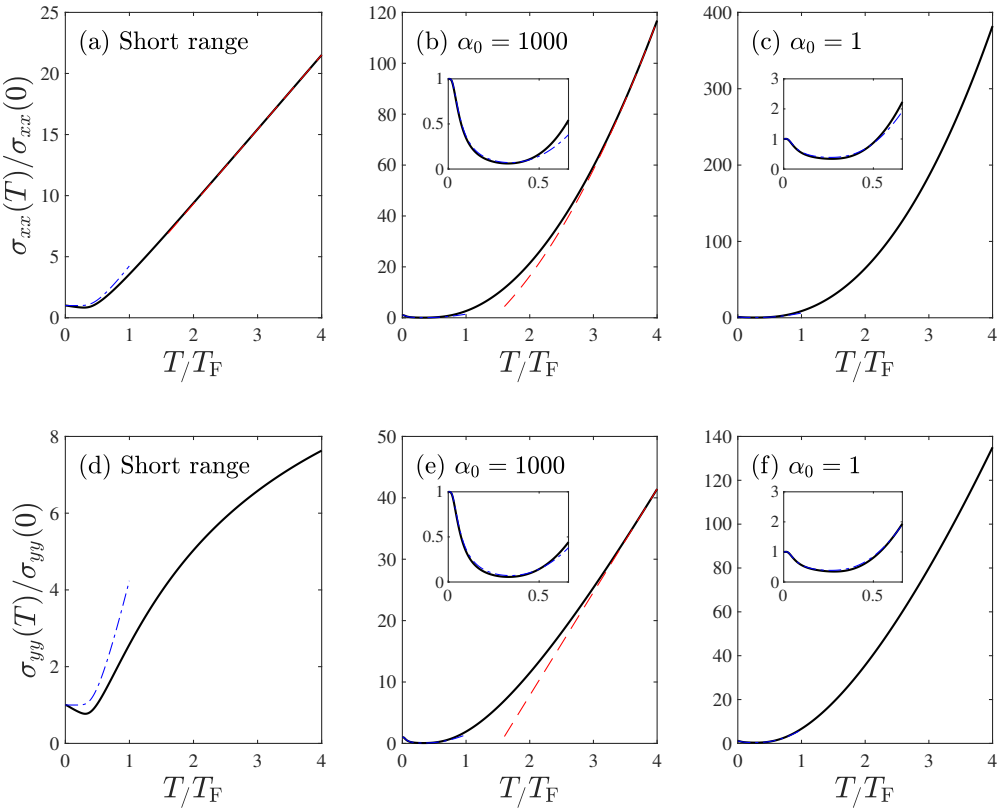

Figure 4.8 Calculated dc conductivities (a)-(c) σ_{xx} and (d)-(f) σ_{yy} in the low-density limit as a function of the temperature in the insulator phase with $\Delta = 1$ for (a), (d) short-range impurities, (b), (d) charged impurities with $\alpha_0 = 1000$, and (c), (f) charged impurities with $\alpha_0 = 1$. Here, $\varepsilon_{\rm F} = 1.1\varepsilon_0$ is used for the calculation. The blue dashed-dotted lines represent the result for the gapped 2DEG system (see Appendix B.6), and the red dashed lines represent power-law fitting by the asymptotic form of the semi-Dirac transition point [Eqs. (4.21) and (4.22)] in the high-temperature limit.

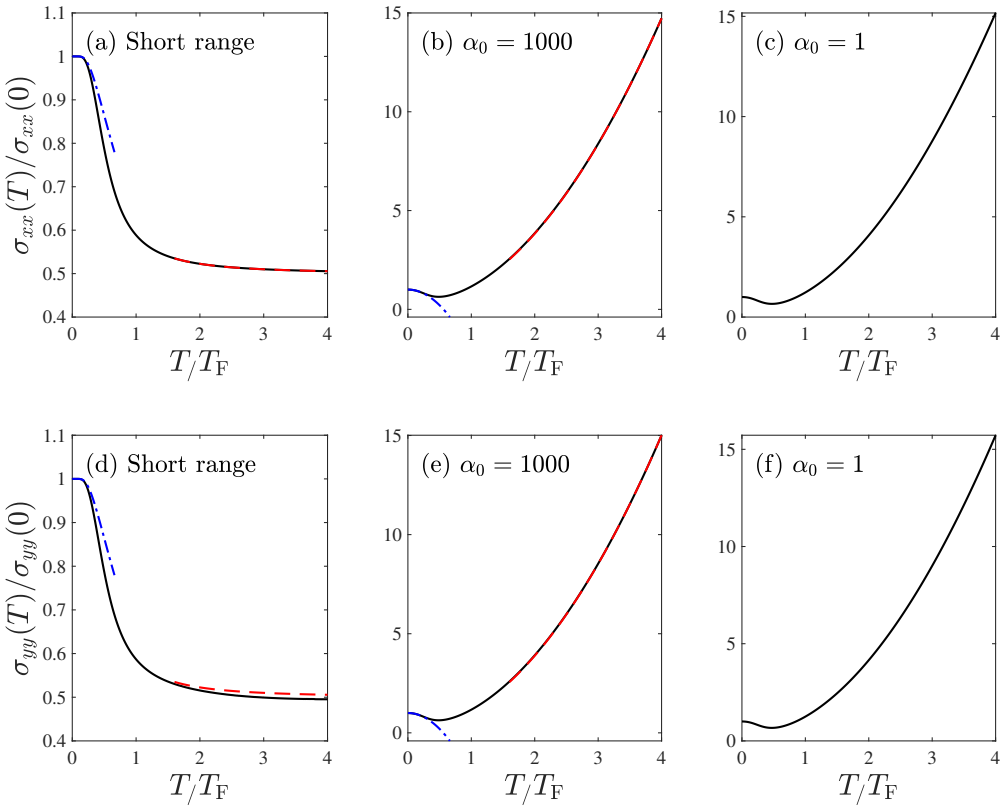

Figure 4.9 Calculated dc conductivities (a)-(c) σ_{xx} and (d)-(f) σ_{yy} in the low-density limit as a function of the temperature in the Dirac semimetal phase with $\Delta = -1$ for (a), (d) short-range impurities, (b), (d) charged impurities with $\alpha_0 = 1000$, and (c), (f) charged impurities with $\alpha_0 = 1$. Here, $\varepsilon_{\rm F} = 0.01\varepsilon_0$ is used for the calculation. The blue dashed-dotted lines and red dashed lines represent fitting by the corresponding asymptotic form [Eqs. (4.23) and (4.24)] in the low- and high-temperature limits, respectively.

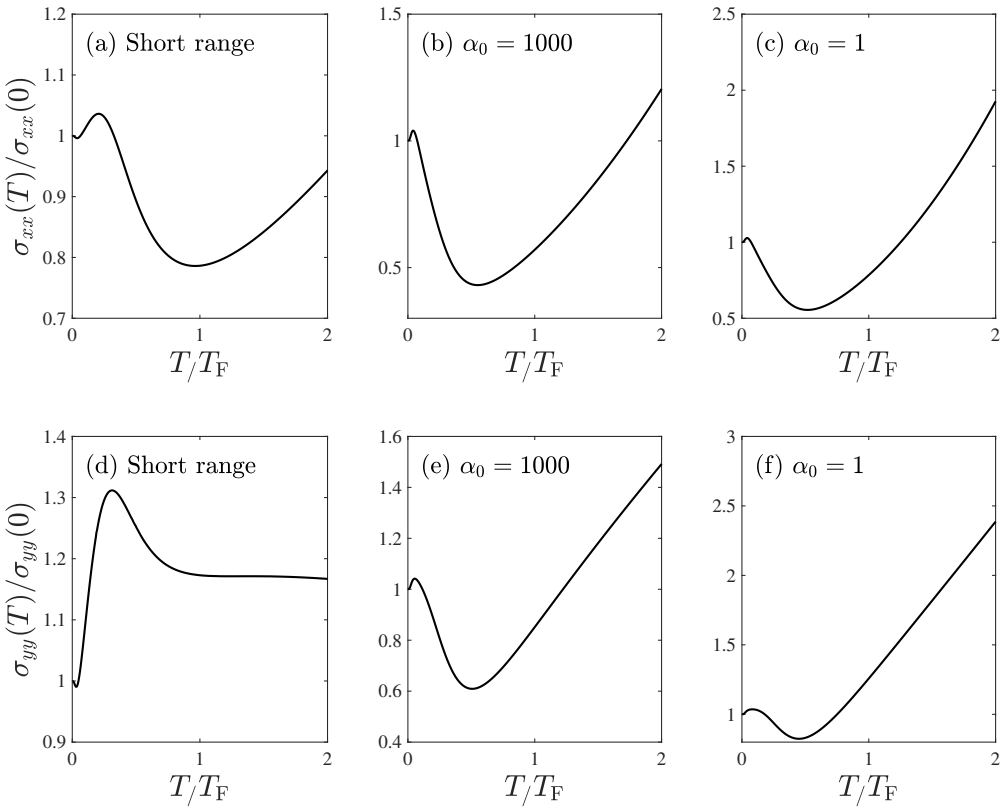

Figure 4.10 Calculated dc conductivities (a)–(c) σ_{xx} and (d)–(f) σ_{yy} immediately below the van Hove singularity point as a function of the temperature in the Dirac semimetal phase with $\Delta = 1$ for (a), (d) short-range impurities, (b), (d) charged impurities with $\alpha_0 = 1000$, and (c), (f) charged impurities with $\alpha_0 = 1$. Here, $\varepsilon_{\mathrm{F}} = 0.9\varepsilon_0$ is used for the calculation.

Chapter 5

Semiclassical Boltzmann magnetotransport theory in anisotropic systems with a nonvanishing Berry curvature

5.1 Introduction

The magnetic field effect on the transport behavior has always been a significant topic to study in the condensed matter physics. By adding another tuning knob (magnetic field) to the electronic transport experiment, we can essentially gain another dimension to our understanding on the material of interest. In this regard, the magnetotransport measurement done on a system can be a great tool to reveal many fascinating features that the material hides. The quantum Hall effect [74], for example, which is one of the most important discoveries in the last century, has been brought to light by magnetoresistance experiments.

Especially, the topological materials with nonvanishing Berry curvature such as Weyl semimetals or topological insulators display many interesting magne-

totransport behaviors such as negative magnetoresistance (MR). The negative MR in Weyl semimetals [10, 16, 75–89] along with the negative MR in topological insulators [90–100] have received a great amount of attention over the last decade. Not only the negative MR behavior, but the magnetotransport research in general on the topological materials, e.g. Weyl semimetals, multi-Weyl semimetals, or topological insulators, have also enjoyed a fair share of awareness. These magnetoresistance researches mostly fall under either one of two categories: strong magnetic field regime where the Landau level limited quantum magnetotransport is predominant [101–108], or the weak magnetic field regime where the charge transport can be described by the semiclassical formalism [36, 75, 76, 109–122].

Most of the works that studied the semiclassical magnetotransport theory utilize the simple isotropic relaxation time approximation. However, this practice can turn out to be problematic when the band dispersion of the system is highly anisotropic and the system can no longer be approximated to be an isotropic system. Furthermore, in a magnetotransport context, this isotropic approximation can induce another trouble of not being able to account for the anisotropy that arises from the coupling between the magnetic field and the Berry curvature. Fundamentally, we are faced with two different sources of anisotropy that can affect the electronic transport: the band dispersion-originated anisotropy and the magnetic field-driven anisotropy. We believe that laying foundations on how to properly study these anisotropies of the system is one of the mainstays in the semiclassical magnetotransport theory, be it from the band dispersion anisotropy or the field-driven anisotropy that arises from the Berry curvature coupling with the magnetic field.

With these motivations, we formulate the fully anisotropic Boltzmann magnetotransport equation that incorporates the energy dispersion-originated anisotropy

as well as the magnetic field-driven anisotropy. Although there has been some studies that considered field-dependent anisotropic relaxation time [16, 123], our approach utilizes more generally applicable form in calculating the relaxation time itself. We expanded the relaxation time into anisotropic, direction-dependent formalism and built the transport theory with minimum amount of assumptions. We solve the Boltzmann equation and calculate the nonequilibrium distribution function by introducing an ansatz that encompasses the electric field, the magnetic field, and the Berry curvature effect coherently. Our method can be applied to any configuration of magnetic field, not just parallel or perpendicular to the electric field direction, as long as the field strength is weak enough that the semiclassical approximation is valid. We calculate the anisotropic relaxation time that is defined by the impurity scattering, and suggest the method to obtain the magnetoconductivity with the anisotropic relaxation time.

This chapter is organized as follows. We summarize the isotropic Boltzmann magnetotransport equation for the systems without the Berry curvature and demonstrate the relaxation time equation in the electron gas system in Sec. 5.2. Then in Sec. 5.3, we present our main result, which is the Boltzmann transport equation that can be applied in the systems with the intrinsic anisotropy as well as the magnetic field-driven anisotropy. We follow that up with the conductivity equations in Sec. 5.4, and finally, we conclude our chapter in Sec. 5.5 with discussions.

5.2 Magnetotransport equation in electron gas systems

First, we recapitulate the magnetotransport relaxation time equation for an isotropic electron gas without the Berry curvature [124]. In this case, the equation of motion takes a simple form [40]:

$$\dot{\boldsymbol{r}} = \boldsymbol{v}_{\boldsymbol{k}} \tag{5.1}$$

$$\hbar\dot{\boldsymbol{k}} = q\boldsymbol{E} + \frac{q}{c}\boldsymbol{v}_{\boldsymbol{k}} \times \boldsymbol{B}, \tag{5.2}$$

where $\boldsymbol{r}$ is the three-dimensional (3D) position vector, $\boldsymbol{k}$ is the crystal momentum, q is the electric charge, $\boldsymbol{E}$ is the electric field, $\boldsymbol{B}$ is the magnetic field, $\boldsymbol{v}_{\boldsymbol{k}} = \frac{1}{\hbar}\nabla_{\boldsymbol{k}}\tilde{\varepsilon}_{\boldsymbol{k}}$, $\tilde{\varepsilon}_{\boldsymbol{k}} \equiv \varepsilon_{\boldsymbol{k}} - \boldsymbol{m}_{\boldsymbol{k}} \cdot \boldsymbol{B}$, $\varepsilon_{\boldsymbol{k}} = \frac{\hbar k^2}{2m}$ is the electronic band dispersion relation of an electron gas, m is the effective mass of an electron, and $\boldsymbol{m}_{\boldsymbol{k}}$ is the orbital magnetic moment, which vanishes for a single-band electron gas with no Berry curvature [109, 125–128].

The Boltzmann transport equation can be written as

$$\frac{df}{dt} = \left(\frac{df}{dt}\right)_{\text{coll}}, \tag{5.3}$$

where f is the nonequilibrium distribution function, and $\frac{df}{dt}$ is the equation of motion given by

$$\frac{df}{dt} = \frac{\partial f}{\partial t} + \dot{\boldsymbol{r}} \cdot \nabla_{\boldsymbol{r}} f + \dot{\boldsymbol{k}} \cdot \nabla_{\boldsymbol{k}} f, \tag{5.4}$$

with $f_{\boldsymbol{k}} = f^{(0)}_{\boldsymbol{k}} + g_{\boldsymbol{k}}$ ($f^{(0)}_{\boldsymbol{k}}$ is the equilibrium Fermi-Dirac distribution function and $g_{\boldsymbol{k}}$ is the part where the field-dependent terms are contained), and $\left(\frac{df}{dt}\right)_{\text{coll}}$ is the collision integral term which is given by

$$\left(\frac{df}{dt}\right)_{\text{coll}} = -\int \frac{d^d k'}{(2\pi)^d} W_{\boldsymbol{k}'\boldsymbol{k}} \left(g_{\boldsymbol{k}} - g_{\boldsymbol{k}'}\right), \tag{5.5}$$

where $d = 3$ is the dimension of the system, $W_{\boldsymbol{k}'\boldsymbol{k}} = \frac{2\pi}{\hbar} n_{\text{imp}} |V_{\boldsymbol{k}'\boldsymbol{k}}|^2 \delta(\varepsilon_{\boldsymbol{k}'} - \varepsilon_{\boldsymbol{k}})$ is the transition rate given by the Fermi's golden rule, with the impurity potential $V_{\boldsymbol{k}'\boldsymbol{k}}$, the impurity density n_{imp} and $\delta(\varepsilon_{\boldsymbol{k}})$ is the Dirac delta function.

Now, we assume that f is spatially homogeneous (in this case, no temperature gradient or nonuniform electric field) and there is no explicit time dependence. Then the Eq. (5.3) becomes

$$\frac{df}{dt} = \dot{\boldsymbol{k}} \cdot \nabla_{\boldsymbol{k}} f = \left(\frac{df}{dt} \right)_{\text{coll}}. \tag{5.6}$$

Noting that $f^{(0)}_{\boldsymbol{k}} = f^{(0)}(\varepsilon_{\boldsymbol{k}})$, the nonequilibrium distribution function $f_{\boldsymbol{k}}$ and its $\boldsymbol{k}$ gradient can be written as

$$\nabla_{\boldsymbol{k}} f_{\boldsymbol{k}} = \nabla_{\boldsymbol{k}} f^{(0)}_{\boldsymbol{k}} + \nabla_{\boldsymbol{k}} g_{\boldsymbol{k}} = \hbar \boldsymbol{v}_{\boldsymbol{k}} \frac{\partial f^{(0)}_{\boldsymbol{k}}}{\partial \varepsilon_{\boldsymbol{k}}} + \nabla_{\boldsymbol{k}} g_{\boldsymbol{k}}, \tag{5.7}$$

Then the equation of motion becomes

$$\begin{aligned} &-\hbar \dot{\boldsymbol{k}} \cdot \boldsymbol{v}_{\boldsymbol{k}} S^{(0)}(\varepsilon) + \dot{\boldsymbol{k}} \cdot \nabla_{\boldsymbol{k}} g_{\boldsymbol{k}} \\ &= -q \boldsymbol{E} \cdot \boldsymbol{v}_{\boldsymbol{k}} S^{(0)}(\varepsilon) + \frac{q}{\hbar c} (\boldsymbol{v}_{\boldsymbol{k}} \times \boldsymbol{B}) \cdot \nabla_{\boldsymbol{k}} g_{\boldsymbol{k}}, \end{aligned} \tag{5.8}$$

where $S^{(0)}(\varepsilon) \equiv -\frac{\partial f^{(0)}_{\boldsymbol{k}}}{\partial \varepsilon_{\boldsymbol{k}}}$, and we neglected the higher-order electric field terms. Then the Boltzmann equation becomes

$$\begin{aligned} &q \boldsymbol{E} \cdot \boldsymbol{v}_{\boldsymbol{k}} S^{(0)}(\varepsilon) - \frac{q}{\hbar c} (\boldsymbol{v}_{\boldsymbol{k}} \times \boldsymbol{B}) \cdot \nabla_{\boldsymbol{k}} g_{\boldsymbol{k}} \\ &= \int \frac{d^d k'}{(2\pi)^d} W_{\boldsymbol{k}'\boldsymbol{k}} \left(g_{\boldsymbol{k}} - g_{\boldsymbol{k}'} \right). \end{aligned} \tag{5.9}$$

How would we define and calculate the additional term $g_{\boldsymbol{k}}$ is the main concern in solving the Boltzmann equation. When there is no magnetic field present, we often utilize the simple relaxation time equation, i.e. $-\frac{g_{\boldsymbol{k}}}{\tau_{\boldsymbol{k}}} = \left(\frac{df}{dt} \right)$, where we assume the system relaxes back to the equilibrium from the impurity scattering

with the relaxation time $\tau_{\boldsymbol{k}}$. We extend the relaxation time equation to incorporate the additional contribution from the magnetic field so the additional term $g_{\boldsymbol{k}}$ is given by

$$\begin{aligned} g_{\boldsymbol{k}} &= q\boldsymbol{E}\cdot\boldsymbol{v}_{\boldsymbol{k}}\tau_{\boldsymbol{k}}S^{(0)}(\varepsilon) + \frac{q}{\hbar c}\tau_{\boldsymbol{k}}(\nabla_{\boldsymbol{k}}g_{\boldsymbol{k}}\times\boldsymbol{B})\cdot\boldsymbol{v}_{\boldsymbol{k}} \\ &\equiv \boldsymbol{v}_{\boldsymbol{k}}\cdot\boldsymbol{G}_{\boldsymbol{k}}, \end{aligned} \tag{5.10}$$

where $\boldsymbol{G}_{\boldsymbol{k}} = q\boldsymbol{E}\tau_{\boldsymbol{k}}S^{(0)}(\varepsilon) + \frac{q}{\hbar c}\tau_{\boldsymbol{k}}(\nabla_{\boldsymbol{k}}g_{\boldsymbol{k}}\times\boldsymbol{B})$. Then $\boldsymbol{G}_{\boldsymbol{k}}$ can be written as

$$\boldsymbol{G}_{\boldsymbol{k}} = \boldsymbol{G}_{\boldsymbol{k}}^{(0)} + \frac{\mu_0}{c}(\nabla_{\boldsymbol{v}}g_{\boldsymbol{k}}\times\boldsymbol{B}), \tag{5.11}$$

where $\boldsymbol{G}_{\boldsymbol{k}}^{(0)} = q\boldsymbol{E}\tau_{\boldsymbol{k}}S^{(0)}(\varepsilon)$, and $\mu_0 = \frac{q\tau_{\boldsymbol{k}}}{m}$ is the mobility of an electron gas system. Using an assumption that $\boldsymbol{G}_{\boldsymbol{k}}$ is independent of $\boldsymbol{v}_{\boldsymbol{k}}$, $\nabla_{\boldsymbol{v}}g_{\boldsymbol{k}} = \boldsymbol{G}_{\boldsymbol{k}}$. Then we have

$$\boldsymbol{G}_{\boldsymbol{k}} = \boldsymbol{G}_{\boldsymbol{k}}^{(0)} + \frac{\mu_0}{c}(\boldsymbol{G}_{\boldsymbol{k}}\times\boldsymbol{B}). \tag{5.12}$$

Taking the vector product of $\frac{\mu_0}{c}\boldsymbol{B}$ to each side of Eq. (5.12),

$$\begin{aligned} \frac{\mu_0}{c}\boldsymbol{G}_{\boldsymbol{k}}\times\boldsymbol{B} &= \frac{\mu_0}{c}\boldsymbol{G}_{\boldsymbol{k}}^{(0)}\times\boldsymbol{B} + \frac{\mu_0^2}{c^2}(\boldsymbol{G}_{\boldsymbol{k}}\times\boldsymbol{B})\times\boldsymbol{B} \\ &= \frac{\mu_0}{c}\boldsymbol{G}_{\boldsymbol{k}}^{(0)}\times\boldsymbol{B} + \frac{\mu_0^2}{c^2}\left(\boldsymbol{G}_{\boldsymbol{k}}\cdot\boldsymbol{B}\right)\boldsymbol{B} - \frac{\mu_0^2}{c^2}B^2\boldsymbol{G}_{\boldsymbol{k}}, \end{aligned} \tag{5.13}$$

and taking the inner product of $\frac{\mu_0}{c}\boldsymbol{B}$ to each side of Eq. (5.12),

$$\frac{\mu_0}{c}\boldsymbol{G}_{\boldsymbol{k}}\cdot\boldsymbol{B} = \frac{\mu_0}{c}\boldsymbol{G}_{\boldsymbol{k}}^{(0)}\cdot\boldsymbol{B} + \cancelto{0}{\frac{\mu_0^2}{c^2}(\boldsymbol{G}_{\boldsymbol{k}}\times\boldsymbol{B})\cdot\boldsymbol{B}}. \tag{5.14}$$

Then we can obtain a closed form of $\boldsymbol{G}_{\boldsymbol{k}}$ as [124]

$$\boldsymbol{G}_{\boldsymbol{k}} = \frac{\boldsymbol{G}_{\boldsymbol{k}}^{(0)} + \frac{\mu_0}{c}(\boldsymbol{G}_{\boldsymbol{k}}^{(0)}\times\boldsymbol{B}) + \frac{\mu_0^2}{c^2}(\boldsymbol{G}_{\boldsymbol{k}}^{(0)}\cdot\boldsymbol{B})\boldsymbol{B}}{1+\frac{\mu_0^2}{c^2}B^2}, \tag{5.15}$$

which, in turn, gives the expression for $g_{\boldsymbol{k}}$ as

$$\begin{aligned} g_{\boldsymbol{k}} &= \boldsymbol{v}_{\boldsymbol{k}}\cdot\boldsymbol{G}_{\boldsymbol{k}} \\ &= q\tau_{\boldsymbol{k}}S^{(0)}\boldsymbol{v}_{\boldsymbol{k}}\cdot\frac{\boldsymbol{E}+\frac{\mu_0}{c}(\boldsymbol{E}\times\boldsymbol{B}) + \frac{\mu_0^2}{c^2}(\boldsymbol{E}\cdot\boldsymbol{B})\boldsymbol{B}}{1+\frac{\mu_0^2}{c^2}B^2}. \end{aligned} \tag{5.16}$$

Putting $g_{\boldsymbol{k}}$ back in Eq. (5.9), we get

$$\begin{aligned}\frac{df}{dt} &= q\boldsymbol{E}\cdot\boldsymbol{v}_{\boldsymbol{k}}S^{(0)}(\varepsilon) + \frac{q}{\hbar c}\left(\nabla_{\boldsymbol{k}}g_{\boldsymbol{k}}\times\boldsymbol{B}\right)\cdot\boldsymbol{v}_{\boldsymbol{k}} \\ &= \boldsymbol{v}_{\boldsymbol{k}}\cdot\boldsymbol{G}_{\boldsymbol{k}},\end{aligned} \tag{5.17}$$

and finally, equating with the collision integral terms, we get

$$\begin{aligned}&\boldsymbol{v}_{\boldsymbol{k}}\cdot\boldsymbol{G}_{\boldsymbol{k}} \\ &= \int\frac{d^dk'}{(2\pi)^d}W_{\boldsymbol{k}'\boldsymbol{k}}\tau_{\boldsymbol{k}}\left(\boldsymbol{v}_{\boldsymbol{k}}\cdot\boldsymbol{G}-\boldsymbol{v}_{\boldsymbol{k}'}\cdot\boldsymbol{G}\right),\end{aligned} \tag{5.18}$$

where we have used $\nabla_{\boldsymbol{k}}g_{\boldsymbol{k}} = \frac{\hbar}{q}\mu_0\boldsymbol{G}$. If we assume that $\tau_{\boldsymbol{k}}$ in $\mu_0 = \frac{q\tau_{\boldsymbol{k}}}{m}$ is invariant under the electric field change, so that the equality Eq. (5.17) holds for all $\boldsymbol{G}$, we would get

$$\frac{1}{\tau_{\boldsymbol{k}}} = \int\frac{d^dk'}{(2\pi)^d}D_{\boldsymbol{k}'}W_{\boldsymbol{k}'\boldsymbol{k}}\left(1-\cos\theta\right), \tag{5.19}$$

where θ is an angle between $\boldsymbol{k}$ and $\boldsymbol{k}'$. Eq. (5.19) takes the exactly the same form as the nonmagnetic cases [40].

5.3 Magnetotransport equation in anisotropic systems with a nonvanishing Berry curvature

Up until this point, we have only considered the isotropic, single-band system without Berry curvature, namely an isotropic electron gas. Removing this restriction, we can account for the anisotropy from the electronic band structure, as well as the anisotropy that arises from the external magnetic field coupled with the Berry curvature of the system.

The semiclassical equation of motion for a Bloch electron in a system with nonvanishing Berry curvature is given by [129]

$$\dot{\boldsymbol{r}} = \boldsymbol{v}_{\boldsymbol{k}} - \dot{\boldsymbol{k}}\times\boldsymbol{\Omega}_{\boldsymbol{k}} \tag{5.20}$$

$$\hbar\dot{\boldsymbol{k}} = q\boldsymbol{E} + \frac{q}{c}\dot{\boldsymbol{r}}\times\boldsymbol{B}, \tag{5.21}$$

where $\boldsymbol{\Omega}_{\boldsymbol{k}}$ is the Berry curvature. Solving the recursive equation, we get

$$D_{\boldsymbol{k}}\dot{\boldsymbol{r}} = \boldsymbol{v}_{\boldsymbol{k}} - \frac{q}{\hbar}\boldsymbol{E}\times\boldsymbol{\Omega}_{\boldsymbol{k}} - \frac{q}{\hbar c}(\boldsymbol{v}_{\boldsymbol{k}}\cdot\boldsymbol{\Omega}_{\boldsymbol{k}})\boldsymbol{B} \tag{5.22}$$

$$\hbar D_{\boldsymbol{k}}\dot{\boldsymbol{k}} = q\boldsymbol{E} + \frac{q}{c}\boldsymbol{v}_{\boldsymbol{k}}\times\boldsymbol{B} - \frac{q^2}{\hbar c}(\boldsymbol{E}\cdot\boldsymbol{B})\boldsymbol{\Omega}_{\boldsymbol{k}}, \tag{5.23}$$

where $D_{\boldsymbol{k}} = 1 - \frac{q}{\hbar c}(\boldsymbol{\Omega}_{\boldsymbol{k}}\cdot\boldsymbol{B})$. The magnetic field and the Berry curvature also modifies the density of states, and the volume element $\Delta V_0 \to \Delta V_0/D_{\boldsymbol{k}}$ [109–111]. Therefore, any integral over a Brillouin zone must get an additional $D_{\boldsymbol{k}}$ to account for this change.

Writing the equation of motion of an arbitrary system with Eq. (5.23), we get

$$\begin{aligned}
\frac{df}{dt} &= -\hbar\dot{\boldsymbol{k}}\cdot\boldsymbol{v}_{\boldsymbol{k}}S^{(0)}(\varepsilon) + \dot{\boldsymbol{k}}\cdot\nabla_{\boldsymbol{k}}g_{\boldsymbol{k}} \\
&= -\frac{1}{D_{\boldsymbol{k}}}\left[q\boldsymbol{E} + \cancelto{0}{\frac{q}{c}\boldsymbol{v}_{\boldsymbol{k}}\times\boldsymbol{B}} - \frac{q^2}{\hbar c}(\boldsymbol{E}\cdot\boldsymbol{B})\boldsymbol{\Omega}_{\boldsymbol{k}}\right]\cdot\boldsymbol{v}_{\boldsymbol{k}}S^{(0)}(\varepsilon) \\
&+\frac{1}{D_{\boldsymbol{k}}}\frac{q}{\hbar c}(\boldsymbol{v}_{\boldsymbol{k}}\times\boldsymbol{B})\cdot\nabla_{\boldsymbol{k}}g_{\boldsymbol{k}} \\
&= -q\boldsymbol{E}\cdot\boldsymbol{v}_{\boldsymbol{k}}^{\mathrm{mod}}S^{(0)}(\varepsilon) + \frac{q}{\hbar c}\frac{(\boldsymbol{v}_{\boldsymbol{k}}\times\boldsymbol{B})\cdot\nabla_{\boldsymbol{k}}g_{\boldsymbol{k}}}{D_{\boldsymbol{k}}} \\
&= -q\boldsymbol{E}\cdot\boldsymbol{v}_{\boldsymbol{k}}^{\mathrm{mod}}S^{(0)}(\varepsilon) + \frac{q}{\hbar c}(\boldsymbol{v}_{\boldsymbol{k}}^{\mathrm{mod}}\times\boldsymbol{B})\cdot\nabla_{\boldsymbol{k}}g_{\boldsymbol{k}},
\end{aligned} \tag{5.24}$$

where $\boldsymbol{v}_{\boldsymbol{k}}^{\mathrm{mod}} \equiv \left[\boldsymbol{v}_{\boldsymbol{k}} - \frac{q}{\hbar c}(\boldsymbol{\Omega}_{\boldsymbol{k}}\cdot\boldsymbol{v}_{\boldsymbol{k}})\boldsymbol{B}\right]/D_{\boldsymbol{k}}$ is the modified velocity. Then the Boltzmann equation becomes

$$\begin{aligned}
&q\boldsymbol{E}\cdot\boldsymbol{v}_{\boldsymbol{k}}^{\mathrm{mod}}S^{(0)}(\varepsilon) - \frac{q}{\hbar c}(\boldsymbol{v}_{\boldsymbol{k}}^{\mathrm{mod}}\times\boldsymbol{B})\cdot\nabla_{\boldsymbol{k}}g_{\boldsymbol{k}} \\
&= \int\frac{d^dk'}{(2\pi)^d}D_{\boldsymbol{k}'}W_{\boldsymbol{k}'\boldsymbol{k}}\left(g_{\boldsymbol{k}} - g_{\boldsymbol{k}'}\right),
\end{aligned} \tag{5.25}$$

which takes a similar form as the Eq. (5.9), but the velocity $\boldsymbol{v}_{\boldsymbol{k}}$ was swapped out for the modified velocity $\boldsymbol{v}_{\boldsymbol{k}}^{\mathrm{mod}}$, and the collision integral got an additional $D_{\boldsymbol{k}'}$ from the modified volume element.

Similar to Eq. (5.10) in the previous section, we introduce an ansatz for the $g_{\boldsymbol{k}}$ that extends upon the Eq. (5.10). The modified ansatz for the $g_{\boldsymbol{k}}$ is given by

$$\begin{aligned} g_{\boldsymbol{k}} &= q\left(\sum_{i=1}^{d} E^{(i)} v_{\boldsymbol{k}}^{\mathrm{mod}(i)} \tau_{\boldsymbol{k}}^{(i)}\right) S^{(0)}(\varepsilon) \\ &+ \frac{q}{\hbar c}\sum_{i,j,k}^{d} \epsilon_{ijk}\tau_{\boldsymbol{k}}^{(i)} v_{\boldsymbol{k}}^{\mathrm{mod}(i)} \frac{\partial g_{\boldsymbol{k}}}{\partial k^{(j)}} B^{(k)} \\ &\equiv \sum_{i=1}^{d} v_{\boldsymbol{k}}^{\mathrm{mod}(i)} \tau_{\boldsymbol{k}}^{(i)} G^{(i)}, \end{aligned} \tag{5.26}$$

where ϵ_{ijk} is a Levi-Civita symbol, $\tau_{\boldsymbol{k}}^{(i)}$ is the relaxation time, and

$$G^{(i)} = qE^{(i)}S^{(0)} + \frac{q}{\hbar c}\sum_{j,k}^{d} \epsilon_{ijk}\frac{\partial g_{\boldsymbol{k}}}{\partial k^{(j)}} B^{(k)}. \tag{5.27}$$

Introducing inverse mass tensor $\tilde{\mathbb{M}}$ [130], where

$$\tilde{\mathbb{M}}_{ij} = \frac{1}{\hbar}\frac{\partial v_{\boldsymbol{k}}^{\mathrm{mod}(j)}}{\partial k_i}, \tag{5.28}$$

then Eq. (5.27) becomes

$$G^{(i)} = G_0^{(i)} + \frac{q}{c}\sum_{j,k}^{d} \epsilon_{ijk}\tilde{\mathbb{M}}_{jl}\frac{\partial g_{\boldsymbol{k}}}{\partial v_{\boldsymbol{k}}^{\mathrm{mod}(l)}} B^{(k)}, \tag{5.29}$$

where $G_0^{(i)} \equiv qE^{(i)}S^{(0)}$. Introducing the relaxation time tensor $\mathbb{T}$, where

$$\mathbb{T} = \begin{pmatrix} \tau_{\boldsymbol{k}}^{x} & 0 & 0 \\ 0 & \tau_{\boldsymbol{k}}^{y} & 0 \\ 0 & 0 & \tau_{\boldsymbol{k}}^{z} \end{pmatrix}, \tag{5.30}$$

and the field strength tensor $\mathbb{F}$ (whose action onto a vector is equivalent to taking a cross product, i.e. $\boldsymbol{a} \times \boldsymbol{B} = \mathbb{F}\boldsymbol{a}$, $\boldsymbol{a}$ is an arbitrary three-dimensional vector),

$$\mathbb{F} = \epsilon_{ijk}B^{(k)} = \begin{pmatrix} 0 & B^{z} & -B^{y} \\ -B^{z} & 0 & B^{x} \\ B^{y} & -B^{x} & 0 \end{pmatrix}, \tag{5.31}$$

then Eq. (5.27) can be further simplified as

$$G^{(i)} = G_0^{(i)} + \frac{q}{c}\left[\mathbb{F}\tilde{\mathbb{M}}\frac{\partial g_{\boldsymbol{k}}}{\partial \boldsymbol{v}_{\boldsymbol{k}}^{\rm mod}}\right]_i = G_0^{(i)} + \left[\mathbb{F}\frac{\boldsymbol{\mu}}{c}\boldsymbol{G}\right]_i, \tag{5.32}$$

where $\boldsymbol{\mu}_{ij} = q\sum_{l=1}^{d}\tilde{\mathbb{M}}_{il}\mathbb{T}_{lj}$ is the mobility tensor. Here, we have assumed that $\boldsymbol{G}$ is independent of $\boldsymbol{v}_{\boldsymbol{k}}^{\rm mod}$ which holds for low magnetic field, i.e. $\frac{\partial g_{\boldsymbol{k}}}{\partial \boldsymbol{v}_{\boldsymbol{k}}^{\rm mod}} = \sum_{i=1}^{d}\tau_{\boldsymbol{k}}^{(i)}G^{(i)}$ (from Eq. (5.26)). Then Eq. (5.32) becomes

$$\begin{aligned}\boldsymbol{G} &= \boldsymbol{G}_0 + \mathbb{F}\frac{\boldsymbol{\mu}}{c}\boldsymbol{G} \\ &= \left(\mathbb{1} - \mathbb{F}\frac{\boldsymbol{\mu}}{c}\right)^{-1}\boldsymbol{G}_0 \equiv \mathbb{N}\boldsymbol{G}_0,\end{aligned} \tag{5.33}$$

where $\mathbb{1}$ is a 3×3 identity matrix, and $\mathbb{N} = \left(\mathbb{1} - \mathbb{F}\frac{\boldsymbol{\mu}}{c}\right)^{-1}$. Now we can express $g_{\boldsymbol{k}}$ as

$$g_{\boldsymbol{k}} = \sum_{i=1}^{d} v_{\boldsymbol{k}}^{{\rm mod}(i)}\tau_{\boldsymbol{k}}^{(i)}G^{(i)} = \sum_{i,j=1}^{d} v_{\boldsymbol{k}}^{{\rm mod}(i)}\tau_{\boldsymbol{k}}^{(i)}\mathbb{N}_{ij}G_0^{(j)}. \tag{5.34}$$

We now re-arrange the equation of motion $\dot{\boldsymbol{k}}\cdot\nabla_{\boldsymbol{k}}f$ with the quantities defined above. Using $\nabla_{\boldsymbol{k}}g_{\boldsymbol{k}} = \frac{\hbar}{q}\boldsymbol{\mu}\boldsymbol{G}$, we would get

$$\begin{aligned}\frac{df}{dt} &= q\boldsymbol{E}\cdot\boldsymbol{v}_{\boldsymbol{k}}^{\rm mod}S^{(0)}(\varepsilon) + \frac{q}{c}\left(\tilde{\mathbb{M}}\mathbb{T}\boldsymbol{G}\times\boldsymbol{B}\right)\cdot\boldsymbol{v}_{\boldsymbol{k}}^{\rm mod} \\ &= \left[qS^{(0)}(\varepsilon)\boldsymbol{E} + \mathbb{F}\frac{\boldsymbol{\mu}}{c}\boldsymbol{G}\right]\cdot\boldsymbol{v}_{\boldsymbol{k}}^{\rm mod} \\ &= \boldsymbol{v}_{\boldsymbol{k}}^{\rm mod}\cdot\boldsymbol{G}.\end{aligned} \tag{5.35}$$

Putting $g_{\boldsymbol{k}}$ back to the collision integral equation, we now write down the Boltzmann equation as

$$\begin{aligned}\frac{df}{dt} &= \sum_{i=1}^{d} v_{\boldsymbol{k}}^{{\rm mod}(i)}G^{(i)} \\ &= \sum_{i=1}^{d}\int\frac{d^dk'}{(2\pi)^d}D_{\boldsymbol{k}'}W_{\boldsymbol{k}'\boldsymbol{k}}\left(v_{\boldsymbol{k}}^{{\rm mod}(i)}\tau_{\boldsymbol{k}}^{(i)}G^{(i)} - v_{\boldsymbol{k}'}^{{\rm mod}(i)}\tau_{\boldsymbol{k}'}^{(i)}G^{(i)}\right),\end{aligned} \tag{5.36}$$

where we have assumed that $\boldsymbol{G}$ only depends on $\boldsymbol{k}$ through $\varepsilon(\boldsymbol{k})$ for the elastic scattering, which gives $\boldsymbol{G} = \boldsymbol{G}'$. Using that $\boldsymbol{G} = \mathbb{N}\boldsymbol{G}_0 = qS^{(0)}\mathbb{N}\boldsymbol{E}$, we can group Eq. (5.35) into the linear equation for $\boldsymbol{G}$.

$$\left[\int \frac{d^d k'}{(2\pi)^d} D_{\boldsymbol{k}'} W_{\boldsymbol{k}'\boldsymbol{k}} \left(\boldsymbol{v}_{\boldsymbol{k}}^{\mathrm{mod}}\mathbb{T} - \boldsymbol{v}_{\boldsymbol{k}'}^{\mathrm{mod}}\mathbb{T}'\right) - \boldsymbol{v}_{\boldsymbol{k}}^{\mathrm{mod}}\right] \cdot \boldsymbol{G} = 0 \tag{5.37}$$

and as Eq. (5.37) must hold for all $\boldsymbol{E}$, the terms inside the bracket must be zero. Then we obtain

$$\int \frac{d^d k'}{(2\pi)^d} D_{\boldsymbol{k}'} W_{\boldsymbol{k}'\boldsymbol{k}} \left(\boldsymbol{v}_{\boldsymbol{k}}^{\mathrm{mod}}\mathbb{T} - \boldsymbol{v}_{\boldsymbol{k}'}^{\mathrm{mod}}\mathbb{T}'\right) = \boldsymbol{v}_{\boldsymbol{k}}^{\mathrm{mod}}, \tag{5.38}$$

or alternatively,

$$\int \frac{d^d k'}{(2\pi)^d} D_{\boldsymbol{k}'} W_{\boldsymbol{k}'\boldsymbol{k}} \left(\tau_{\boldsymbol{k}}^{(i)} - \frac{v_{\boldsymbol{k}'}^{\mathrm{mod}(i)}}{v_{\boldsymbol{k}}^{\mathrm{mod}(i)}} \tau_{\boldsymbol{k}'}^{(i)}\right) = 1, \tag{5.39}$$

which is a coupled integral equation for $\tau_{\boldsymbol{k}}^{(i)}$.

Notice that Eq. (5.39) has exactly the same form as the nonmagnetic anisotropic relaxation time equation [70, 131], except the velocity gets modified, i.e. $v_{\boldsymbol{k}}^{(i)} \to v_{\boldsymbol{k}}^{\mathrm{mod}(i)}$ and the integral gets an extra $D_{\boldsymbol{k}}$ term.

5.4 Magnetoconductivity

The current density $\boldsymbol{J}$ is given by

$$\begin{aligned}
\boldsymbol{J} &= gq \int \frac{d^d \boldsymbol{k}}{(2\pi)^d} D_{\boldsymbol{k}} \dot{\boldsymbol{r}} f_{\boldsymbol{k}} \\
&= gq \int \frac{d^d \boldsymbol{k}}{(2\pi)^d} \left[\boldsymbol{v}_{\boldsymbol{k}} - \frac{q}{\hbar}\boldsymbol{E} \times \boldsymbol{\Omega}_{\boldsymbol{k}} - \frac{q}{\hbar c}(\boldsymbol{v}_{\boldsymbol{k}} \cdot \boldsymbol{\Omega}_{\boldsymbol{k}})\boldsymbol{B}\right] \\
&\times \left(f_{\boldsymbol{k}}^{(0)} + g_{\boldsymbol{k}}\right).
\end{aligned} \tag{5.40}$$

where g is the spin degeneracy factor. Working out each term, we get (note that $\boldsymbol{v}_{\boldsymbol{k}} f_{\boldsymbol{k}}^{(0)}$ vanishes after the integral)

$$\boldsymbol{J} = \boldsymbol{J}^{\mathrm{IAHE}} + \boldsymbol{J}^{\mathrm{AHE}} + \boldsymbol{J}^{\mathrm{CME}} + \boldsymbol{J}^{\mathrm{ext}}, \tag{5.41}$$

where

$$\boldsymbol{J}^{\mathrm{IAHE}} = -\frac{gq^2}{\hbar}\int \frac{d^d\boldsymbol{k}}{(2\pi)^d}\boldsymbol{E}\times\boldsymbol{\Omega}_{\boldsymbol{k}} f_{\boldsymbol{k}}^{(0)}, \tag{5.42}$$

is the intrinsic anomalous Hall effect (AHE) term,

$$\boldsymbol{J}^{\mathrm{AHE}} = -\frac{gq^2}{\hbar}\int \frac{d^d\boldsymbol{k}}{(2\pi)^d}\boldsymbol{E}\times\boldsymbol{\Omega}_{\boldsymbol{k}} g_{\boldsymbol{k}}, \tag{5.43}$$

is the AHE term,

$$\boldsymbol{J}^{\mathrm{CME}} = -\frac{gq^2}{\hbar c}\int \frac{d^d\boldsymbol{k}}{(2\pi)^d}(\boldsymbol{v}_{\boldsymbol{k}}\cdot\boldsymbol{\Omega}_{\boldsymbol{k}})\boldsymbol{B} f_{\boldsymbol{k}}^{(0)}, \tag{5.44}$$

is the intrinsic CME current term, and

$$\boldsymbol{J}^{\mathrm{ext}} = gq\int \frac{d^d\boldsymbol{k}}{(2\pi)^d} D_{\boldsymbol{k}}\boldsymbol{v}_{\boldsymbol{k}}^{\mathrm{mod}} g_{\boldsymbol{k}}, \tag{5.45}$$

is the extrinsic current term. Ignoring the intrinsic terms and the higher-order terms, we are only left with the $\boldsymbol{J}^{\mathrm{ext}}$. Writing down the Ohm's law, we get

$$J_i^{\mathrm{ext}} = \sigma_{ij}^{\mathrm{ext}} E_j = gq\int \frac{d^d\boldsymbol{k}}{(2\pi)^d} v_{\boldsymbol{k}}^{\mathrm{mod}(i)} g_{\boldsymbol{k}}, \tag{5.46}$$

where $\sigma_{ij}^{\mathrm{ext}}$ is the conductivity tensor as a response to the extrinsic field.

If we were to consider the isotropic system with magnetic field, then $g_{\boldsymbol{k}}$ will be given by Eq. (5.16). By matching coefficients of $\boldsymbol{E}$, we get

$$\begin{aligned}\sigma_{ij}^{\mathrm{ext}} &= gq^2\int \frac{d^d\boldsymbol{k}}{(2\pi)^d}\frac{D_{\boldsymbol{k}} S^{(0)}\tau_{\boldsymbol{k}} v_{\boldsymbol{k}}^{\mathrm{mod}(i)}}{1+\frac{\mu^2}{c^2}B^2} \\ &\times\left[v_{\boldsymbol{k}}^{\mathrm{mod}(j)} - \frac{\mu}{c}(\boldsymbol{v}_{\boldsymbol{k}}^{\mathrm{mod}}\times\boldsymbol{B})_{(j)} + \frac{\mu^2}{c^2}(\boldsymbol{v}_{\boldsymbol{k}}^{\mathrm{mod}}\cdot\boldsymbol{B})B^{(j)}\right].\end{aligned} \tag{5.47}$$

If we consider the anisotropic system with magnetic field, then $g_{\boldsymbol{k}}$ will be given by Eq. (5.34). Again, by matching coefficients of $\boldsymbol{E}$ for each row of $\boldsymbol{\sigma}^{\mathrm{ext}}\cdot\boldsymbol{E}$, we get

$$\begin{aligned}\sigma_{ij}^{\mathrm{ext}} &= gq^2\int \frac{d^d\boldsymbol{k}}{(2\pi)^d} D_{\boldsymbol{k}} S^{(0)} v_{\boldsymbol{k}}^{\mathrm{mod}(i)} (\boldsymbol{v}_{\boldsymbol{k}}^{\mathrm{mod}}\mathbb{T}\mathbb{N})_{(j)} \\ &= gq^2\sum_{l=1}^{d}\int \frac{d^d\boldsymbol{k}}{(2\pi)^d} D_{\boldsymbol{k}} S^{(0)} v_{\boldsymbol{k}}^{\mathrm{mod}(i)} \mathbb{N}_{lj}\tau_{\boldsymbol{k}}^{(l)} v_{\boldsymbol{k}}^{\mathrm{mod}(l)}.\end{aligned} \tag{5.48}$$

For anisotropic, multi-band systems, Eq. (5.48) would become

$$\sigma_{ij}^{\text{ext}} = gq^2 \sum_{\alpha} \int \frac{d^d\boldsymbol{k}}{(2\pi)^d} D_{\boldsymbol{k}\alpha} S^{(0)} v_{\boldsymbol{k}\alpha}^{\text{mod}(i)} (\boldsymbol{v}_{\boldsymbol{k}\alpha}^{\text{mod}} \mathbb{T}\mathbb{N})_{(j)} \tag{5.49}$$

$$= gq^2 \sum_{\alpha} \sum_{l=1}^{d} \int \frac{d^d\boldsymbol{k}}{(2\pi)^d} D_{\boldsymbol{k}\alpha} S^{(0)} v_{\boldsymbol{k}\alpha}^{\text{mod}(i)} \mathbb{N}_{lj} \tau_{\boldsymbol{k}\alpha}^{(l)} v_{\boldsymbol{k}\alpha}^{\text{mod}(l)}.$$

If we consider the system without the magnetic field, $\mathbb{N} = \mathbb{1}$, $\boldsymbol{v}_{\boldsymbol{k}}^{\text{mod}} = \boldsymbol{v}_{\boldsymbol{k}}$, and $D_{\boldsymbol{k}} = 1$.

$$\sigma_{ij}^{\text{ext}} = gq^2 \int \frac{d^d\boldsymbol{k}}{(2\pi)^d} S^{(0)} v_{\boldsymbol{k}}^{(i)} v_{\boldsymbol{k}}^{(j)} \tau_{\boldsymbol{k}}^{(j)}, \tag{5.50}$$

or for multi-band systems,

$$\sigma_{ij}^{\text{ext}} = gq^2 \sum_{\alpha} \int \frac{d^d\boldsymbol{k}}{(2\pi)^d} S^{(0)} v_{\boldsymbol{k}\alpha}^{(i)} v_{\boldsymbol{k}\alpha}^{(j)} \tau_{\boldsymbol{k}\alpha}^{(j)}, \tag{5.51}$$

which are anisotropic, or anisotropic multi-band conductivity equation that are consistent with the nonmagnetic cases [70, 131].

5.5 Discussion

We derive the semiclassical magnetotransport equations, as well as the relaxation time equation, with the least possible amount of assumptions imposed to obtain the compact closed form of the nonequilibrium distribution function. We calculated the field-dependent, anisotropic relaxation time $\tau_{\boldsymbol{k}}^{(i)}$ as a solution to the nonequilibrium distribution function $f_{\boldsymbol{k}} = f_{\boldsymbol{k}}^{(0)} + g_{\boldsymbol{k}}$, and studied how the impurity scattering and the magnetic field affect the transport behavior.

We developed the extended Boltzmann transport theory that can not only be applied when the system is inherently anisotropic, i.e. the band dispersion is anisotropic, but can also be utilized when the system is made to be anisotropic with its Berry curvature and the magnetic field coupling. Even when the band dispersion of the system is isotropic, we suggest that the magnetic field and

the Berry curvature makes the distribution of the electrons anisotropic so that their movement can no longer be described in an isotropic formalism, as the band velocity $\boldsymbol{v}_{\boldsymbol{k}}$ gets the additional magnetic field-originate terms when there is a nonvanishing Berry curvature present. Using our formalism, any anisotropy of the system can be properly assessed regardless of its origin.

For the scattering mechanisms, we only considered the elastic scattering sources that conserve energy. When the scattering becomes inelastic, e.g. electron-phonon scattering, it can be shown that the modified detailed balance equation $W_{\boldsymbol{k}\boldsymbol{k}'} f^{(0)}_{\boldsymbol{k}'}(1 - f^{(0)}_{\boldsymbol{k}}) = W_{\boldsymbol{k}'\boldsymbol{k}} f^{(0)}_{\boldsymbol{k}}(1 - f^{(0)}_{\boldsymbol{k}'})$ [132, 133] would apply and the final expression of $\tau^{(i)}_{\boldsymbol{k}}$ would become

$$\int \frac{d^d k'}{(2\pi)^d} D_{\boldsymbol{k}'} W_{\boldsymbol{k}'\boldsymbol{k}} \left(\tau^{(i)}_{\boldsymbol{k}} - \frac{v^{\mathrm{mod}(i)}_{\boldsymbol{k}'}}{v^{\mathrm{mod}(i)}_{\boldsymbol{k}}} \tau^{(i)}_{\boldsymbol{k}'} \right) \left(\frac{1 - f^{(0)}_{\boldsymbol{k}'}}{1 - f^{(0)}_{\boldsymbol{k}}} \right) = 1. \tag{5.52}$$

Chapter 6

Diluted magnetic Dirac-Weyl materials: Susceptibility and ferromagnetism in three-dimensional chiral gapless semimetals

6.1 Introduction

In recent years, there has been substantial interest in three-dimensional (3D) Weyl/Dirac semimetals, which have relativistic linear energy dispersion [4, 23, 24, 107, 134–136]. These systems are effectively 3D versions of graphene which is the quintessential 2D Dirac system. The magnetic properties of Dirac-Weyl semimetals have been studied theoretically, demonstrating the possibility of magnetic ordering of the dopant magnetic impurities at zero temperature with and without spin-orbit coupling [137–139]. Mechanisms for various magnetic ordering in topological materials have been investigated, demonstrating that magnetically doped semiconductors with the strong spin-orbit interaction can

have ferromagnetic ordering through the mechanism of van Vleck paramagnetism [140, 141]. The spin susceptibilities in Weyl and Dirac semimetals have been calculated, investigating the effect of the magnetic texture and associated physical properties [142–145].

The indirect exchange interactions between magnetic impurities through carriers of a host material (i.e., Ruderman-Kittel-Kasuya-Yosida (RKKY) interaction [146–149]) in semimetal systems has become an interesting issue. Since the low energy dispersion in condensed matter systems can be nonlinear as in 2D multilayer graphene [150, 151] and 3D multi-Weyl semimetals [6], it is also interesting to find the effects of arbitrary band dispersion and finite temperature on the magnetic properties of 3D gapless systems in the presence of random magnetic impurities (i.e. in addition to the expected linear gapless chiral dispersion of Dirac systems). Moreover, the nonlinear energy dispersions of itinerant carriers result in an interesting behavior of the RKKY interaction between magnetic spins, which provides a more complete picture of the qualitative nature of magnetic properties in gapless semimetals with arbitrary band dispersion. In particular, it is useful to know whether 3D Dirac-Weyl gapless semimetals could magnetically order at finite temperatures through the RKKY coupling, and how the resultant magnetic transition temperature depends on the band carrier energy dispersion.

In this chapter, we study the magnetic properties of 3D gapless electron-hole systems at finite temperatures with arbitrary band dispersion, focusing on the possibility of long-range ordering in the magnetic moments that are embedded in the system. To study the carrier-mediated indirect RKKY exchange interaction among the random magnetic impurities with the itinerant carriers mediating the magnetic interaction between the impurities, we calculate the temperature-dependent response functions and the corresponding long-range

magnetic coupling between dilute random magnetic impurities. We mainly focus on the dilute impurity limit, which is different from the strong disorder limit in which strong enough disorder may induce a phase transition to a metallic state [27, 152–154]. The effects of finite temperature, disorder, and carrier mean-free path on the RKKY interaction are also considered systematically in our current work, but we do not consider the topic of disorder-induced quantum phase transition since our focus is on magnetic properties and not disorder physics. Especially, we study the role of the ultraviolet momentum cutoff, which is necessary in gapless semimetals, demonstrating that it fundamentally modifies the characteristic power-law behavior of the RKKY interaction. Inclusion of the mean-free path in the theory allows us to make a specific prediction about the dependence of the magnetic behavior of the system on the carrier transport properties [155]. A smooth interpolation between long-range and short-range magnetic interactions is possible by varying the cutoff parameter R in the range of the RKKY interaction, which is related to the localization length of the carriers in semimetals [156–158].

By considering all these effects together within one comprehensive mean-field theory, we calculate the ferromagnetic transition temperature in the framework of a finite-temperature self-consistent field approximation [156] for the ferromagnetism in 3D gapless semimetals. We find that in 3D gapless semimetals, the ferromagnetic ordering between magnetic impurities induced by the RKKY exchange interaction is favored with enhanced magnetic coupling, as the energy dispersion has a higher power-law. Our results indicate that within the experimentally accessible range of parameters, ferromagnetic ordering between magnetic impurities is possible in gapless 3D semimetals. Ferromagnetism in 3D semimetals, as predicted in our theory, can be utilized in spintronics applications if our predictions are validated experimentally. We predict that it

should be possible to experimentally induce long-range finite-temperature ferromagnetic ordering in 3D Dirac-Weyl materials by magnetically doping the system.

This chapter is organized as follows. In Sec. 6.2, we describe our model and calculate the finite-temperature static susceptibilities. In Sec. 6.3, we provide the calculated results of the effective magnetic coupling through RKKY interaction in 3D chiral gapless semimetals. The conclusions are provided in Sec. 6.4 with a discussion on the momentum-cutoff effect on long-range oscillations.

6.2 Model

To describe the 3D chiral gapless semimetals, including Weyl/Dirac semimetals, we introduce the following Hamiltonian with an isotropic energy dispersion characterized by a positive integer N [37]:

$$H = \varepsilon_0 \left(\frac{|\boldsymbol{k}|}{k_0} \right)^N \hat{\boldsymbol{k}} \cdot \boldsymbol{\sigma}, \tag{6.1}$$

where $\boldsymbol{\sigma}$ represents the Pauli matrices acting in the space of the two bands near the band touching point, and ε_0 and k_0 are materials dependent constants with dimensions of energy and wave vector, respectively. We note that the introduced Hamiltonian describes a gapless electron-hole system with arbitrary energy-band dispersion. Even though the real systems with the Hamiltonian except a linear dispersion ($N = 1$) may not be available currently in 3D, it is interesting to obtain the magnetic properties for both linear and nonlinear energy dispersions to develop intuition about the dispersion dependence of RKKY interactions. Also, rapid development in the materials science may lead to such materials with nonlinear dispersion in the future, making our theory for the nonlinear dispersion of experimental relevance. Here, for simplicity, we assume that the Pauli matrices describe the pseudospin degrees of freedom rather than

real spin degrees of freedom, focusing on the effect of the arbitrary energy dispersion. We will discuss the effect of the real spin texture in the Discussion and Conclusion section. The energy dispersion of the Hamiltonian is given by $\varepsilon_{\lambda,\boldsymbol{k}} = \lambda\varepsilon_0 \left(\frac{|\boldsymbol{k}|}{k_0}\right)^N$, where $\lambda = \pm 1$ is the band index for the conduction (valence) band. Note that the Hamiltonian with $N = 1$ corresponds to Weyl semimetals with linear energy dispersion. We assume that the system is intrinsic with the Fermi energy at the band touching point, which we take to be the zero of energy. We are thus considering undoped intrinsic Dirac-Weyl systems with the chemical potential pinned at the Dirac-Weyl point.

Carrier-mediated RKKY indirect exchange interaction between local moments is proportional to the static carrier susceptibility. At finite temperatures, the static susceptibility is given by

$$\chi(\boldsymbol{q}, T) = -g \sum_{\lambda,\lambda'} \int \frac{d^3\boldsymbol{k}}{(2\pi)^3} \frac{f_{\lambda,\boldsymbol{k}} - f_{\lambda',\boldsymbol{k}'}}{\varepsilon_{\lambda,\boldsymbol{k}} - \varepsilon_{\lambda',\boldsymbol{k}'}} F_{\lambda,\lambda'}(\boldsymbol{k}, \boldsymbol{k}'), \tag{6.2}$$

where g is the total (e.g., spin, valley, etc.) degeneracy factor, $f_{\lambda,\boldsymbol{k}} = \left[e^{\varepsilon_{\lambda,\boldsymbol{k}}/k_{\mathrm{B}}T} + 1\right]^{-1}$ is the finite-temperature Fermi-Dirac distribution function for the λ-band and wave vector $\boldsymbol{k}$, the chiral factor $F_{\lambda,\lambda'}(\boldsymbol{k}, \boldsymbol{k}')$ is the square of the wavefunction overlap between $|\lambda, \boldsymbol{k}\rangle$ and $|\lambda', \boldsymbol{k}'\rangle$ states, and $\boldsymbol{k}' = \boldsymbol{k} + \boldsymbol{q}$. For the 3D chiral gapless system described by Eq. (6.1), $F_{\lambda,\lambda'}(\boldsymbol{k}, \boldsymbol{k}') = \frac{1}{2}\left(1 + \lambda\lambda' \cos\theta_{\boldsymbol{k},\boldsymbol{k}'}\right)$ for all N, where $\theta_{\boldsymbol{k},\boldsymbol{k}'}$ is the angle between $\boldsymbol{k}$ and $\boldsymbol{k}'$. Note that F arises entirely from the chirality of the system.

Dividing the sum in Eq. (6.2) into interband ($\lambda \neq \lambda'$) and intraband ($\lambda = \lambda'$) contributions, the static susceptibility can be decomposed into $\chi(\boldsymbol{q}, T) = \chi^+(\boldsymbol{q}, T) + \chi^-(\boldsymbol{q}, T)$, where $\chi^\pm$ denote the interband (+) and intraband (−) contributions, respectively. With the density of states (DOS) at $T = 0$, $D_N(q) =$

$\frac{gq^{3-N}k_0^N}{2\pi^2 N\varepsilon_0}$, the normalized susceptibility $\chi^{\pm}$ can be rewritten as

$$\begin{aligned}\frac{\chi^{\pm}(\boldsymbol{q},T)}{D_N(q)} &= \frac{N}{4}\int_0^{\infty} x^2 dx \int_0^{\pi} \sin\theta d\theta \frac{(1\mp\cos\psi)}{x^N \pm (x')^N} \\ &\times \left[\tanh\frac{(qx/k_0)^N}{2T/T_0} \pm \tanh\frac{(qx'/k_0)^N}{2T/T_0}\right], \end{aligned} \tag{6.3}$$

where θ is the angle between $\boldsymbol{k}$ and $\boldsymbol{q}$, and ψ is the angle between $\boldsymbol{k}$ and $\boldsymbol{k'} = \boldsymbol{k}+\boldsymbol{q}$. In Eq. (6.3), $x = k/q$, $x' = k'/q = \sqrt{1+2x\cos\theta+x^2}$, $\cos\psi = (x+\cos\theta)/x'$, and $T_0 = \varepsilon_0/k_{\mathrm{B}}$. Note that for $N = 1$, a finite (ultraviolet) momentum cutoff is required for the convergence of the integral. For the calculation, we set $g = 4$ and $k_0 = a^{-1}$, where a is the lattice constant of the system.

At zero temperature ($T = 0$), due to the phase-space restriction, the intraband part χ^- vanishes and only the interband part χ^+ contributes to the total susceptibility. In the long wavelength limit ($q \to 0$), the susceptibility approaches the DOS and $\chi^+(q, T = 0) \propto q^{3-N}$, which diverges for $N \geq 4$ as $q \to 0$. At finite temperatures ($T \neq 0$), we obtain $\chi^+(q,T) \propto q^3/T$ for $q \to 0$. Thus, the $q = 0$ singularity of $\chi^+(q, T = 0)$ for $N \geq 4$ disappears. In addition, due to the thermal excitation of electrons and holes, χ^- also contributes to the susceptibility at finite temperatures even for the undoped system under consideration. Thus, for $T \neq 0$, the total susceptibility at $q = 0$ becomes finite for all N. Specifically, we find that $\chi^-(q \to 0, T) \propto T^{\frac{3-N}{N}}$, which shows the same power-law dependence as the DOS, $D_N(\varepsilon) \propto \varepsilon^{\frac{3-N}{N}}$ with energy ε replaced by T. Therefore, as temperature increases, the total susceptibility at $q = 0$ increases for $N = 1, 2$, remains constant for $N = 3$, and decreases for $N \geq 4$. These analytical findings are helpful in understanding our detailed numerical results presented in the rest of this chapter.

Figure 6.1 shows the calculated static susceptibility as a function of the wave vector for several temperatures. For $N = 1, 2$, the susceptibility increases with temperature, whereas for $N \geq 4$, it decreases with temperature, as expected.

Interestingly, for $N \geq 3$, the finite-temperature result in the $T \to 0$ limit is different from the zero-temperature value, i.e., $\chi(0, T = 0) \neq \chi(0, T \to 0)$. Note that for $N = 3$, the DOS $D_N(q)$ becomes constant and $\chi(0, T \to 0)$ approaches the constant DOS, whereas $\chi(0, T = 0)$ can be obtained from Eq. (6.3). For $N = 3$, we find that $\chi(0, T = 0)/\chi(0, T \to 0) \approx 0.8229$. This $T = 0$ non-analyticity in the $N = 3$ susceptibility follows from the fact that the DOS has a 'kink' structure at $N = 3$ with $D_N(\varepsilon)$ increasing (decreasing) as a function of increasing energy for $N < 3$ ($N > 3$).

6.3 RKKY interaction and effective magnetic coupling

To study the effective magnetic coupling between random magnetic impurities (which are treated as quenched classical magnetic moments), we consider the carrier-mediated RKKY indirect exchange interaction. The indirect exchange interaction between magnetic impurities can be accounted for by the interaction between a localized (classical) spin $\boldsymbol{S}_i$ of a magnetic impurity located at $\boldsymbol{r}_i$ and an itinerant electron spin $\boldsymbol{s}$ located at $\boldsymbol{r}$. It is given by $V(\boldsymbol{r}) = J_{\rm ex}\boldsymbol{S}_i \cdot \boldsymbol{s}\delta(\boldsymbol{r}_i - \boldsymbol{r})$, where $J_{\rm ex}$ is the local exchange coupling between the quenched impurity and the itinerant carriers. ($J_{\rm ex}$, which depends on the nature of the magnetic impurities, is an unknown parameter in our theory providing the overall magnitude of the magnetic coupling in the system.) Then, the effective Hamiltonian that describes the magnetic interactions between the classical Heisenberg spins $\boldsymbol{S}_i$ and $\boldsymbol{S}_j$ located at $\boldsymbol{r}_i$ and $\boldsymbol{r}_j$, respectively, is given by

$$H = -\sum_{i,j} J_{\rm RKKY}(\boldsymbol{r}_i - \boldsymbol{r}_j)\boldsymbol{S}_i \cdot \boldsymbol{S}_j, \tag{6.4}$$

where

$$J_{\rm RKKY}(\boldsymbol{r}, T) = \frac{[J_{\rm ex}a^3]^2}{4}\chi(\boldsymbol{r}, T). \tag{6.5}$$

The RKKY range function $\chi(\boldsymbol{r}, T)$ is defined by the Fourier transform of the static susceptibility $\chi(\boldsymbol{q}, T)$. For an isotropic system in 3D, it is given by

$$\chi(\boldsymbol{r}, T) = \frac{1}{2\pi^2} \int_0^\infty q^2 dq j_0(qr) \chi(\boldsymbol{q}, T), \tag{6.6}$$

where $j_0(x)$ is the spherical Bessel function of the first kind. Since the large momentum cutoff q_c is natural for a continuum theory, we set $q_c = a^{-1}$ in the numerical calculation of the range function in Eq. (6.6).

Figure 6.2 shows the range functions for $N = 1, 2, 3, 4$ and for different temperatures. For $N = 1, 2$, the magnitude of the oscillating range functions increases with temperature, whereas for $N \geq 4$, it decreases with temperature. For $N = 3$, the range function is almost independent of temperature. These behaviors for different N follow from the temperature dependence of the susceptibility, which is shown in Fig. 6.1. At large distances ($r/a \gg 1$), we find that the range function decays as $\cos(q_c r)/r^2$ for $N \leq 3$, producing long-range oscillations with a periodicity of $2\pi/q_c$ in the spin density. (See Appendix D.1 for the detailed derivations.) We will discuss the implications of the cutoff q_c in the Discussion and Conclusion section (see Sec. 6.4).

The temperature-dependent effective coupling is given by the spatial average of the RKKY interaction J_{RKKY},

$$J_{\mathrm{eff}}(T) = \frac{1}{\Omega_{\mathrm{unit}}} \int d^3 r J_{\mathrm{RKKY}}(\boldsymbol{r}, T), \tag{6.7}$$

where Ω_{unit} is the volume of a unit cell. In the dimensionless form, Eq. (6.7) can be rewritten as

$$\frac{J_{\mathrm{eff}}(T)}{J_{\mathrm{eff}}^{(0)}} = \frac{1}{D_0(a^{-1})} \int r^2 dr \chi(\boldsymbol{r}, T), \tag{6.8}$$

where $J_{\mathrm{eff}}^{(0)} = 4\pi [J_{\mathrm{ex}} a^3]^2 D_0(a^{-1})/4\Omega_{\mathrm{unit}}$ and $D_0 = D_1(a^{-1})/a^3$. Note that the normalization factors $J_{\mathrm{eff}}^{(0)}$ and D_0 are defined to be independent of both index N and temperature T.

In the presence of non-magnetic impurity scattering arising from unintentional background disorder causing momentum relaxation, the RKKY interaction should be cut off at distances larger than a characteristic disorder length scale (i.e., the transport mean-free path), which is determined by the impurity scattering. We include the disorder effect phenomenologically by including an exponential damping at distances larger than the cutoff R in the range of the RKKY interaction. Then, the effective coupling is modified as

$$J_{\text{eff}}(T) = \begin{cases} \frac{1}{\Omega_{\text{unit}}} \int d^3r J_{\text{RKKY}}(\boldsymbol{r}) & (r < R), \\ \frac{1}{\Omega_{\text{unit}}} \int d^3r J_{\text{RKKY}}(\boldsymbol{r}) e^{-\frac{r-R}{R}} & (r > R). \end{cases} \tag{6.9}$$

(See Appendix D.2 for the detailed expression of the effective RKKY coupling with exponential cutoff.) In this calculation, we use $R = 100a$, and our calculated results do not depend on the choice of R qualitatively. One should think of R as a disorder-induced phenomenological effective carrier mean-free path parameter, which provides a cutoff for the RKKY interaction range. R should in general be smaller (larger) depending on the system being more (less) disordered. As a matter of principle, R cannot really be very large since the magnetic ordering phenomenon being studied here necessitates the presence of magnetic impurities, which, in addition to providing the quenched magnetic moments for ordering, also serve as momentum scatterers.

Figure 6.3 shows the calculated effective coupling as a function of temperature for different values of N. The effective coupling decreases monotonically with increasing temperature and increases with increasing N at a fixed temperature. Since the effective coupling $J_{\text{eff}}(T)$ is positive, the magnetic moments are expected to be ferromagnetically aligned.

From the temperature dependent effective coupling in Eq. (6.9), we calculate the magnetic transition temperature of the intrinsic chiral 3D semimetals. For

the Heisenberg classical spins, the mean-field transition temperature T_c is given by [159, 160]

$$k_B T_c = \frac{S(S+1)}{3} x J_{\text{eff}}, \tag{6.10}$$

where S and $x = n_{\text{imp}} a^3$ are the spin and concentration of the local magnetic moments, respectively, and n_{imp} is the effective magnetic impurity density. Since the calculated J_{eff} is a function of temperature, we calculate T_c self-consistently from Eq. (6.10). In Fig. 6.3, the intersections between the dashed line [i.e., $3k_B T/[S(S+1)x]$] and solid lines [i.e., $J_{\text{eff}}(T)$] determine the transition temperature for each N.

Figure 6.4 shows the self-consistently calculated transition temperature for different values of N as a function of the exchange coupling J_{ex}, the magnetic impurity concentration x, and the degeneracy factor g. The ferromagnetic transition temperature increases monotonically with increasing J_{ex}, x, and g for all N. In particular, for $N = 1$, T_c increases quadratically with J_{ex}, and linearly with both x and g, as expected [159, 160]. However, for $N > 1$, the calculated T_c shows non-trivial dependence on the parameters arising from self-consistency even for small values of the parameters, due to the non-trivial behavior of the temperature-dependent effective coupling shown in Fig. 6.3.

6.4 Discussion and conclusion

We studied theoretically the effective magnetic coupling between magnetic impurities and the consequent ferromagnetic transition temperature in 3D chiral gapless semimetals with arbitrary energy dispersion. To calculate the RKKY magnetic coupling range function, we introduced the momentum cutoff q_c, which is natural for the effective continuum model used in this work. We use the inverse lattice constant as the natural ultraviolet momentum cutoff in the the-

ory. As shown in Fig. 6.2, we find that for $N \leq 3$, the envelope of the oscillatory RKKY range function decays as r^{-2} and the period of the oscillation is $2\pi/q_c$. This decaying pattern arises from the finite ultraviolet cutoff q_c used in the range function. If we set the cutoff to be infinite, then the range function loses its oscillatory characteristics and monotonically decays as r^{-6+N}, which gives the typical r^{-5} decay for $N = 1$ [137, 138]. However, in the presence of a finite q_c, the overall behavior of the range function is determined by the competition between the oscillatory r^{-2} term and the non-oscillatory r^{-6+N} term. We find that for $N \leq 3$, the oscillatory r^{-2} decay dominates over the non-oscillatory r^{-6+N} term, but for $N > 3$ it is vice versa (see Appendix D.1 for the detailed derivations). We note that the cutoff dependence of the effective coupling and the corresponding transition temperature is insensitive to the precise quantitative choice of q_c. If the Pauli matrices in Eq. (6.1) refer to real spin degrees of freedom, in addition to the Heisenberg-type spin-spin interaction term, there appears the Ising-type spin-spin interaction term [137, 138]. The systematic evaluation of the transition temperature in that situation is beyond the scope of the current chapter, but we expect that the same power-law dependence which is fundamentally affected by presence of the cutoff will appear in this case. The study of the RKKY physics in the presence of both Heisenberg and Ising couplings remains an interesting theoretical problem for the future.

In summary, we investigate the temperature dependent susceptibility, RKKY interaction, and effective magnetic ordering for 3D chiral gapless semimetals with arbitrary energy dispersion in the presence of dilute random magnetic impurities. We find that in 3D chiral gapless semimetals, the ferromagnetic ordering between magnetic impurities is favored with enhanced magnetic coupling as the energy dispersion has a higher power-law. Our results indicate that ferromagnetic ordering between magnetic impurities is possible in 3D gapless

semimetals, arising entirely from the carrier-mediated indirect RKKY interaction in the dilute impurity limit. This predicted ferromagnetic ordering between magnetic impurities should be experimentally accessible with suitable magnetic doping. Our theory is valid when quantum fluctuations and direct exchange coupling between the impurity moments are negligible, which should be justified for large impurity spins and dilute impurity concentrations. In this chapter, we consider only the case of zero Fermi energy, and the effect of finite Fermi energy would be an interesting future research direction. Our finding that even the intrinsic undoped semimetallic system could be converted to a ferromagnet by dilute magnetic doping has obvious experimental implications, which should be explored in the laboratory.

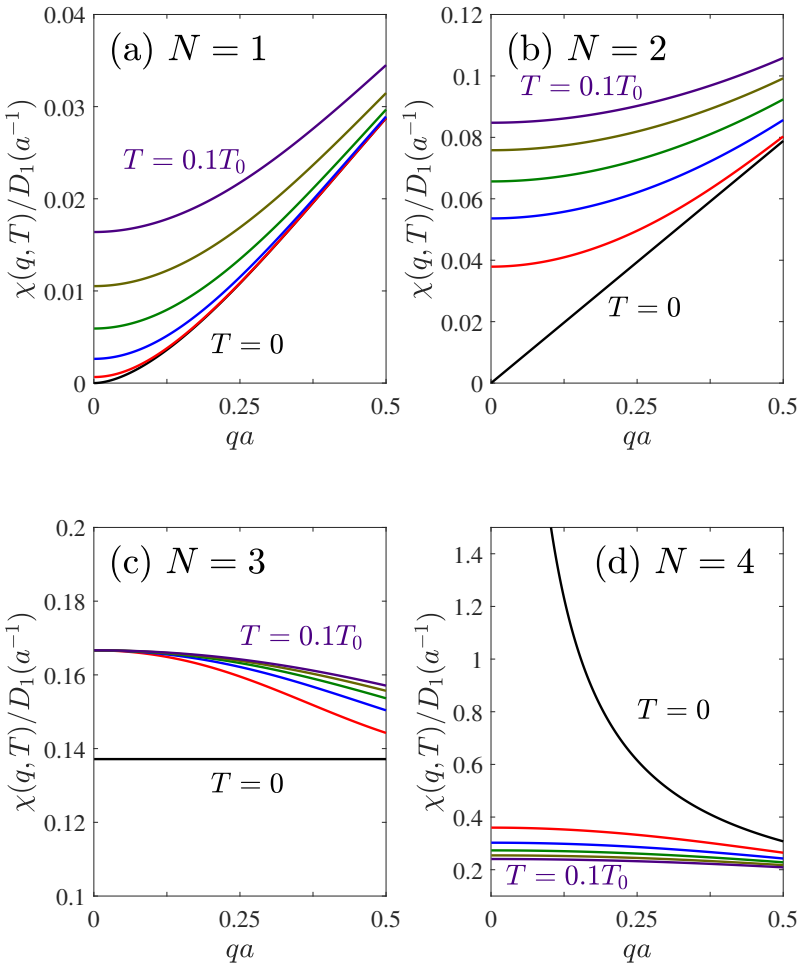

Figure 6.1 The calculated finite-temperature static susceptibility $\chi(\boldsymbol{q}, T)$ as a function of wave vector for various temperatures $T = 0, 0.02, 0.04, 0.06, 0.08,$ and $0.1\ T_0$, and for different values of N (a) $N = 1$, (b) $N = 2$, (c) $N = 3$, and (d) $N = 4$. Here, $T_0 = \varepsilon_0/k_{\mathrm{B}}$, $D_1(a^{-1}) = \frac{gk_0}{2\pi^2\varepsilon_0 a^2}$, and $a = 0.343$ nm (lattice constant of TaAs). For $N = 1$, the finite momentum cutoff a^{-1} is used for the convergence of the integral.

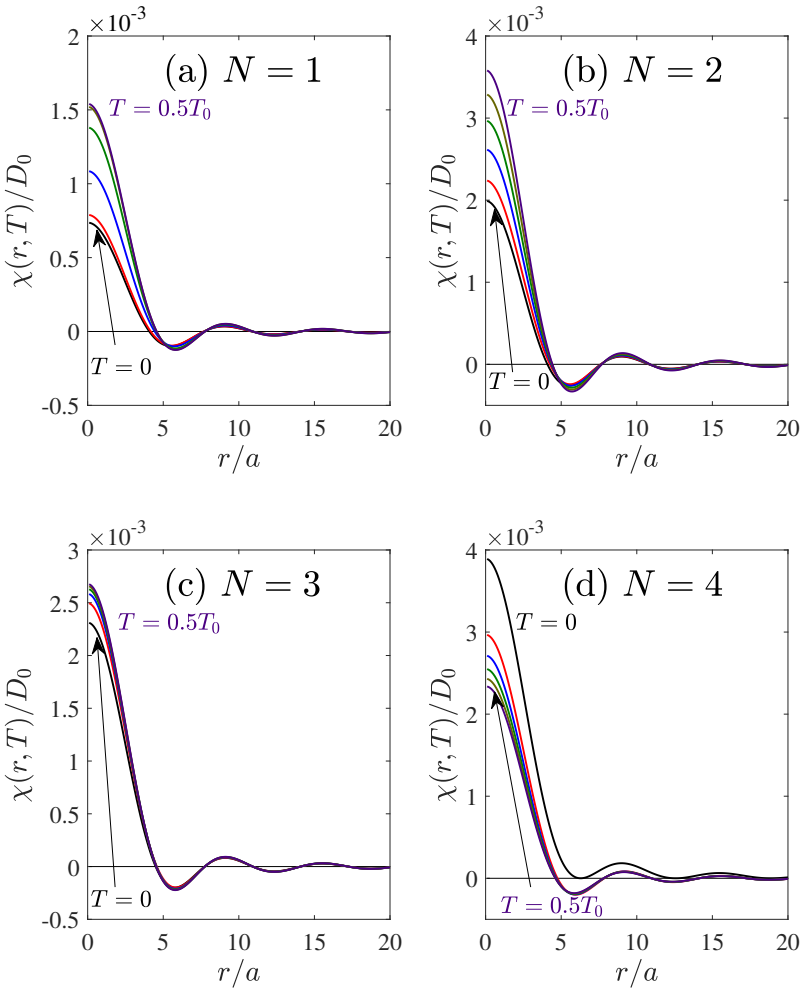

Figure 6.2 The range function $\chi(\boldsymbol{r}, T)$ as a function of distance for different values of N (a) $N = 1$, (b) $N = 2$, (c) $N = 3$, and (d) $N = 4$. In each figure, the curves with different colors represent different temperatures $T = 0$, 0.1, 0.2, 0.3, 0.4, and 0.5 T_0. Here, $D_0 = D_1(a^{-1})/a^3$. In this calculation, the ultraviolet momentum cutoff $q_c = a^{-1}$ is used.

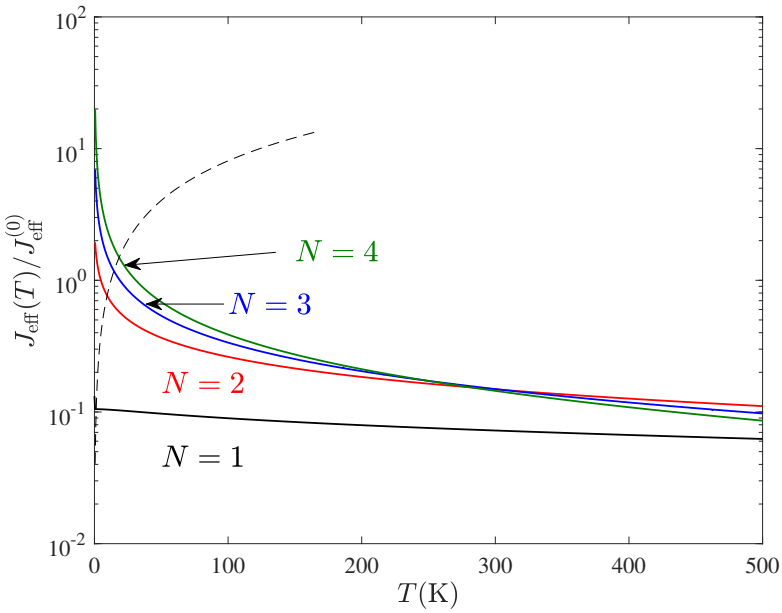

Figure 6.3 The calculated effective coupling (solid lines) as a function of temperature for different values of $N = 1, 2, 3, 4$. In this calculation, the ultraviolet cutoff $q_{\rm c} = a^{-1}$ and exponential cutoff $R = 100a$ are used. Here, the normalization factor $J_{\rm eff}^{(0)} = 4\pi[J_{\rm ex}a^3]^2 D_1(a^{-1})/4\Omega_{\rm unit}$ is independent of N and temperature T. The dashed line represents $3k_{\rm B}T/[S(S+1)x]$, and the intersections with $J_{\rm eff}(T)$ indicate the transition temperatures solved self-consistently. Here, $J_{\rm ex} = 0.1$ eV , $x = 0.05$ and $S = 5/2$.

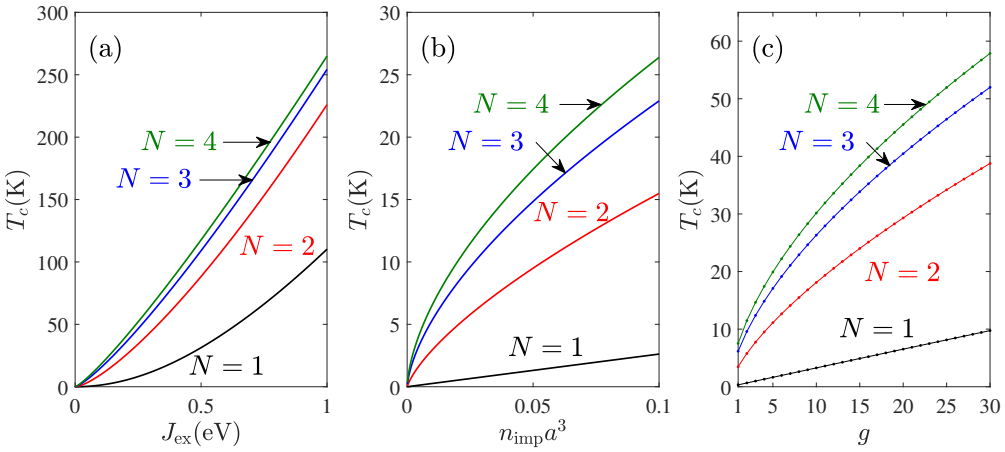

Figure 6.4 The calculated transition temperature $T_{\rm c}$ as a function of (a) the exchange coupling $J_{\rm ex}$, (b) the magnetic impurity concentration $x = n_{\rm imp}a^3$, and (c) the degeneracy factor g for different values of $N = 1, 2, 3, 4$. Here, for fixed parameters, we used $J_{\rm ex} = 0.1$ eV, $x = 0.05$ and $g = 4$.

Chapter 7

Conclusion

During my doctoral research period, I have mainly focused on developing semi-classical Boltzmann transport theory that can be applied to multi-band, anisotropic systems. We applied this theory on various systems such as multi-Weyl semimetals (m-WSMs), which are extension of Weyl semimetals with higher chiral charge, and band-gap tunable few-layer black phosphorus. We have also studied the transport behaviors from the magnetic field-driven anisotropy. We investigated charge carrier spin mediated magnetization of magnetic impurities as well, as known as Ruderman–Kittel–Kasuya–Yosida (RKKY) interaction on 3-dimensional (3D) chiral gas toy model. We summerize our findings down below.

For multi-Weyl semimetals, we developed the anisotropic Boltzmann transport equation that can be applied in the materials with different power-law dependences along its symmetry axes. Using this anisotropic transport equation, we calculated characteristic charge density, and temperature power-law dependence of m-WSM in its conductivity along each direction.

We have also studied the Boltzmann transport theory on few-layer black

phosphorus in various phases, extending our previous study on anisotropic systems to account for its multi-banded nature as well as its band anisotropy. We showed that its tunable band-gap gives rise to many interesting features in the electronic conductivity.

On top of that, we investigated the magnetic field-driven anisotropy and its effect on magnetotransport in systems where the Berry curvature effect is significant, e.g. Weyl semimetals. We argued that the external magnetic field (coupled with the Berry curvature of the system) makes the distribution of charged particles anisotropic, making the utilization of an anisotropic formulation a necessity.

Finally, we considered the dilute magnetic impurities embedded on the 3D chiral gas systems with arbitrary power-law dependence, where the impurities are sparse enough so that the direct magnetization is ignored and only the charge carrier spin-mediated indirect interaction is present. We found that the magnetic alignment in such condition, the system becomes ferromagnetic regardless of the dispersion relation power-law.

Appendix A

Semiclassical Boltzmann transport theory for multi-Weyl semimetals

A.1 Eigenstates and density of states for multi-Weyl semimetals

Let us consider the eigenstates and density of states (DOS) for the low-energy effective Hamiltonian of m-WSMs described by Eq. (3.1) in the main text:

$$H_J = \varepsilon_0 \begin{pmatrix} c_z \tilde{k}_z & \tilde{k}_-^J \\ \tilde{k}_+^J & -c_z \tilde{k}_z \end{pmatrix}, \tag{A.1}$$

where $\tilde{\boldsymbol{k}} = \boldsymbol{k}/k_0$ and $c_z = \hbar v_z k_0/\varepsilon_0$. To avoid difficulties associated with anisotropic dispersions, we consider the following coordinate transformation [37]

$$\begin{aligned} k_x &\to k_0 \left(r \sin\theta\right)^{\frac{1}{J}} \cos\phi, \\ k_y &\to k_0 \left(r \sin\theta\right)^{\frac{1}{J}} \sin\phi, \\ k_z &\to \frac{k_0}{c_z} r \cos\theta, \end{aligned} \tag{A.2}$$

which transforms the Hamiltonian into the following form:

$$H = \varepsilon_0 r \begin{pmatrix} \cos\theta & \sin\theta e^{-iJ\phi} \\ \sin\theta e^{iJ\phi} & -\cos\theta \end{pmatrix}. \tag{A.3}$$

In the transformed coordinates, the energy dispersion is given by $\varepsilon_\pm(r) = \pm\varepsilon_0 r$ and the corresponding eigenstate is given by

$$|+\rangle = \begin{pmatrix} \cos\frac{\theta}{2} \\ \sin\frac{\theta}{2} e^{iJ\phi} \end{pmatrix}, \tag{A.4a}$$

$$|-\rangle = \begin{pmatrix} -\sin\frac{\theta}{2} \\ \cos\frac{\theta}{2} e^{iJ\phi} \end{pmatrix}. \tag{A.4b}$$

The Jacobian $\mathcal{J}$ corresponding to this transformation is given by

$$\mathcal{J} = \begin{vmatrix} \frac{\partial k_x}{\partial r} & \frac{\partial k_x}{\partial \theta} & \frac{\partial k_x}{\partial \phi} \\ \frac{\partial k_y}{\partial r} & \frac{\partial k_y}{\partial \theta} & \frac{\partial k_y}{\partial \phi} \\ \frac{\partial k_z}{\partial r} & \frac{\partial k_z}{\partial \theta} & \frac{\partial k_z}{\partial \phi} \end{vmatrix} = \frac{k_0^3}{c_z J} r^{\frac{2}{J}} \sin^{\frac{2}{J}-1}\theta \equiv \mathcal{J}(r,\theta). \tag{A.5}$$

Note that for the + band, the band velocity $v_{\boldsymbol{k}}^{(i)} = \frac{1}{\hbar}\frac{\varepsilon_{+,\boldsymbol{k}}}{\partial k_i}$ can be expressed as

$$v_{\boldsymbol{k}}^{(x)} = J v_0 r^{1-\frac{1}{J}} \sin^{2-\frac{1}{J}}\theta \cos\phi, \tag{A.6a}$$

$$v_{\boldsymbol{k}}^{(y)} = J v_0 r^{1-\frac{1}{J}} \sin^{2-\frac{1}{J}}\theta \sin\phi, \tag{A.6b}$$

$$v_{\boldsymbol{k}}^{(z)} = c_z v_0 \cos\theta, \tag{A.6c}$$

where $v_0 = \frac{\varepsilon_0}{\hbar k_0}$.

The DOS at energy $\varepsilon > 0$ can be obtained as

$$\begin{aligned} D(\varepsilon) &= g\int \frac{d^3k}{(2\pi)^3}\delta(\varepsilon - \varepsilon_{+,\boldsymbol{k}}) \\ &= g\int_0^\infty dr \int_0^\pi d\theta \int_0^{2\pi} d\phi \frac{\mathcal{J}(r,\theta)}{(2\pi)^3}\delta(\varepsilon - \varepsilon_0 r) \\ &= \frac{gB\left(\frac{1}{2},\frac{1}{J}\right)}{4\pi^2 c_z J}\frac{k_0^3}{\varepsilon_0}\left(\frac{\varepsilon}{\varepsilon_0}\right)^{\frac{2}{J}}, \end{aligned} \tag{A.7}$$

where g is the number of degenerate Weyl nodes. Here, we used the relation $\int_0^{\pi/2} d\theta \cos^m\theta \sin^n\theta = \frac{1}{2}B(\frac{m+1}{2}, \frac{n+1}{2})$, where $B(m,n) = \frac{\Gamma(m)\Gamma(n)}{\Gamma(m+n)}$ is the beta function and $\Gamma(x) = \int_0^\infty dt\, t^{x-1}e^{-t}$ is the gamma function [45]. Note that the Thomas-Fermi wavevector is determined by the DOS at the Fermi energy $\varepsilon_{\rm F}$ given by

$$q_{\rm TF} = \sqrt{\frac{4\pi e^2}{\kappa} D(\varepsilon_{\rm F})} = k_0 \sqrt{\frac{g\alpha B\left(\frac{1}{2}, \frac{1}{J}\right)}{\pi c_z J}} \left(\frac{\varepsilon_{\rm F}}{\varepsilon_0}\right)^{\frac{1}{J}}, \tag{A.8}$$

where $\alpha = \frac{e^2}{\kappa\hbar v_0}$ is the effective fine structure constant.

The carrier density is then given by

$$n = \int_0^{\varepsilon_{\rm F}} d\varepsilon D(\varepsilon) = n_0 \frac{gB\left(\frac{1}{2}, \frac{1}{J}\right)}{4\pi^2 c_z (J+2)} \left(\frac{\varepsilon_{\rm F}}{\varepsilon_0}\right)^{\frac{2}{J}+1}, \tag{A.9}$$

where $n_0 = k_0^3$. Note that $\varepsilon_{\rm F} \sim n^{\frac{J}{J+2}}$ and $D(\varepsilon_{\rm F}) \sim n^{\frac{2}{J+2}}$.

A.2 Density dependence of dc conductivity in multi-Weyl semimetals at zero temperature

In this section, we derive the dc conductivity at zero temperature for 3D anisotropic systems with an anisotropic energy dispersion which has an axial symmetry around the k_z-axis (i.e. independent of ϕ), as in the m-WSMs described by Eq. (3.1) in the main text. To take into account the anisotropy of the energy dispersion, we express the anisotropic Boltzmann equation in Eq. (4.7) in the main text using the transformed coordinates in Eq. (A.5) assuming an

axial symmetry around the k_z-axis:

$$
\begin{aligned}
1 &= \int_0^\infty dr' \int_0^\pi d\theta' \int_0^{2\pi} d\phi' \frac{\mathcal{J}(r',\theta')}{(2\pi)^3} W_{\boldsymbol{k}\boldsymbol{k}'} \left(\tau_{\boldsymbol{k}}^{(i)} - \frac{v_{\boldsymbol{k}'}^{(i)}}{v_{\boldsymbol{k}}^{(i)}} \tau_{\boldsymbol{k}'}^{(i)} \right) \\
&= \int_0^\infty dr' \int_0^\pi d\theta' \int_0^{2\pi} d\phi' \frac{k_0^3 r'^{\frac{2}{J}} \sin^{\frac{2}{J}-1}\theta'}{(2\pi)^3 c_z J} \left[\frac{2\pi}{\hbar} n_{\mathrm{imp}} |V_{\boldsymbol{k}\boldsymbol{k}'}|^2 F_{\boldsymbol{k}\boldsymbol{k}'} \delta(\varepsilon_0 r - \varepsilon_0 r') \right] \\
&\times \left(\tau_{\boldsymbol{k}}^{(i)} - d_{\boldsymbol{k}\boldsymbol{k}'}^{(i)} \tau_{\boldsymbol{k}'}^{(i)} \right) \\
&= \frac{2\pi}{\hbar} n_{\mathrm{imp}} \frac{k_0^3 r^{\frac{2}{J}}}{(2\pi)^2 c_z J \varepsilon_0} \int_{-1}^1 d\cos\theta' (1-\cos^2\theta')^{\frac{1}{J}-1} \\
&\times \int_0^{2\pi} \frac{d\phi'}{2\pi} |V_{\boldsymbol{k}\boldsymbol{k}'}|^2 F_{\boldsymbol{k}\boldsymbol{k}'} \left(\tau_{\boldsymbol{k}}^{(i)} - d_{\boldsymbol{k}\boldsymbol{k}'}^{(i)} \tau_{\boldsymbol{k}'}^{(i)} \right), \qquad \text{(A.10)}
\end{aligned}
$$

where $d_{\boldsymbol{k}\boldsymbol{k}'}^{(i)} = v_{\boldsymbol{k}'}^{(i)} / v_{\boldsymbol{k}}^{(i)}$ and $F_{\boldsymbol{k}\boldsymbol{k}'} = \frac{1}{2}\left[1 + \cos\theta\cos\theta' + \sin\theta\sin\theta'\cos J(\phi - \phi')\right]$ is the square of the wavefunction overlap between $\boldsymbol{k}$ and $\boldsymbol{k}'$ states in the same band. Let us define $\rho_0 = \frac{k_0^3}{(2\pi)^2 c_z \varepsilon_0}$, $V_0 = \frac{\varepsilon_0}{k_0^3}$, and $\frac{1}{\tau_0(r)} = \frac{2\pi}{\hbar} n_{\mathrm{imp}} V_0^2 \rho_0$. Then with $\mu = \cos\theta$, we have

$$
1 = \frac{r^{\frac{2}{J}}}{J} \int_{-1}^1 d\mu' (1-\mu'^2)^{\frac{1}{J}-1} \int_0^{2\pi} \frac{d\phi'}{2\pi} |\tilde{V}_{\boldsymbol{k}\boldsymbol{k}'}|^2 F_{\boldsymbol{k}\boldsymbol{k}'} \left(\tilde{\tau}_{\boldsymbol{k}}^{(i)} - d_{\boldsymbol{k}\boldsymbol{k}'}^{(i)} \tilde{\tau}_{\boldsymbol{k}'}^{(i)} \right), \qquad \text{(A.11)}
$$

where $\tilde{V}_{\boldsymbol{k}\boldsymbol{k}'} = V_{\boldsymbol{k}\boldsymbol{k}'} / V_0$ and $\tilde{\tau}_{\boldsymbol{k}}^{(i)} = \tau_{\boldsymbol{k}}^{(i)} / \tau_0$.

Assuming $\tilde{\tau}_{\boldsymbol{k}}^{(i)} = \tilde{\tau}^{(i)}(\mu)$ from the axial symmetry,

$$
1 = \tilde{w}^{(i)}(\mu)\tilde{\tau}^{(i)}(\mu) - \int_{-1}^1 d\mu' \tilde{w}^{(i)}(\mu,\mu')\tilde{\tau}^{(i)}(\mu'), \qquad \text{(A.12)}
$$

where

$$
\begin{aligned}
\tilde{w}^{(i)}(\mu) &= \frac{r^{\frac{2}{J}}}{J} \int_{-1}^1 d\mu' (1-\mu'^2)^{\frac{1}{J}-1} \int_0^{2\pi} \frac{d\phi'}{2\pi} |\tilde{V}_{\boldsymbol{k}\boldsymbol{k}'}|^2 F_{\boldsymbol{k}\boldsymbol{k}'}, \qquad \text{(A.13a)} \\
\tilde{w}^{(i)}(\mu,\mu') &= \frac{r^{\frac{2}{J}}}{J} (1-\mu'^2)^{\frac{1}{J}-1} \int_0^{2\pi} \frac{d\phi'}{2\pi} |\tilde{V}_{\boldsymbol{k}\boldsymbol{k}'}|^2 F_{\boldsymbol{k}\boldsymbol{k}'} d_{\boldsymbol{k}\boldsymbol{k}'}^{(i)}. \qquad \text{(A.13b)}
\end{aligned}
$$

Now let us discretize θ or equivalently $\mu = \cos\theta$ to μ_n $(n = 1, 2, \cdots, N)$ with an interval $\Delta\mu = 2/N$. Then for $\tilde{\tau}_n^{(i)} = \tilde{\tau}^{(i)}(\mu_n)$, we have

$$
1 = P_n^{(i)} \tilde{\tau}_n^{(i)} - \sum_{n'} P_{nn'}^{(i)} \tilde{\tau}_{n'}^{(i)}, \qquad \text{(A.14)}
$$

where $P_n^{(i)} = \tilde{w}^{(i)}(\mu_n)$ is an N-vector and $P_{nn'}^{(i)} = \tilde{w}^{(i)}(\mu_n, \mu_{n'})\Delta\mu$ is an $N \times N$ matrix which relate the θ-dependent relaxation times. Note that Eq. (B.16) has a similar structure for the multiband scattering [68] in which the relaxation time can be obtained by solving coupled equations, which relate the relaxation times for different energy bands involved in the scattering.

Then the dc conductivity at zero temperature is given by

$$\begin{aligned}
\sigma_{ij} &= ge^2 \int \frac{d^3k}{(2\pi)^3} \delta(\varepsilon_{\boldsymbol{k}} - \varepsilon_{\rm F}) v_{\boldsymbol{k}}^{(i)} v_{\boldsymbol{k}}^{(j)} \tau_{\boldsymbol{k}}^{(j)} \\
&= ge^2 \int_0^\infty dr \int_0^\pi d\theta \int_0^{2\pi} d\phi \frac{k_0^3 r^{\frac{2}{J}} \sin^{\frac{2}{J}-1}\theta}{(2\pi)^3 c_z J} \delta(\varepsilon_0 r - \varepsilon_{\rm F}) v_{\boldsymbol{k}}^{(i)} v_{\boldsymbol{k}}^{(j)} \tau_{\boldsymbol{k}}^{(j)} \\
&= \frac{\sigma_0}{J} \int_0^\infty dr r^{\frac{2}{J}} \int_{-1}^1 d\mu \left(1-\mu^2\right)^{\frac{1}{J}-1} \int_0^{2\pi} \frac{d\phi}{2\pi} \delta(r - r_{\rm F}) \tilde{v}_{\boldsymbol{k}}^{(i)} \tilde{v}_{\boldsymbol{k}}^{(j)} \tilde{\tau}_{\boldsymbol{k}}^{(j)},
\end{aligned} \tag{A.15}$$

where $\sigma_0 = ge^2\rho_0 v_0^2 \tau_0$, $r_{\rm F} = \varepsilon_{\rm F}/\varepsilon_0$, and $\tilde{v}_{\boldsymbol{k}}^{(i)} = v_{\boldsymbol{k}}^{(i)}/v_0$. Thus, from Eq. (A.6), we have

$$\frac{\sigma_{xx}}{\sigma_0} = \frac{J r_{\rm F}^2}{2} \int_{-1}^1 d\mu \left(1-\mu^2\right) \tilde{\tau}^{(x)}(\mu), \tag{A.16a}$$

$$\frac{\sigma_{zz}}{\sigma_0} = \frac{c_z^2 r_{\rm F}^{\frac{2}{J}}}{J} \int_{-1}^1 d\mu \left(1-\mu^2\right)^{\frac{1}{J}-1} \mu^2 \tilde{\tau}^{(z)}(\mu). \tag{A.16b}$$

Note that τ_0, v_0, ρ_0 and σ_0 are the density independent normalization constants in units of time, velocity, DOS, and conductivity, respectively. In addition, from the axial symmetry around the k_z-axis, $\sigma_{xx} = \sigma_{yy}$.

For the short-range impurities, $V_{\boldsymbol{k}\boldsymbol{k}'}$ is independent of density. Thus from Eq. (B.14), $\tilde{\omega}^{(i)}(\mu) \sim \varepsilon_{\rm F}^{\frac{2}{J}}$ and $\tilde{\tau}^{(i)}(\mu) \sim \varepsilon_{\rm F}^{-\frac{2}{J}}$ at the Fermi energy $\varepsilon_{\rm F}$. Note that $\varepsilon_{\rm F} \sim n^{\frac{J}{J+2}}$. Therefore we have

$$\sigma_{xx} \sim \varepsilon_{\rm F}^{2-\frac{2}{J}} \sim n^{\frac{2(J-1)}{J+2}}, \tag{A.17a}$$

$$\sigma_{zz} \sim \varepsilon_{\rm F}^0 \sim n^0. \tag{A.17b}$$

For charged impurities in the strong screening limit, $V_{\boldsymbol{k}\boldsymbol{k}'} \sim q_{\mathrm{TF}}^{-2} \sim D^{-1}(\varepsilon_{\mathrm{F}}) \sim \varepsilon_{\mathrm{F}}^{-\frac{2}{J}}$, thus $\tilde{\omega}^{(i)}(\mu) \sim \varepsilon_{\mathrm{F}}^{\frac{2}{J}-\frac{4}{J}}$ and $\tilde{\tau}^{(i)}(\mu) \sim \varepsilon_{\mathrm{F}}^{\frac{2}{J}}$ at ε_{F}. Therefore we have

$$\sigma_{xx} \sim \varepsilon_{\mathrm{F}}^{2+\frac{2}{J}} \sim n^{\frac{2(J+1)}{J+2}}, \tag{A.18a}$$

$$\sigma_{zz} \sim \varepsilon_{\mathrm{F}}^{\frac{4}{J}} \sim n^{\frac{4}{J+2}}. \tag{A.18b}$$

For charged impurities in the weak screening limit, from $V_{\boldsymbol{k}\boldsymbol{k}'} \sim |\boldsymbol{k}-\boldsymbol{k}'|^{-2}$ and Eq. (A.2), we expect the potential average on the Fermi surface as $V_{\mathrm{F}} \sim \varepsilon_{\mathrm{F}}^{-2\zeta}$ with $\frac{1}{J} \leq \zeta \leq 1$ (assuming no logarithmic correction), thus $\tilde{\omega}^{(i)}(\mu) \sim \varepsilon_{\mathrm{F}}^{\frac{2}{J}-4\zeta}$ and $\tilde{\tau}^{(i)}(\mu) \sim \varepsilon_{\mathrm{F}}^{4\zeta-\frac{2}{J}}$ at ε_{F}. Therefore, we have

$$\sigma_{xx} \sim \varepsilon_{\mathrm{F}}^{2+4\zeta-\frac{2}{J}} \sim n^{\frac{2(J-1)+4J\zeta}{J+2}}, \tag{A.19a}$$

$$\sigma_{zz} \sim \varepsilon_{\mathrm{F}}^{4\zeta} \sim n^{\frac{4J\zeta}{J+2}}. \tag{A.19b}$$

Here, ζs in σ_{xx} and σ_{zz} do not need to be the same, as explained later in this section. Note that $\zeta = \frac{1}{J}$ gives the same density exponent corresponding to the strong screening limit.

For the short-range impurities, it turns out that the relaxation time is independent of polar angles θ. Assuming $\tau^{(i)}(\mu) = \tau^{(i)}$ from the beginning, for short-range impurity potential $V_{\boldsymbol{k}\boldsymbol{k}'} = V_{\mathrm{short}}$, Eq. (B.12) reduces to

$$\frac{1}{\tilde{\tau}^{(i)}} = \frac{r^{\frac{2}{J}}}{J}\tilde{V}_{\mathrm{short}}^2 \int_{-1}^{1} d\mu' (1-\mu'^2)^{\frac{1}{J}-1} \int_0^{2\pi} \frac{d\phi'}{2\pi} F_{\boldsymbol{k}\boldsymbol{k}'} \left(1 - d_{\boldsymbol{k}\boldsymbol{k}'}^{(i)}\right), \tag{A.20}$$

where $\tilde{V}_{\mathrm{short}} = V_{\mathrm{short}}/V_0$. Then we find that the relaxation time $\tau^{(i)}(\varepsilon)$ at at energy $\varepsilon = r\varepsilon_0$ is

$$\frac{1}{\tilde{\tau}^{(x)}(\varepsilon)} = \frac{r^{\frac{2}{J}}}{2J}\tilde{V}_{\mathrm{short}}^2 B\left(\frac{1}{2}, \frac{1}{J}\right) - \delta_{J1}\frac{r^2}{3}\tilde{V}_{\mathrm{short}}^2, \tag{A.21a}$$

$$\frac{1}{\tilde{\tau}^{(z)}(\varepsilon)} = \frac{r^{\frac{2}{J}}}{2J}\tilde{V}_{\mathrm{short}}^2 B\left(\frac{1}{2}, \frac{1}{J}+1\right). \tag{A.21b}$$

From Eq. (B.18), finally we obtain

$$\frac{\sigma_{xx}}{\sigma_0} = \frac{2Jr_{\rm F}^2}{3}\tilde{\tau}^{(x)}(\varepsilon_{\rm F}), \tag{A.22a}$$

$$\frac{\sigma_{zz}}{\sigma_0} = \frac{c_z^2 r_{\rm F}^{\frac{2}{J}}}{J} B\left(\frac{3}{2},\frac{1}{J}\right)\tilde{\tau}^{(z)}(\varepsilon_{\rm F}) = \frac{Jc_z^2}{\tilde{V}_{\rm short}^2}. \tag{A.22b}$$

Note that $\sigma_{xx}/\sigma_0 = \tilde{V}_{\rm short}^{-2}$, $\frac{16}{3\pi} r_{\rm F}\tilde{V}_{\rm short}^{-2}$, $\frac{12}{B\left(\frac{1}{2},\frac{1}{3}\right)} r_{\rm F}^{\frac{4}{3}}\tilde{V}_{\rm short}^{-2}$ for $J = 1, 2, 3$, respectively, and the obtained analytic expressions are consistent with the density dependence in Eq. (A.17). From Eq. (A.22), we find $\sigma_{xx}/\sigma_{zz} = \frac{1}{c_z^2}$, $\frac{8r_{\rm F}}{3\pi c_z^2}$, $\frac{4r_{\rm F}^{\frac{4}{3}}}{B\left(\frac{1}{2},\frac{1}{3}\right)c_z^2}$ for $J = 1, 2, 3$, respectively, and the anisotropy between σ_{xx} and σ_{zz} increases as the Fermi energy or the carrier density increases.

For charged impurities in the strong screening limit, the impurity potential becomes $V_{\boldsymbol{kk'}} \approx V_{\rm screen}^{\rm strong} \equiv \frac{4\pi e^2}{\kappa q_{\rm TF}^2}$, having the same feature of the short-range impurity potential. Thus, the relaxation time is also independent of polar angles and similar analytic expressions can be obtained by replacing $\tilde{V}_{\rm short}$ by $\tilde{V}_{\rm screen}^{\rm strong}$ in Eqs. (A.21) and (A.22), where $\tilde{V}_{\rm screen}^{\rm strong} = V_{\rm screen}^{\rm strong}/V_0 = 4\pi\alpha k_0^2/q_{\rm TF}^2$. Then the relaxation time is given by

$$\frac{1}{\tilde{\tau}^{(x)}(\varepsilon)} = \frac{8\pi^4 c_z^2 J}{g^2 B\left(\frac{1}{2},\frac{1}{J}\right)} r^{\frac{2}{J}} r_{\rm F}^{-\frac{4}{J}} - \delta_{J1}\frac{4\pi^4 c_z^2}{3g^2} r^2 r_{\rm F}^{-4}, \tag{A.23a}$$

$$\frac{1}{\tilde{\tau}^{(z)}(\varepsilon)} = \frac{16\pi^4 c_z^2 J}{(J+2)g^2 B\left(\frac{1}{2},\frac{1}{J}\right)} r^{\frac{2}{J}} r_{\rm F}^{-\frac{4}{J}}, \tag{A.23b}$$

thus, in the strong screening limit, we obtain

$$\frac{\sigma_{xx}}{\sigma_0} = \frac{2Jr_{\rm F}^2}{3}\tilde{\tau}^{(x)}(\varepsilon_{\rm F}), \tag{A.24a}$$

$$\frac{\sigma_{zz}}{\sigma_0} = \frac{c_z^2 r_{\rm F}^{\frac{2}{J}}}{J} B\left(\frac{3}{2},\frac{1}{J}\right)\tilde{\tau}^{(z)}(\varepsilon_{\rm F}) = \frac{g^2 B^2\left(\frac{1}{2},\frac{1}{J}\right)}{16\pi^4 J} r_{\rm F}^{\frac{4}{J}}. \tag{A.24b}$$

Note that $\sigma_{xx}/\sigma_0 = \frac{g^2}{4\pi^4 c_z^2} r_{\rm F}^4$, $\frac{g^2}{12\pi^3 c_z^2} r_{\rm F}^3$, $\frac{g^2 B\left(\frac{1}{2},\frac{1}{3}\right)}{12\pi^4 c_z^2} r_{\rm F}^{\frac{8}{3}}$ for $J = 1, 2, 3$, respectively, and the obtained analytic expressions are consistent with the density dependence in Eq. (A.18). Also note that σ_{xx}/σ_{zz} has the same form with that obtained for short-range impurities.

For charged impurities at arbitrary screening, the relaxation time in general depends on polar angles for $J > 1$. In addition, as seen in Fig. 3.2 in the main text, the density exponent shows non-monotonic behavior as a function of $g\alpha$. From Eq. (B.11), for a given wavevector $\boldsymbol{k} = (k_0 (r_{\rm F} \sin\theta)^{\frac{1}{J}}, 0, \frac{k_0}{c_z} r_{\rm F} \cos\theta)$ at the Fermi energy, the average of the squared Coulomb potential on the Fermi surface is given by

$$\left\langle V^2(\theta) \right\rangle_{\rm F} = \frac{1}{2} \int_{-1}^{1} d\cos\theta' (1 - \cos^2\theta')^{\frac{1}{J}-1} \int_0^{2\pi} \frac{d\phi'}{2\pi} |V_{\boldsymbol{k}\boldsymbol{k}'}|^2. \tag{A.25}$$

Then assuming $\left\langle V^2(\theta) \right\rangle_{\rm F} \sim r_{\rm F}^{-4\zeta(\theta)}$, we can obtain the angle dependent exponent $\zeta(\theta)$ with $\frac{1}{J} \leq \zeta(\theta) \leq 1$. Figure A.1 shows $\zeta(\theta)$ for several values of $\theta = 0, \pi/6, \pi/2$. This angle-dependent power-law gives rise to a significant non-monotonic behavior of τ_z and σ_{zz} in $g\alpha$, which originates from the competition between two inverse length scales, $q_{\rm TF} \sim r_{\rm F}^{\frac{1}{J}}$ and $k_{\rm F}^{(z)} \sim r_{\rm F}$. Note that the in-plane component of the wavevector $k_{\rm F}^{(\parallel)} \sim r_{\rm F}^{\frac{1}{J}}$ at the Fermi energy has the same Fermi energy dependence with $q_{\rm TF}$, showing a monotonic-like behavior of τ_x and σ_{xx} in $g\alpha$. As $g\alpha$ increases, $\zeta(\theta)$ eventually approaches $1/J$ irrespective of θ, obtained in the strong screening limit.

A.3 Temperature dependence of chemical potential and Thomas-Fermi wavevector in multi-Weyl semimetals

In this section, we derive the temperature dependent chemical potential and Thomas-Fermi wavevector in a general gapless electron-hole system, and apply the results to m-WSMs. Suppose that a gapless electron-hole system has a DOS given by $D(\varepsilon) = C_\alpha |\varepsilon|^{\alpha-1} \Theta(\varepsilon)$, where C_α is a constant and $\Theta(\varepsilon)$ is a step function. For a d-dimensional electron gas with an isotropic energy dispersion

$\varepsilon \sim k^J$, $\alpha = d/J$, whereas for m-WSMs, $D(\varepsilon) \propto \varepsilon^{\frac{2}{J}}$ from Eq. (A.7), thus $\alpha = \frac{2}{J} + 1$.

When the temperature is finite, the chemical potential μ deviates from the Fermi energy $\varepsilon_{\rm F}$ due to the broadening of the Fermi distribution function $f^{(0)}(\varepsilon, \mu) = \left[e^{\beta(\varepsilon-\mu)} + 1\right]^{-1}$ where $\beta = \frac{1}{k_{\rm B}T}$. Since the charge carrier density n does not vary under the temperature change, we have

$$n = \int_{-\infty}^{\infty} d\varepsilon D(\varepsilon) f^{(0)}(\varepsilon, \mu) = \int_{0}^{\infty} d\varepsilon D(\varepsilon) \left[f^{(0)}(\varepsilon, \mu) + f^{(0)}(-\varepsilon, \mu)\right] \equiv \int_{-\infty}^{\varepsilon_{\rm F}} d\varepsilon D(\varepsilon). \tag{A.26}$$

Then the carrier density measured from the charge neutral point, $\Delta n \equiv n|_{\mu} - n|_{\mu=0}$, is given by

$$\Delta n = \int_{0}^{\infty} d\varepsilon D(\varepsilon) \left[f^{(0)}(\varepsilon, \mu) - f^{(0)}(\varepsilon, -\mu)\right] \equiv \int_{0}^{\varepsilon_{\rm F}} d\varepsilon D(\varepsilon). \tag{A.27}$$

Here, we used $f(-\varepsilon, \mu) = 1 - f(\varepsilon, -\mu)$.

Before proceeding further, let us consider the following integral:

$$\begin{aligned} \int_0^\infty dx \frac{x^{\alpha-1}}{z^{-1}e^x + 1} &= \int_0^\infty dx \frac{x^{\alpha-1} z e^{-x}}{1 + z e^{-x}} = -\int_0^\infty dx x^{\alpha-1} \sum_{n=1}^{\infty} (-z)^n e^{-nx} \\ &\overset{t=nx}{=} \left[\int_0^\infty dt\, t^{n-1} e^{-t}\right] \left[-\sum_{n=1}^{\infty} \frac{(-z)^n}{n^\alpha}\right] = \Gamma(\alpha) F_\alpha(z), \end{aligned} \tag{A.28}$$

where $\Gamma(\alpha) = \int_0^\infty dt\, t^{\alpha-1} e^{-t}$ is the gamma function and $F_\alpha(z) = -\sum_{n=1}^{\infty} \frac{(-z)^n}{n^\alpha}$. Note that $\Gamma(\alpha) = (\alpha - 1)\Gamma(\alpha - 1)$ with $\Gamma(1) = 1$ and $\Gamma(1/2) = \sqrt{\pi}$, and $F_\alpha(z) = z\frac{\partial}{\partial z} F_{\alpha+1}(z)$.

Using the above result, we obtain

$$\Delta n = C_\alpha (k_{\rm B}T)^\alpha \Gamma(\alpha) \left[F_\alpha(z) - F_\alpha(z^{-1})\right] = \frac{C_\alpha}{\alpha} \varepsilon_{\rm F}^\alpha, \tag{A.29}$$

where $z = e^{\beta\mu}$, which is called the fugacity. Thus, finally we have

$$F_\alpha(z) - F_\alpha(z^{-1}) = \frac{(\beta\varepsilon_{\rm F})^\alpha}{\Gamma(\alpha + 1)}. \tag{A.30}$$

By solving the above equation with respect to z for a given T, we can obtain the chemical potential $\mu = k_{\mathrm{B}} T \ln z$.

At low temperatures, $\beta\mu \to \infty$ thus $z \to \infty$. Note that from the Sommerfeld expansion [40]

$$\lim_{z\to\infty} \int_0^\infty dx \frac{H(x)}{z^{-1}e^x + 1} \approx \int_0^{\beta\mu} dx H(x) + \frac{\pi^2}{6} \frac{\partial H(\beta\mu)}{\partial x}, \tag{A.31}$$

where $H(x)$ is a function which diverges no more rapidly than a polynomial as $x \to \infty$. Then for $H(x) = x^{\alpha-1}$ and using Eq. (A.28), Eq. (A.31) becomes

$$\lim_{z\to\infty} F_\alpha(z) \approx \frac{(\beta\mu)^\alpha}{\Gamma(\alpha+1)} \left[1 + \frac{\pi^2}{6} \frac{\alpha(\alpha-1)}{(\beta\mu)^2}\right], \tag{A.32}$$

whereas $F_\alpha(z^{-1}) = z^{-1} - \frac{z^{-2}}{2^\alpha} + \cdots$ vanishes as $z \to \infty$. Thus, we can obtain the low-temperature correction as

$$\frac{\mu}{\varepsilon_{\mathrm{F}}} \approx 1 - \frac{\pi^2}{6} (\alpha - 1) \left(\frac{T}{T_{\mathrm{F}}}\right)^2, \tag{A.33}$$

where $T_{\mathrm{F}} = \varepsilon_{\mathrm{F}}/k_{\mathrm{B}}$ is the Fermi temperature.

At high temperatures, $\beta\mu \to 0$ due to the finite carrier densities, thus $z \to 1$. From $z \approx 1 + \beta\mu + \frac{1}{2}(\beta\mu)^2$ for $|\beta\mu| \ll 1$,

$$\lim_{z\to 1} F_\alpha(z) \approx \eta(\alpha) + \eta(\alpha-1)\beta\mu + \frac{1}{2}\eta(\alpha-2)\,(\beta\mu)^2, \tag{A.34}$$

where $\eta(\alpha) = F_\alpha(1)$ is the Dirichlet eta function [45]. Thus, we have $F_\alpha(z) - F_\alpha(z^{-1}) \approx 2\eta(\alpha-1)\beta\mu$, and obtain the following high-temperature asymptotic form:

$$\frac{\mu}{\varepsilon_{\mathrm{F}}} \approx \frac{1}{2\eta(\alpha-1)\Gamma(\alpha+1)} \left(\frac{T_{\mathrm{F}}}{T}\right)^{\alpha-1}. \tag{A.35}$$

For m-WSMs, $\alpha = \frac{2}{J} + 1$ and we obtain

$$\frac{\mu}{\varepsilon_{\mathrm{F}}} = \begin{cases} 1 - \frac{\pi^2}{3J}\left(\frac{T}{T_{\mathrm{F}}}\right)^2 & (T \ll T_{\mathrm{F}}), \\ \frac{1}{2\eta\left(\frac{2}{J}\right)\Gamma\left(2+\frac{2}{J}\right)}\left(\frac{T}{T_{\mathrm{F}}}\right)^{-\frac{2}{J}} & (T \gg T_{\mathrm{F}}). \end{cases} \tag{A.36}$$

Next, consider the temperature dependent Thomas-Fermi wavevector $q_{\rm TF}(T)$. Note that in 3D, $q^2_{\rm TF}(0) = \frac{4\pi e^2}{\kappa} D(\varepsilon_{\rm F})$ and at finite T, $q^2_{\rm TF}(T) = \frac{4\pi e^2}{\kappa} \frac{\partial n}{\partial \mu}$. Thus we have

$$\frac{q^2_{\rm TF}(T)}{q^2_{\rm TF}(0)} = \frac{\partial \varepsilon_{\rm F}}{\partial \mu} = \frac{\Gamma(\alpha)}{(\beta\varepsilon_{\rm F})^{\alpha-1}} \left[F_{\alpha-1}(z) + F_{\alpha-1}(z^{-1})\right]. \tag{A.37}$$

For a given T, the chemical potential (or equivalently fugacity z) is calculated using the density invariance in Eq. (B.52), and then $q_{\rm TF}(T)$ is obtained from the above relation.

At low temperatures, $\mu(T)$ is given by Eq. (A.33), thus

$$\begin{aligned} \frac{q^2_{\rm TF}(T)}{q^2_{\rm TF}(0)} &\approx \frac{\Gamma(\alpha)}{(\beta\varepsilon_{\rm F})^{\alpha-1}} \left[\frac{(\beta\mu)^{\alpha-1}}{\Gamma(\alpha)} \left(1 + \frac{\pi^2}{6} \frac{(\alpha-1)(\alpha-2)}{(\beta\mu)^2}\right) + \cancelto{0}{\left(z^{-1} - \frac{z^{-2}}{2^{\alpha-1}}\right)}\right] \\ &\approx \frac{\mu}{\varepsilon_{\rm F}} + \frac{\pi^2}{6} \frac{(\alpha-1)(\alpha-2)}{(\beta\varepsilon_{\rm F})^2} \approx 1 - \frac{\pi^2}{6}(\alpha-1)\left(\frac{T}{T_{\rm F}}\right)^2. \end{aligned} \tag{A.38}$$

At high temperatures, $\mu(T)$ is given by Eq. (A.35), thus

$$\begin{aligned} \frac{q^2_{\rm TF}(T)}{q^2_{\rm TF}(0)} &\approx \frac{\Gamma(\alpha)}{(\beta\varepsilon_{\rm F})^{\alpha-1}} \left[2\eta(\alpha-1) + \eta(\alpha-3)(\beta\mu)^2\right] \\ &\approx 2\eta(\alpha-1)\Gamma(\alpha)\left(\frac{T}{T_{\rm F}}\right)^{\alpha-1}. \end{aligned} \tag{A.39}$$

For m-WSMs, we find

$$\frac{q_{\rm TF}(T)}{q_{\rm TF}(0)} = \begin{cases} 1 - \frac{\pi^2}{6J}\left(\frac{T}{T_{\rm F}}\right)^2 & (T \ll T_{\rm F}), \\ \sqrt{2\eta\left(\frac{2}{J}\right)\Gamma\left(1+\frac{2}{J}\right)}\left(\frac{T}{T_{\rm F}}\right)^{\frac{1}{J}} & (T \gg T_{\rm F}), \end{cases} \tag{A.40}$$

where $q_{\rm TF}(0) = q_{\rm TF}$ is given by Eq. (A.8).

Figure A.2 shows the temperature dependence of the chemical potential and Thomas-Fermi wavevector in m-WSMs.

A.4 Temperature dependence of dc conductivity in multi-Weyl semimetals

From Eq. (4.10) in the main text, we can easily generalize the conductivity tensor at zero temperature to that at finite temperature. For $f^{(0)}(\varepsilon) = \left[z^{-1}e^{\beta\varepsilon}+1\right]^{-1}$, $S^{(0)}(\varepsilon) = -\frac{\partial f^{(0)}(\varepsilon)}{\partial\varepsilon} = \beta f^{(0)}(\varepsilon)\left(1-f^{(0)}(\varepsilon)\right) = \frac{\beta z^{-1}e^{\beta\varepsilon}}{(z^{-1}e^{\beta\varepsilon}+1)^2}$. Then the conductivity tensor at finite temperature is given by

$$\begin{aligned}\sigma_{ij}(T) &= ge^2\int\frac{d^3k}{(2\pi)^3}\left(-\frac{\partial f^{(0)}(\varepsilon_{\boldsymbol{k}})}{\partial\varepsilon}\right)v^{(i)}_{\boldsymbol{k}}v^{(j)}_{\boldsymbol{k}}\tau^{(j)}_{\boldsymbol{k}}\\ &= ge^2\int_0^\infty dr\int_0^\pi d\theta\int_0^{2\pi}d\phi\frac{k_0^3 r^{\frac{2}{J}}\sin^{\frac{2}{J}-1}\theta}{(2\pi)^3 c_z J}\frac{\beta z^{-1}e^{\beta\varepsilon_0 r}}{(z^{-1}e^{\beta\varepsilon_0 r}+1)^2}v^{(i)}_{\boldsymbol{k}}v^{(j)}_{\boldsymbol{k}}\tau^{(j)}_{\boldsymbol{k}}\\ &= \frac{\sigma_0}{J}\int_0^\infty dr r^{\frac{2}{J}}\int_{-1}^1 d\mu\left(1-\mu^2\right)^{\frac{1}{J}-1}\int_0^{2\pi}\frac{d\phi}{2\pi}\frac{\beta\varepsilon_0 z^{-1}e^{\beta\varepsilon_0 r}}{(z^{-1}e^{\beta\varepsilon_0 r}+1)^2}\tilde{v}^{(i)}_{\boldsymbol{k}}\tilde{v}^{(j)}_{\boldsymbol{k}}\tilde{\tau}^{(j)}_{\boldsymbol{k}}.\end{aligned} \tag{A.41}$$

Thus from Eq. (A.6), we have

$$\sigma_{xx}(T) = \sigma_0\frac{J}{2}\int_0^\infty dr\, r^2\frac{\beta\varepsilon_0 z^{-1}e^{\beta\varepsilon_0 r}}{(z^{-1}e^{\beta\varepsilon_0 r}+1)^2}\int_{-1}^1 d\mu\left(1-\mu^2\right)\tilde{\tau}^{(x)}(\mu), \tag{A.42a}$$

$$\sigma_{zz}(T) = \sigma_0\frac{c_z^2}{J}\int_0^\infty dr\, r^{\frac{2}{J}}\frac{\beta\varepsilon_0 z^{-1}e^{\beta\varepsilon_0 r}}{(z^{-1}e^{\beta\varepsilon_0 r}+1)^2}\int_{-1}^1 d\mu\left(1-\mu^2\right)^{\frac{1}{J}-1}\mu^2\tilde{\tau}^{(z)}(\mu). \tag{A.42b}$$

To derive the asymptotic behaviors of $\sigma_{ii}(T)/\sigma_{ii}(0)$ at low and high temperatures, let us rewrite Eq. (4.10) in the main text, in the following energy integral form:

$$\sigma_{ii}(T) = ge^2 I\int_0^\infty d\varepsilon\left(-\frac{\partial f^{(0)}(\varepsilon)}{\partial\varepsilon}\right)D(\varepsilon)[v^{(i)}(\varepsilon)]^2\tau^{(i)}(\varepsilon,T), \tag{A.43}$$

where I is a factor from the angular integration. Note that the factor I will be canceled by $\sigma_{ii}(0)$ later. Assuming that $\tau^{(i)}(\varepsilon,T)$ can be decomposed as

$$\tau^{(i)}(\varepsilon,T) = \tau^{(i)}(\varepsilon)g^{(i)}\left(\frac{T}{T_{\rm F}}\right), \tag{A.44}$$

where $g^{(i)}\left(\frac{T}{T_{\rm F}}\right)$ is the energy-independent correction term from the screening effect with $g^{(i)}(0) \equiv 1$, we can separate the contributions from the energy averaging over the Fermi distribution and the temperature dependent screening. Suppose $D(\varepsilon) \propto \varepsilon^{\alpha-1}$, $v^{(i)}(\varepsilon) \propto \varepsilon^{\nu}$, and $\tau^{(i)}(\varepsilon) \propto \varepsilon^{\gamma}$. Then we can express $\sigma_{ii}(T)$ as

$$\begin{aligned}\sigma_{ii}(T) &= C\int_0^\infty d\varepsilon\left(-\frac{\partial f^{(0)}(\varepsilon)}{\partial\varepsilon}\right)\varepsilon^{\alpha-1+2\nu+\gamma}g^{(i)}\left(\frac{T}{T_{\rm F}}\right)\\ &= C(k_{\rm B}T)^{\delta}\Gamma(\delta+1)F_{\delta}(z)g\left(\frac{T}{T_{\rm F}}\right),\end{aligned} \tag{A.45}$$

where C is a constant and $\delta \equiv \alpha - 1 + 2\nu + \gamma$. Note that Eq. (A.45) reduces to $\sigma_{ii}(0) = C\varepsilon_{\rm F}^{\delta}$ at zero temperature. Therefore, after eliminating C, we have

$$\frac{\sigma_{ii}(T)}{\sigma_{ii}(0)} = \frac{\Gamma(\delta+1)F_{\delta}(z)}{(\beta\varepsilon_{\rm F})^{\delta}}g^{(i)}\left(\frac{T}{T_{\rm F}}\right). \tag{A.46}$$

For short-range impurities, $g^{(i)}\left(\frac{T}{T_{\rm F}}\right) = 1$. For charged impurities at low temperatures, from the form of the low-temperature correction for the Thomas-Fermi wavevector in Eq. (A.38), we expect

$$g^{(i)}\left(\frac{T}{T_{\rm F}}\right) \approx 1 - A^{(i)}\left(\frac{T}{T_{\rm F}}\right)^2. \tag{A.47}$$

Note that $A^{(i)}$ depends on the screening strength, and in the strong screening limit, from Eq. (A.40) we have $A^{(i)} = \frac{2\pi^2}{3J}$. At high temperatures, however, $\tau^{(i)}(\varepsilon, T)$ cannot be simply decomposed as Eq. (A.44). The energy averaging typically dominates over the screening contribution [155], and the screening correction $g\left(\frac{T}{T_{\rm F}}\right)$ only gives a constant factor without changing the temperature power. Assuming $g^{(i)}\left(\frac{T}{T_{\rm F}}\right) \approx 1$ at high temperatures, then in the low and high temperature limits, we have

$$\frac{\sigma_{ii}(T)}{\sigma_{ii}(0)} = \begin{cases} 1 + \left[\frac{\pi^2}{6}(\delta-\alpha)\delta - A^{(i)}\right]\left(\frac{T}{T_{\rm F}}\right)^2 & (T \ll T_{\rm F}),\\ \Gamma(\delta+1)\eta(\delta)\left(\frac{T}{T_{\rm F}}\right)^{\delta} & (T \gg T_{\rm F}).\end{cases} \tag{A.48}$$

Now, consider m-WSM with $\alpha = \frac{2}{J}+1$. For short-range impurities, $g^{(i)}\left(\frac{T}{T_\mathrm{F}}\right) = 1$, and from the energy dependence of the relaxation time in Eq. (A.21), $\gamma = -\frac{2}{J}$. Thus, we find

$$\frac{\sigma_{xx}(T)}{\sigma_{xx}(0)} = \begin{cases} 1 + \frac{\pi^2}{3}\left(\frac{J-1}{J}\right)\left(\frac{J-4}{J}\right)\left(\frac{T}{T_\mathrm{F}}\right)^2 & (T \ll T_\mathrm{F}), \\ \Gamma(3-\frac{2}{J})\eta(2-\frac{2}{J})\left(\frac{T}{T_\mathrm{F}}\right)^{2-\frac{2}{J}} & (T \gg T_\mathrm{F}), \end{cases} \tag{A.49a}$$

$$\frac{\sigma_{zz}(T)}{\sigma_{zz}(0)} = \begin{cases} 1 - e^{-T_\mathrm{F}/T} & (T \ll T_\mathrm{F}), \\ \frac{1}{2} + \frac{1}{8\eta(\frac{2}{J})\Gamma(\frac{2}{J}+2)}\left(\frac{T}{T_\mathrm{F}}\right)^{-\frac{2+J}{J}} & (T \gg T_\mathrm{F}). \end{cases} \tag{A.49b}$$

For charged impurities in the strong screening limit, from Eq. (A.23), $\tau^{(i)}(\varepsilon) \sim \varepsilon^{-\frac{2}{J}}$ thus $\gamma = -\frac{2}{J}$ at low temperatures, whereas at high temperatures $\tau^{(i)}(\varepsilon) \sim \varepsilon^{-\frac{2}{J}+\frac{4}{J}}$ because thermally induced charge carriers participate in transport giving $\gamma = \frac{2}{J}$. Combining the temperature dependent screening correction with $A^{(i)} = \frac{2\pi^2}{3J}$ at low temperatures, we find

$$\frac{\sigma_{xx}(T)}{\sigma_{xx}(0)} = \begin{cases} 1 + \frac{\pi^2}{3}\left(\frac{J^2-7J+4}{J^2}\right)\left(\frac{T}{T_\mathrm{F}}\right)^2 & (T \ll T_\mathrm{F}), \\ \Gamma(3+\frac{2}{J})\eta(2+\frac{2}{J})\left(\frac{T}{T_\mathrm{F}}\right)^{2+\frac{2}{J}} & (T \gg T_\mathrm{F}), \end{cases} \tag{A.50a}$$

$$\frac{\sigma_{zz}(T)}{\sigma_{zz}(0)} = \begin{cases} 1 - \frac{2\pi^2}{3J}\left(\frac{T}{T_\mathrm{F}}\right)^2 & (T \ll T_\mathrm{F}), \\ \Gamma(1+\frac{4}{J})\eta(\frac{4}{J})\left(\frac{T}{T_\mathrm{F}}\right)^{\frac{4}{J}} & (T \gg T_\mathrm{F}). \end{cases} \tag{A.50b}$$

For charged impurities at arbitrary screening, from the Fermi energy dependence of the relaxation time discussed in Sec. A.2, $\gamma = 4\zeta - \frac{2}{J}$ with $\frac{1}{J} \le \zeta \le 1$ at high temperatures. Thus, we can express the low and high temperature asymp-

totic forms as

$$\frac{\sigma_{xx}(T)}{\sigma_{xx}(0)} = \begin{cases} 1 + C_{xx}\left(\frac{T}{T_{\rm F}}\right)^2 & (T \ll T_{\rm F}), \\ \Gamma\left(3+4\zeta-\frac{2}{J}\right)\zeta\left(2+4\zeta-\frac{2}{J}\right)\left(\frac{T}{T_{\rm F}}\right)^{2+4\zeta-\frac{2}{J}} & (T \gg T_{\rm F}), \end{cases} \tag{A.51a}$$

$$\frac{\sigma_{zz}(T)}{\sigma_{zz}(0)} = \begin{cases} 1 + C_{zz}\left(\frac{T}{T_{\rm F}}\right)^2 & (T \ll T_{\rm F}), \\ \Gamma(1+4\zeta)\eta(4\zeta)\left(\frac{T}{T_{\rm F}}\right)^{4\zeta} & (T \gg T_{\rm F}). \end{cases} \tag{A.51b}$$

As explained in Sec. A.2, ζs in σ_{xx} and σ_{zz} do not need to be the same. Note that $\zeta = \frac{1}{J}$ in Eq. (A.51) gives the same high-temperature exponent corresponding to the strong screening limit in Eq. (A.50), and the temperature dependent conductivity has the high-temperature asymptotic form given by Eq. (A.51) with ζ which varies within $\frac{1}{J} \le \zeta \le 1$ and approaches $\frac{1}{J}$ in the strong screening limit.

Figure A.3 shows the evolution of the low-temperature coefficients C_{xx} and C_{zz} in Eq. (A.51) for charged impurities as a function of the screening strength $g\alpha$. Above a critical $g\alpha$, C_{xx} and C_{zz} become negative, thus the conductivity decreases with temperature, showing a metallic behavior. As $g\alpha$ increases further, the low-temperature coefficients eventually approach $C_{xx} = \frac{\pi^2}{3}\left(\frac{J^2-7J+4}{J^2}\right)$ and $C_{zz} = -\frac{2\pi^2}{3J}$, as obtained in Eq. (A.50). The non-monotonic behavior in the low-temperature coefficients C_{zz} as a function of $g\alpha$ for $J > 1$ originates from the angle-dependent power-law in the relaxation time, similarly as shown in Fig. 3.2 in the main text.

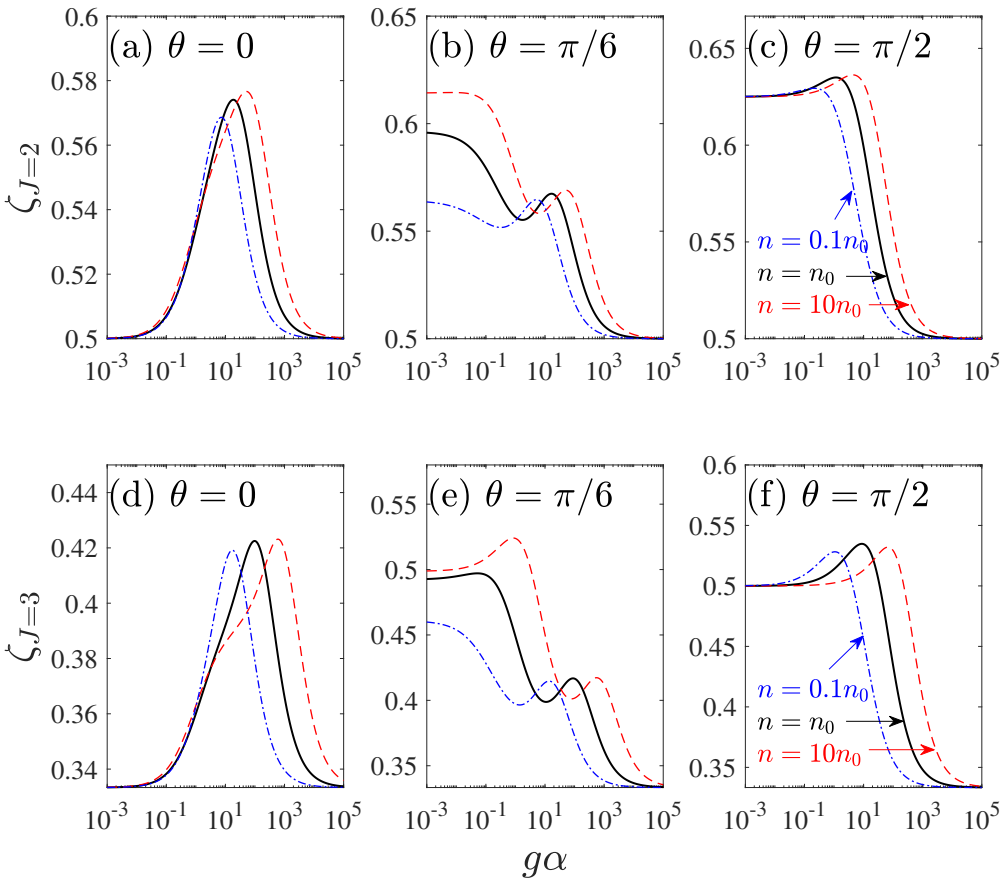

Figure A.1 Angle dependent exponent $\zeta(\theta)$ for (a)-(c) $J = 2$ and (d)-(f) $J = 3$ as a function of the screening strength $g\alpha$ at $\theta = 0, \pi/6, \pi/2$. Blue dashed-dotted, black solid, and red dashed lines represent $n = 0.1n_0, n_0, 10n_0$, respectively.

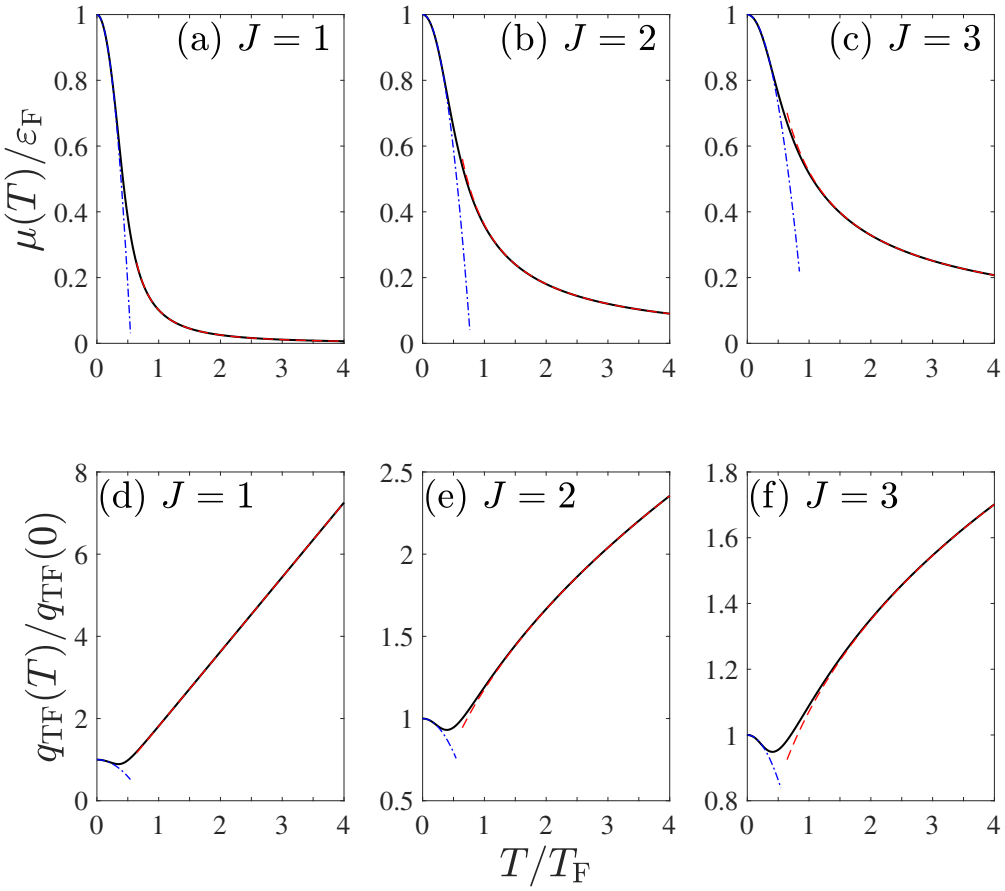

Figure A.2 Temperature dependence of (a)-(c) chemical potential and (d)-(f) Thomas-Fermi wavevector for m-WSMs with $J = 1, 2, 3$. Red dashed and blue dashed-dotted lines represent the asymptotic forms in Eqs. (A.36) and (A.40).

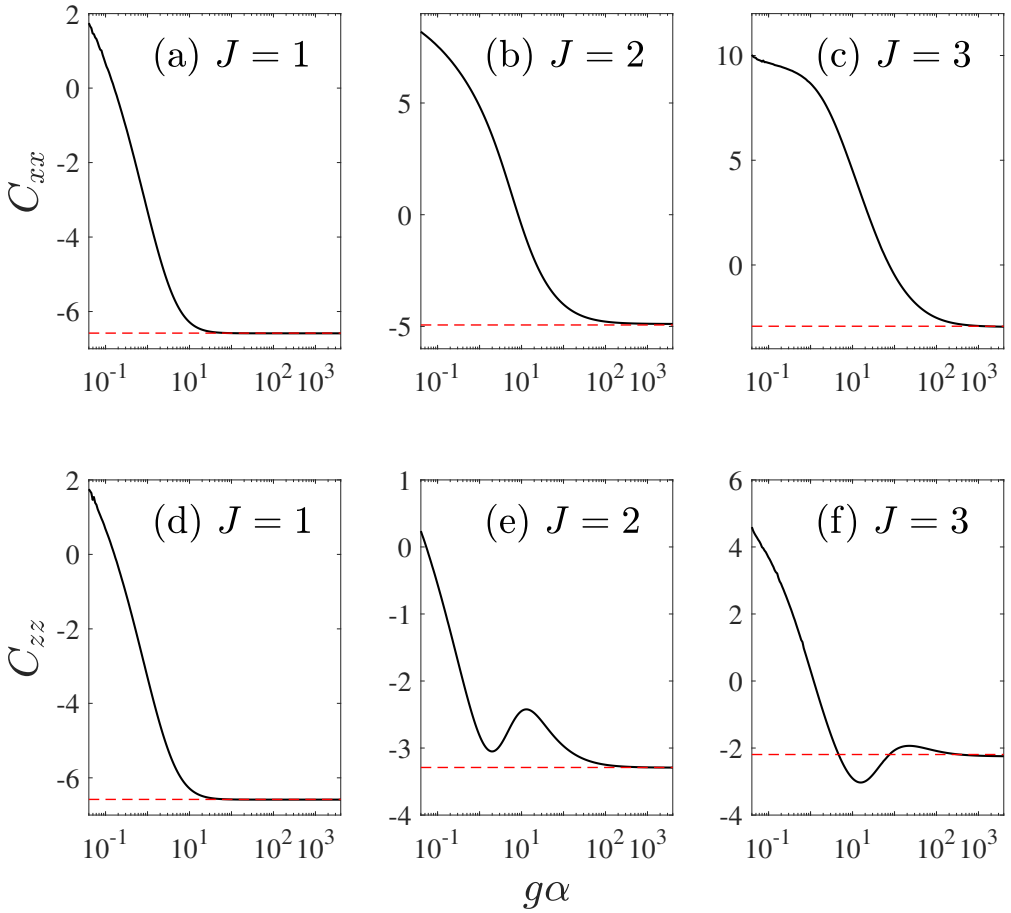

Figure A.3 Low-temperature coefficients (a)-(c) C_{xx} and (d)-(f) C_{zz} as a function of the screening strength $g\alpha$ for charged impurities. Red dashed lines represent the low-temperature coefficients in the strong screening limit given by Eq. (A.50). Here, $n = n_0$ is used for calculation.

Appendix B

Semiclassical Boltzmann transport theory of few-layer black phosphorus in various phases

B.1 Eigenstates and density of states

In this section, we provide a detailed explanation on the model Hamiltonian of few-layer black phosphorus (BP), and its various properties including density of states (DOS). In the model Hamiltonian given by Eq. (4.1) in the main text, the exact values of m^* and v_0 depend on the number of layers and the gap tuning parameter. We introduce the normalization constants $k_0 \equiv a^{-1}$ and $\varepsilon_0 \equiv \frac{\hbar^2 k_0^2}{2m^*}$; thus, the Hamiltonian becomes

$$H = \varepsilon_0 \begin{pmatrix} 0 & \tilde{k}_x^2 - ic\tilde{k}_y + \Delta \\ \tilde{k}_x^2 + ic\tilde{k}_y + \Delta & 0 \end{pmatrix}, \tag{B.1}$$

where $\tilde{\boldsymbol{k}} = \boldsymbol{k}/k_0$, $c = \hbar v_0 k_0/\varepsilon_0$, and $\Delta \equiv \frac{\varepsilon_g}{2\varepsilon_0}$. To avoid difficulties associated with anisotropic dispersion, we consider the following coordinate transformation

with

$$\begin{aligned} k_x &\to \alpha k_0 \left(r\cos\phi - \Delta\right)^{\frac{1}{2}}, \\ k_y &\to \frac{k_0}{c} r \sin\phi, \end{aligned} \tag{B.2}$$

where $\alpha = \pm 1$ represents each half of the Fermi surfaces. This Fermi surface splitting is especially useful for the $\Delta < 0$ case where there are two distinct Fermi surfaces (see Fig. 4.1(f) in the main text), accounting for the "interband" scattering between these two surfaces. The maximum value of ϕ is thus given by

$$\phi_{\max}(r) = \begin{cases} \arccos\left(\frac{\Delta}{r}\right) & (\Delta \neq 0 \text{ and } |\Delta| < r), \\ \pi & (\Delta < 0 \text{ and } |\Delta| \geq r), \\ \frac{\pi}{2} & (\text{otherwise}), \end{cases} \tag{B.3}$$

where $\phi \in [-\phi_{\max}(r), \phi_{\max}(r)]$. This coordinate transformation changes the Hamiltonian into the following form:

$$H = \varepsilon_0 r \begin{pmatrix} 0 & e^{-i\phi} \\ e^{i\phi} & 0 \end{pmatrix}. \tag{B.4}$$

In the transformed coordinates, the energy dispersion is given by $\varepsilon_\pm(r) = \pm\varepsilon_0 r$ and the corresponding eigenstates are given by

$$|+\rangle = \frac{1}{\sqrt{2}} \begin{pmatrix} 1 \\ e^{i\phi} \end{pmatrix}, \tag{B.5a}$$

$$|-\rangle = \frac{1}{\sqrt{2}} \begin{pmatrix} -1 \\ e^{i\phi} \end{pmatrix}. \tag{B.5b}$$

The Jacobian $\mathcal{J}$ corresponding to this transformation is given by

$$\mathcal{J} = \begin{vmatrix} \frac{\partial k_x}{\partial r} & \frac{\partial k_x}{\partial \phi} \\ \frac{\partial k_y}{\partial r} & \frac{\partial k_y}{\partial \phi} \end{vmatrix} = \frac{k_0^2 r}{2c\sqrt{r\cos\phi - \Delta}} \equiv \mathcal{J}(r,\phi). \tag{B.6}$$

Note that, for the + band, the band velocity $v_{\boldsymbol{k}}^{(i)} = \frac{1}{\hbar}\frac{\partial \varepsilon_{+,\boldsymbol{k}}}{\partial k_i}$ can be expressed as

$$v_{\boldsymbol{k}}^{(x)} = 2\alpha v_0 \cos\phi\sqrt{r\cos\phi - \Delta}, \tag{B.7a}$$

$$v_{\boldsymbol{k}}^{(y)} = v_0 c \sin\phi, \tag{B.7b}$$

where $v_0 = \frac{\varepsilon_0}{\hbar k_0}$.

The DOS at the semi-Dirac transition point ($\Delta = 0$) at the energy $\varepsilon > 0$ can be obtained analytically as

$$\begin{aligned} D(\varepsilon) &= g\int \frac{d^2k}{(2\pi)^2}\delta(\varepsilon - \varepsilon_{+,\boldsymbol{k}}) \\ &= 2g\int_0^\infty dr \int_{-\frac{\pi}{2}}^{\frac{\pi}{2}} d\phi \frac{\mathcal{J}(r,\phi)}{(2\pi)^2}\delta(\varepsilon - \varepsilon_0 r) \\ &= \frac{2gk_0^2\sqrt{2}K(1/2)}{\pi^2 c\varepsilon_0}\left(\frac{\varepsilon}{\varepsilon_0}\right)^{\frac{1}{2}}, \end{aligned} \tag{B.8}$$

where g is the spin degeneracy, and the factor 2 originates from the duplicate parts of the Fermi surfaces parameterized by $\alpha = \pm 1$. Here, $K(k) = \sum_{n=0}^{\infty}\left[(2n-1)!!/(2n)!!\right]^2 k^{2n}$ is the complete elliptic integral of the first kind with $K(1/2) \approx 1.854$ [45]. Note that the Thomas–Fermi wave vector is determined by the DOS at the Fermi energy ε_{F} given by

$$q_{\mathrm{TF}} = \frac{2\pi e^2}{\kappa} D(\varepsilon_{\mathrm{F}}) = \frac{4g\alpha_0 k_0\sqrt{2}K(1/2)}{\pi c}\left(\frac{\varepsilon_{\mathrm{F}}}{\varepsilon_0}\right)^{\frac{1}{2}}, \tag{B.9}$$

where $\alpha_0 = \frac{e^2}{\kappa\hbar v_0}$ is the effective fine structure constant.

The carrier density is thus given by

$$n = \int_0^{\varepsilon_{\mathrm{F}}} d\varepsilon D(\varepsilon) = n_0 \frac{4g\sqrt{2}K(1/2)}{3\pi^2 c}\left(\frac{\varepsilon_{\mathrm{F}}}{\varepsilon_0}\right)^{\frac{3}{2}}, \tag{B.10}$$

where $n_0 = k_0^2$. Note that $\varepsilon_{\mathrm{F}} \sim n^{\frac{2}{3}}$ and $D(\varepsilon_{\mathrm{F}}) \sim n^{\frac{1}{3}}$.

Figure 4.2 in the main text shows the calculated DOS and the carrier density for each phase.

B.2 Density dependence of dc conductivity in black phosphorus

In this section, we derive the dc conductivity at zero temperature for 2D multiband systems with anisotropic energy dispersion. To consider the anisotropy of the energy dispersion, we express the multiband anisotropic Boltzmann equation in Eq. (4.7) using the transformed coordinates in Eq. (B.6) as follows:

$$\begin{aligned}
1 &= \sum_{\alpha'} \int_0^\infty dr' \int_{-\phi_{\max}(r')}^{\phi_{\max}(r')} d\phi' \frac{\mathcal{J}(r',\phi')}{(2\pi)^2} W^{\alpha\alpha'}_{\boldsymbol{k}\boldsymbol{k}'} \left(\tau^{(i)}_{\boldsymbol{k}\alpha} - \frac{v^{(i)}_{\boldsymbol{k}'\alpha'}}{v^{(i)}_{\boldsymbol{k}\alpha}} \tau^{(i)}_{\boldsymbol{k}'\alpha'} \right) \\
&= \sum_{\alpha'} \int_0^\infty dr' \int_r' \frac{d\phi'}{(2\pi)^2} \frac{k_0^2 r'}{2c\sqrt{r'\cos\phi' - \Delta}} \\
&\times \left[\frac{2\pi}{\hbar} n_{\rm imp} |V^{\alpha\alpha'}_{\boldsymbol{k}\boldsymbol{k}'}|^2 F^{\alpha\alpha'}_{\boldsymbol{k}\boldsymbol{k}'} \delta(\varepsilon_0 r - \varepsilon_0 r') \right] \left(\tau^{(i)}_{\boldsymbol{k}\alpha} - d^{\alpha\alpha'(i)}_{\boldsymbol{k}\boldsymbol{k}'} \tau^{(i)}_{\boldsymbol{k}'\alpha'} \right) \\
&= \frac{2\pi}{\hbar} n_{\rm imp} \frac{k_0^2}{2\pi c \varepsilon_0} \sum_{\alpha'} \int_r' \frac{d\phi'}{2\pi} \frac{r}{2\sqrt{r\cos\phi' - \Delta}} |V^{\alpha\alpha'}_{\boldsymbol{k}\boldsymbol{k}'}|^2 F^{\alpha\alpha'}_{\boldsymbol{k}\boldsymbol{k}'} \left(\tau^{(i)}_{\boldsymbol{k}\alpha} - d^{\alpha\alpha'(i)}_{\boldsymbol{k}\boldsymbol{k}'} \tau^{(i)}_{\boldsymbol{k}'\alpha'} \right),
\end{aligned} \tag{B.11}$$

where $\alpha = \pm 1$ represents each half of the Fermi surfaces, $d^{\alpha\alpha'(i)}_{\boldsymbol{k}\boldsymbol{k}'} = v^{(i)}_{\boldsymbol{k}'\alpha'}/v^{(i)}_{\boldsymbol{k}\alpha}$, and $F^{\alpha\alpha'}_{\boldsymbol{k}\boldsymbol{k}'} = \frac{1}{2}\left[1 + \cos(\phi - \phi')\right]$ is the square of the wave function overlap between $\boldsymbol{k}$ and $\boldsymbol{k}'$ states in the same conduction (or valence) band. Let us define $\rho_0 = \frac{k_0^2}{2\pi c \varepsilon_0}$, $V_0 = \frac{\varepsilon_0}{k_0^2}$, and $\frac{1}{\tau_0(r)} = \frac{2\pi}{\hbar} n_{\rm imp} V_0^2 \rho_0$, then we have

$$\begin{aligned}
1 = \sum_{\alpha'} \int_r' \frac{d\phi'}{2\pi} \frac{r}{2\sqrt{r\cos\phi' - \Delta}} \\
\times |\tilde{V}^{\alpha\alpha'}_{\boldsymbol{k}\boldsymbol{k}'}|^2 F^{\alpha\alpha'}_{\boldsymbol{k}\boldsymbol{k}'} \left(\tilde{\tau}^{(i)}_{\boldsymbol{k}\alpha} - d^{\alpha\alpha'(i)}_{\boldsymbol{k}\boldsymbol{k}'} \tilde{\tau}^{(i)}_{\boldsymbol{k}'\alpha'} \right),
\end{aligned} \tag{B.12}$$

where $\tilde{V}^{\alpha\alpha'(i)}_{\boldsymbol{k}\boldsymbol{k}'} = V^{\alpha\alpha'(i)}_{\boldsymbol{k}\boldsymbol{k}'}/V_0$ and $\tilde{\tau}^{(i)}_{\boldsymbol{k}\alpha} = \tau^{(i)}_{\boldsymbol{k}\alpha}/\tau_0$. Here, $\int_r' d\phi'$ represents an integration over $-\phi_{\max}(r) < \phi' < \phi_{\max}(r)$. Thus, Eq. (B.12) becomes

$$1 = \sum_{\alpha'} \left[\tilde{w}^{(i)}_{\alpha\alpha'}(\phi) \tilde{\tau}^{(i)}_{\alpha}(\phi) - \int_r' \frac{d\phi'}{2\pi} \tilde{w}^{(i)}_{\alpha\alpha'}(\phi,\phi') \tilde{\tau}^{(i)}_{\alpha'}(\phi') \right], \tag{B.13}$$

where

$$\tilde{w}^{(i)}_{\alpha\alpha'}(\phi) = \int_r' \frac{d\phi'}{2\pi} \frac{r}{2\sqrt{r\cos\phi' - \Delta}} |V^{\alpha\alpha'}_{\boldsymbol{k}\boldsymbol{k}'}|^2 F^{\alpha\alpha'}_{\boldsymbol{k}\boldsymbol{k}'}, \tag{B.14a}$$

$$\tilde{w}^{(i)}_{\alpha\alpha'}(\phi,\phi') = \frac{r}{2\sqrt{r\cos\phi' - \Delta}} |V^{\alpha\alpha'}_{\boldsymbol{k}\boldsymbol{k}'}|^2 F^{\alpha\alpha'}_{\boldsymbol{k}\boldsymbol{k}'} d^{\alpha\alpha'(i)}_{\boldsymbol{k}\boldsymbol{k}'}. \tag{B.14b}$$

Since Eq. (B.13) holds for both $\alpha = \pm 1$, we can rewrite it as

$$\begin{aligned} 1 &= \tilde{w}^{(i)}_{11}(\phi)\tilde{\tau}^{(i)}_1(\phi) - \int_r' \frac{d\phi'}{2\pi} \tilde{w}^{(i)}_{11}(\phi,\phi')\tilde{\tau}^{(i)}_1(\phi') \qquad \text{(B.15a)} \\ &+ \tilde{w}^{(i)}_{1-1}(\phi)\tilde{\tau}^{(i)}_1(\phi) - \int_r' \frac{d\phi'}{2\pi} \tilde{w}^{(i)}_{1-1}(\phi,\phi')\tilde{\tau}^{(i)}_{-1}(\phi'), \\ 1 &= \tilde{w}^{(i)}_{-11}(\phi)\tilde{\tau}^{(i)}_{-1}(\phi) - \int_r' \frac{d\phi'}{2\pi} \tilde{w}^{(i)}_{11}(\phi,\phi')\tilde{\tau}^{(i)}_1(\phi') \qquad \text{(B.15b)} \\ &+ \tilde{w}^{(i)}_{-1-1}(\phi)\tilde{\tau}^{(i)}_{-1}(\phi) - \int_r' \frac{d\phi'}{2\pi} \tilde{w}^{(i)}_{-1-1}(\phi,\phi')\tilde{\tau}^{(i)}_{-1}(\phi'). \end{aligned}$$

Now, let us discretize ϕ to ϕ_n ($n = 1, 2, \cdots, N$) with an interval $\Delta\phi = 2\phi_{\max}(r)/N$. Thus, for $\tilde{\tau}^{(i)}_{n\alpha} = \tilde{\tau}^{(i)}_{\alpha}(\phi_n)$, we have

$$\begin{aligned} 1 &= P^{(i)}{}^{n}_{11}\tilde{\tau}^{(i)}_{n1} - \sum_{n'} P^{(i)}{}^{nn'}_{11}\tilde{\tau}^{(i)}_{n'1} \\ &+ P^{(i)}{}^{n}_{1-1}\tilde{\tau}^{(i)}_{n1} - \sum_{n'} P^{(i)}{}^{nn'}_{1-1}\tilde{\tau}^{(i)}_{n'-1}, \qquad \text{(B.16a)} \\ 1 &= P^{(i)}{}^{n}_{-11}\tilde{\tau}^{(i)}_{n-1} - \sum_{n'} P^{(i)}{}^{nn'}_{-11}\tilde{\tau}^{(i)}_{n'1} \\ &+ P^{(i)}{}^{n}_{-1-1}\tilde{\tau}^{(i)}_{n-1} - \sum_{n'} P^{(i)}{}^{nn'}_{-1-1}\tilde{\tau}^{(i)}_{n'-1}, \qquad \text{(B.16b)} \end{aligned}$$

where $P^{(i)}{}^{n}_{\alpha\alpha'} = \tilde{w}^{(i)}_{\alpha\alpha'}(\phi_n)$ is an N-vector and $P^{(i)}{}^{nn'}_{\alpha\alpha'} = \tilde{w}^{(i)}_{\alpha\alpha'}(\phi_n, \phi_{n'})\Delta\phi$ is an $N \times N$ matrix, which correlates the different ϕ-dependent relaxation times for a given (α, α') combination. Note that Eq. (B.16) shares the basic structure with the multiband scattering formula [68, 69] (which accounts for the scattering between each half of the Fermi surface) and the anisotropic scattering formula

[70] (which accounts for the scattering between different ϕ and ϕ' points). Furthermore, Eq. (B.16) is a $2N \times 2N$ matrix equation with two independent basis indices (α, ϕ_n), i.e., index α for each half of the Fermi surfaces and the ϕ-discretization index n.

Thus, the dc conductivity at zero temperature is given by

$$\begin{aligned}
\sigma_{ij} &= ge^2 \sum_\alpha \int \frac{d^2k}{(2\pi)^2} \delta(\varepsilon_{\boldsymbol{k}} - \varepsilon_{\rm F}) v^{(i)}_{\boldsymbol{k}\alpha} v^{(j)}_{\boldsymbol{k}\alpha} \tau^{(j)}_{\boldsymbol{k}\alpha} \\
&= ge^2 \sum_\alpha \int_0^\infty dr \int_r' d\phi \frac{k_0^2 r \delta(\varepsilon_0 r - \varepsilon_{\rm F}) v^{(i)}_{\boldsymbol{k}\alpha} v^{(j)}_{\boldsymbol{k}\alpha} \tau^{(j)}_{\boldsymbol{k}\alpha}}{2(2\pi)^2 c\sqrt{r\cos\phi - \Delta}} \\
&= \sigma_0 \sum_\alpha \int_0^\infty dr \int_r' \frac{d\phi}{2\pi} \frac{r \delta(r - r_{\rm F}) \tilde{v}^{(i)}_{\boldsymbol{k}\alpha} \tilde{v}^{(j)}_{\boldsymbol{k}\alpha} \tilde{\tau}^{(j)}_{\boldsymbol{k}\alpha}}{2\sqrt{r\cos\phi - \Delta}},
\end{aligned} \tag{B.17}$$

where $\sigma_0 = ge^2\rho_0 v_0^2 \tau_0$, $r_{\rm F} = \varepsilon_{\rm F}/\varepsilon_0$ and $\tilde{v}^{(i)}_{\boldsymbol{k}\alpha} = v^{(i)}_{\boldsymbol{k}\alpha}/v_0$. Thus, from Eq. (B.7), we have

$$\frac{\sigma_{xx}}{\sigma_0} = 2\sum_\alpha \int_{r_{\rm F}}' \frac{d\phi}{2\pi} r_{\rm F} \cos^2\phi \sqrt{r_{\rm F}\cos\phi - \Delta} \tilde{\tau}^{(x)}_\alpha(\phi), \tag{B.18a}$$

$$\frac{\sigma_{yy}}{\sigma_0} = c^2 \sum_\alpha \int_{r_{\rm F}}' \frac{d\phi}{2\pi} \frac{r_{\rm F}\sin^2\phi}{2\sqrt{r_{\rm F}\cos\phi - \Delta}} \tilde{\tau}^{(y)}_\alpha(\phi). \tag{B.18b}$$

Note that τ_0, v_0, ρ_0, and σ_0 are the density-independent normalization constants in units of time, velocity, DOS, and conductivity, respectively.

B.3 Low-density approximate models for the insulator phase and Dirac semimetal phase

In this section, we derive the dc conductivity of low-density approximate models for the insulator phase and Dirac semimetal phase. Note that the only anisotropy considered in these models is the anisotropy in the effective mass or velocity with the *same* power-law dependence in momentum.

B.3.1 Insulator phase at low densities

For the insulator phase, as well as the Dirac semimetal phase discussed later, the DOS and carrier density do not follow the simple power-law behavior. Therefore, we utilize approximate models to understand the asymptotic behavior of dc conductivity at low densities. When $|\varepsilon_{\rm F}| > |\varepsilon_g|$ but the carrier density is sufficiently small, the system can be approximated as a two-dimensional electron gas (2DEG). From the series expansion at the minimum point of the conduction band, we have

$$\begin{aligned} \varepsilon(\boldsymbol{k}) &= \varepsilon_0 \left(\frac{k_x}{k_0}\right)^2 + \frac{\varepsilon_0 c^2}{2\Delta}\left(\frac{k_y}{k_0}\right)^2 \\ &\equiv \frac{\hbar^2 k_x^2}{2m_x} + \frac{\hbar^2 k_y^2}{2m_y}, \end{aligned} \tag{B.19}$$

where $m_x = \frac{\hbar^2 k_0^2}{2\varepsilon_0}$ and $m_y = \frac{\Delta \hbar^2 k_0^2}{c^2 \varepsilon_0}$.

For comparison, we first consider a 2DEG with an isotropic energy dispersion given by

$$\varepsilon(\boldsymbol{k}) = \frac{\hbar^2 k^2}{2m}. \tag{B.20}$$

As the system is isotropic, we can readily calculate the conductivity of each case using the Einstein relation

$$\sigma_{\rm iso} = e^2 D(\varepsilon_{\rm F}) \mathcal{D}, \tag{B.21}$$

where $\mathcal{D} = \frac{v_{\rm F}^2 \tau_{\rm F}}{2}$ is the diffusion constant and $D(\varepsilon) = \frac{gm}{2\pi\hbar^2}$ is the DOS for the isotropic 2DEG. The relaxation time at the Fermi energy $\tau_{\rm F}$ is given by

$$\begin{aligned} \frac{1}{\tau_{\rm F}} &= \frac{2\pi n_{\rm imp}}{\hbar} \int \frac{d^2\boldsymbol{k'}}{(2\pi)^2} |V_{\boldsymbol{k}\boldsymbol{k'}}|^2 \delta(\varepsilon - \varepsilon_{\rm F})(1 - \cos\phi') \\ &= \frac{2\pi n_{\rm imp}}{\hbar} \frac{m}{2\pi\hbar^2} \int_0^{2\pi} \frac{d\phi'}{(2\pi)} |V_{\phi'}|^2 (1 - \cos\phi') \\ &\equiv \frac{2\pi n_{\rm imp}}{\hbar} \frac{m}{2\pi\hbar^2} \bar{V}_{\rm i2DEG}^2, \end{aligned} \tag{B.22}$$

where $V_{\phi'}$ is the angle-dependent potential on the Fermi surface and $\bar{V}^2_{\rm i2DEG} \equiv \int_0^{2\pi} \frac{d\phi'}{2\pi} |V_{\phi'}|^2 (1-\cos\phi')$ is the angle-averaged square of the impurity potential.

Therefore, the dc conductivity of the isotropic 2DEG is given by

$$\begin{aligned} \sigma_{\rm iso} &= e^2 \left(\frac{gm}{2\pi\hbar^2}\right) \left(\frac{v_{\rm F}^2}{2}\right) \left(\frac{\hbar}{2\pi n_{\rm imp}} \frac{2\pi\hbar^2}{m\bar{V}^2_{\rm i2DEG}}\right) \\ &= \frac{ge^2\hbar}{2\pi n_{\rm imp}\bar{V}^2_{\rm i2DEG}} \left(\frac{\hbar^2 k_{\rm F}^2}{2m^2}\right) \\ &= \frac{ge^2\hbar\varepsilon_{\rm F}}{2\pi n_{\rm imp} m\bar{V}^2_{\rm i2DEG}}, \end{aligned} \tag{B.23}$$

where $v_{\rm F} = \frac{\hbar k_{\rm F}}{m}$ and $\varepsilon_{\rm F} = \frac{\hbar^2 k_{\rm F}^2}{2m^2}$.

Subsequently, let us consider the Fermi energy dependence of the dc conductivity using the Einstein relation in Eq. (B.21). For short-range impurities, $\bar{V}^2_{\rm i2DEG}$ is a constant independent of $\varepsilon_{\rm F}$; thus, we have

$$\sigma \sim \varepsilon_{\rm F}. \tag{B.24}$$

Here, we used $v_{\rm F}^2 \sim k_{\rm F}^2 \sim \varepsilon_{\rm F}$. For charged impurities in the strong screening limit, $\bar{V}^2_{\rm i2DEG} \sim q_{\rm TF}^{-2} \sim D^{-2}(\varepsilon_{\rm F})$ is also a constant; thus,

$$\sigma \sim \varepsilon_{\rm F}. \tag{B.25}$$

For the anisotropic 2DEG with different effective masses in each direction, we introduce the following coordinate transformation $[(k_x, k_y) \to (k, \phi)]$:

$$\begin{aligned} k_x &\to \sqrt{\frac{m_x}{m}} k\cos\phi, \\ k_y &\to \sqrt{\frac{m_x}{m}} k\sin\phi, \end{aligned} \tag{B.26}$$

which gives the Jacobian $dk_x dk_y = \frac{\sqrt{m_x m_y}}{m} k dk d\phi$. The band velocity $v^{(i)}_{\boldsymbol{k}} = \frac{1}{\hbar}\frac{\partial \varepsilon_{\boldsymbol{k}}}{\partial k_i}$ can be expressed as

$$\begin{aligned} v^{(x)}_{\boldsymbol{k}} &= \frac{\hbar k}{\sqrt{m m_x}} \cos\phi, \\ v^{(y)}_{\boldsymbol{k}} &= \frac{\hbar k}{\sqrt{m m_y}} \sin\phi. \end{aligned} \tag{B.27}$$

Subsequently, the energy dispersion becomes isotropic in the transformed coordinates; thus, the DOS is given by

$$D(\varepsilon) = \frac{g\sqrt{m_x m_y}}{2\pi\hbar^2}. \tag{B.28}$$

The relaxation time of the anisotropic 2DEG for $\boldsymbol{k}$ at the Fermi energy can be obtained by solving the coupled integral equation [Eq. (4.7) in the main text]. For short-range impurities or charged impurities in the strong screening limit, the scattering potential $V_{\boldsymbol{k}\boldsymbol{k}'} = V_0$ is independent of the angle, thus it can be shown that $\tau^{(i)}_{\boldsymbol{k}} = \tau^{(i)}_{\varepsilon_{\boldsymbol{k}}} \equiv \tau^{(i)}$. Then the coupled equation can be simplified as

$$\begin{aligned} \frac{1}{\tau^{(i)}} &= \frac{2\pi n_{\rm imp}}{\hbar}\int \frac{d^2\boldsymbol{k}'}{(2\pi)^2}|V_{\boldsymbol{k}\boldsymbol{k}'}|^2\delta(\varepsilon_{\boldsymbol{k}}-\varepsilon_{\boldsymbol{k}'})\left(1-\frac{v^{(i)}_{\boldsymbol{k}'}}{v^{(i)}_{\boldsymbol{k}}}\right) \\ &= \frac{2\pi n_{\rm imp}}{\hbar}\frac{\sqrt{m_x m_y}}{2\pi\hbar^2}\bar{V}^2_{\rm a2DEG}, \end{aligned} \tag{B.29}$$

where $\bar{V}^2_{\rm a2DEG} \equiv \int_0^{2\pi}\frac{d\phi'}{(2\pi)}|V_0|^2\left(1-\frac{v^{(i)}_{\boldsymbol{k}'}}{v^{(i)}_{\boldsymbol{k}}}\right) = |V_0|^2$ is the angle-averaged square of the impurity potential for the anisotropic 2DEG. Note that $\tau^{(i)}$ is independent of the direction i.

Therefore, the conductivity of the anisotropic 2DEG is given by

$$\begin{aligned} \sigma_{ij} &= ge^2\int\frac{d^2\boldsymbol{k}}{(2\pi)^2}\delta(\varepsilon_{\rm F}-\varepsilon(\boldsymbol{k}))v^{(i)}v^{(j)}\tau^{(j)} \\ &= \frac{ge^2\sqrt{m_x m_y}}{2\pi\hbar^2}\tau_{\rm F}\int_0^{2\pi}\frac{d\phi}{2\pi}v^{(i)}_{\rm F}v^{(j)}_{\rm F}, \end{aligned} \tag{B.30}$$

where $\tau_{\rm F}$ is the relaxation time at the Fermi energy. When the electric field and

the current density are along the x-direction, the conductivity σ_{xx} becomes

$$\begin{aligned}\sigma_{xx} &= \frac{ge^2\sqrt{m_x m_y}}{2\pi\hbar^2}\tau_{\rm F}\int_0^{2\pi}\frac{d\phi}{2\pi}\left[v_{\rm F}^{(x)}\right]^2 \\ &= \frac{ge^2\sqrt{m_x m_y}}{2\pi\hbar^2}\frac{\hbar}{2\pi n_{\rm imp}}\frac{2\pi\hbar^2}{\sqrt{m_x m_y}\bar{V}_{\rm a2DEG}^2} \\ &\quad\times\frac{\hbar^2}{m m_x}\int_0^{2\pi}\frac{d\phi}{2\pi}k_{\rm F}^2\cos^2\phi \\ &= \frac{ge^2\hbar\varepsilon_{\rm F}}{2\pi n_{\rm imp}\bar{V}_{\rm a2DEG}^2 m}\frac{m}{m_x}. \end{aligned} \tag{B.31}$$

Similarly, when the electric field and the current density are along the y-direction, the conductivity σ_{yy} becomes

$$\begin{aligned}\sigma_{yy} &= \frac{ge^2\sqrt{m_x m_y}}{2\pi\hbar^2}\tau_{\rm F}\int_0^{2\pi}\frac{d\phi}{2\pi}\left[v_{\rm F}^{(y)}\right]^2 \\ &= \frac{ge^2\hbar\varepsilon_{\rm F}}{2\pi n_{\rm imp}\bar{V}_{\rm a2DEG}^2 m}\frac{m}{m_y}. \end{aligned} \tag{B.32}$$

Therefore, the dc conductivities for the anisotropic case are modified as

$$\sigma_{xx} = \sigma_{\rm iso}\frac{m}{m_x}, \tag{B.33a}$$

$$\sigma_{yy} = \sigma_{\rm iso}\frac{m}{m_y}. \tag{B.33b}$$

Thus, for short-range impurities or charged-impurities in the strong screening limit, the Fermi energy dependence of the dc conductivities for the anisotropic 2DEG follows that of the isotropic 2DEG given by Eqs. (B.24) and (B.25).

Note that, as the Fermi energy or the carrier density increases, the insulator phase can no longer be approximated by a 2DEG model, and the energy dispersion follows that of the semi-Dirac transition point. Therefore, the power-law dependence eventually follows that of the semi-Dirac transition point.

B.3.2 Dirac semimetal phase at low densities

For the Dirac semimetal phase ($\Delta < 0$), the series expansion at one of the band touching points gives

$$\begin{aligned} H(\boldsymbol{k}) &= \frac{\varepsilon_0}{k_0}\left(2\sqrt{-\Delta}k_x\sigma_x + ck_y\sigma_y\right) \\ &\equiv \hbar\left(v_x k_x\sigma_x + v_y k_y\sigma_y\right), \end{aligned} \tag{B.34}$$

where $v_x = \frac{2\sqrt{-\Delta}\varepsilon_0}{\hbar k_0}$ and $v_y = \frac{c\varepsilon_0}{\hbar k_0}$.

For comparison, we first consider an isotropic 2D Dirac semimetal with the Hamiltonian given by

$$H(\boldsymbol{k}) = \hbar v\left(k_x\sigma_x + k_y\sigma_y\right). \tag{B.35}$$

The DOS is thus given by

$$D(\varepsilon) = \frac{gk}{2\pi\hbar v} = \frac{g\varepsilon}{2\pi\hbar^2 v^2}. \tag{B.36}$$

The relaxation time at the Fermi energy $\tau_{\rm F}$ is given by

$$\begin{aligned} \frac{1}{\tau_{\rm F}} &= \frac{2\pi n_{\rm imp}}{\hbar}\int\frac{d^2\boldsymbol{k}'}{(2\pi)^2}|V_{\boldsymbol{k}\boldsymbol{k}'}|^2 F_{\boldsymbol{k}\boldsymbol{k}'}\delta(\varepsilon-\varepsilon_{\rm F})(1-\cos\phi') \\ &= \frac{2\pi n_{\rm imp}}{\hbar}\frac{k_{\rm F}}{2\pi\hbar v}\int_0^{2\pi}\frac{d\phi'}{2\pi}|V_{\phi'}|^2 F(\phi')(1-\cos\phi') \\ &= \frac{2\pi n_{\rm imp}}{\hbar}\frac{k_{\rm F}}{2\pi\hbar v}\bar{V}_{\rm igp}^2, \end{aligned} \tag{B.37}$$

where $F(\phi') = \frac{1}{2}(1+\cos\phi')$ is the square of the wave function overlap and $\bar{V}_{\rm igp}^2 \equiv \int_0^{2\pi}\frac{d\phi'}{2\pi}|V_{\phi'}|^2 F(\phi')(1-\cos\phi')$ is the angle-averaged square of the impurity potential. Therefore, the dc conductivity of the isotropic Dirac semimetal is given by

$$\begin{aligned} \sigma_{\rm iso} &= e^2\left(\frac{gk_{\rm F}}{2\pi\hbar v}\right)\frac{v^2}{2}\left(\frac{\hbar}{2\pi n_{\rm imp}}\frac{2\pi\hbar v}{k_{\rm F}\bar{V}_{\rm igp}^2}\right) \\ &= \frac{ge^2\hbar v^2}{4\pi n_{\rm imp}\bar{V}_{\rm igp}^2}. \end{aligned} \tag{B.38}$$

Subsequently, let us consider the Fermi energy dependence of the dc conductivity using the Einstein relation in Eq. (B.21). For short-range impurities, $\bar{V}_{\rm igp}^2$ is a constant independent of $\varepsilon_{\rm F}$; thus, we have

$$\sigma \sim \varepsilon_{\rm F}^0, \tag{B.39}$$

whereas for charged impurities in the strong screening limit, $\bar{V}_{\rm igp}^2 \sim q_{\rm TF}^{-2} \sim D^{-2}(\varepsilon_{\rm F}) \sim \varepsilon_{\rm F}^{-2}$; thus,

$$\sigma \sim \varepsilon_{\rm F}^2. \tag{B.40}$$

Note that, even in the weak screening limit, $\bar{V}_{\rm igp}^2 \sim k_{\rm F}^{-2} \sim \varepsilon_{\rm F}^{-2}$, and in general, $\sigma \sim \varepsilon_{\rm F}^2$ for charged impurities.

For the anisotropic Dirac semimetals with different velocities in each direction, we introduce the following coordinate transformation $[(k_x, k_y) \to (k, \phi)]$:

$$\begin{aligned} k_x &\to \frac{v}{v_x} k \cos\phi, \\ k_y &\to \frac{v}{v_y} k \sin\phi, \end{aligned} \tag{B.41}$$

which gives the Jacobian $dk_x dk_y = \frac{v^2}{v_x v_y} k dk d\phi$. The band velocity $v_{\boldsymbol{k}}^{(i)} = \frac{1}{\hbar} \frac{\partial \varepsilon_{\boldsymbol{k}}}{\partial k_i}$ can be expressed as

$$\begin{aligned} v_{\boldsymbol{k}}^{(x)} &= v_x \cos\phi, \\ v_{\boldsymbol{k}}^{(y)} &= v_y \sin\phi. \end{aligned} \tag{B.42}$$

Subsequently, the energy dispersion becomes isotropic in the transformed coordinates; thus, the DOS is given by

$$D(\varepsilon) = \frac{g v k}{2\pi\hbar v_x v_y} = \frac{g\varepsilon}{2\pi\hbar^2 v_x v_y}. \tag{B.43}$$

Similarly, using the same assumptions which were used in Eq. (B.29), for short-range impurities or charged impurities in the strong screening limit, we can

calculate the relaxation time of the anisotropic Dirac semimetals given by

$$\begin{aligned}\frac{1}{\tau^{(i)}} &= \frac{2\pi n_{\rm imp}}{\hbar}\int\frac{d^2\boldsymbol{k'}}{(2\pi)^2}|V_{\boldsymbol{k}\boldsymbol{k'}}|^2F_{\boldsymbol{k}\boldsymbol{k'}}\delta(\varepsilon_{\boldsymbol{k}}-\varepsilon_{\boldsymbol{k'}})\left(1-\frac{v^{(i)}_{\boldsymbol{k'}}}{v^{(i)}_{\boldsymbol{k}}}\right)\\ &= \frac{2\pi n_{\rm imp}}{\hbar}\frac{gvk}{2\pi\hbar v_x v_y}\bar{V}^2_{\rm agp},\end{aligned} \tag{B.44}$$

where $\bar{V}^2_{\rm agp}\equiv\int_0^{2\pi}\frac{d\phi'}{(2\pi)}|V_0|^2F(\phi')\left(1-\frac{v^{(i)}_{\boldsymbol{k'}}}{v^{(i)}_{\boldsymbol{k}}}\right)=\frac{|V_0|^2}{4}$ is the angle-averaged square of the impurity potential for the anisotropic graphene. Note that $\tau^{(i)}$ for the anisotropic Dirac semimetal is also independent of the direction i.

Therefore, the conductivity of the anisotropic Dirac semimetal is given by

$$\begin{aligned}\sigma_{ij} &= ge^2\int\frac{d^2\boldsymbol{k}}{(2\pi)^2}\delta(\varepsilon_{\rm F}-\varepsilon(\boldsymbol{k}))v^{(i)}v^{(j)}\tau^{(j)}\\ &= \frac{ge^2vk}{2\pi\hbar v_x v_y}\tau_{\rm F}\int_0^{2\pi}\frac{d\phi}{2\pi}v^{(i)}_{\rm F}v^{(j)}_{\rm F}.\end{aligned} \tag{B.45}$$

When the electric field and the current density are along the x-direction, the conductivity σ_{xx} becomes

$$\begin{aligned}\sigma_{xx} &= \frac{ge^2vk}{2\pi\hbar v_x v_y}\tau_{\rm F}\int_0^{2\pi}\frac{d\phi}{2\pi}\left[v^{(x)}_{\rm F}\right]^2\\ &= \frac{ge^2vk}{2\pi\hbar v_x v_y}\frac{\hbar}{2\pi n_{\rm imp}}\frac{2\pi\hbar v_x v_y}{vk\bar{V}^2_{\rm agp}}v_x^2\int_0^{2\pi}\frac{d\phi}{2\pi}\cos^2\phi\\ &= \frac{ge^2\hbar v^2}{4\pi n_{\rm imp}\bar{V}^2_{\rm agp}}\frac{v_x^2}{v^2}.\end{aligned} \tag{B.46}$$

Similarly, when the electric field and the current density are along the y-direction, the conductivity σ_{yy} becomes

$$\begin{aligned}\sigma_{yy} &= \frac{ge^2vk}{2\pi\hbar v_x v_y}\tau_{\rm F}\int_0^{2\pi}\frac{d\phi}{2\pi}\left[v^{(y)}_{\rm F}\right]^2\\ &= \frac{ge^2\hbar v^2}{4\pi n_{\rm imp}\bar{V}^2_{\rm agp}}\frac{v_y^2}{v^2}.\end{aligned} \tag{B.47}$$

Therefore, the dc conductivities for the anisotropic case are modified as

$$\sigma_{xx} = \sigma_{\rm iso}\frac{v_x^2}{v^2}, \tag{B.48a}$$

$$\sigma_{yy} = \sigma_{\rm iso}\frac{v_y^2}{v^2}. \tag{B.48b}$$

Thus, for short-range impurities or charged-impurities in the strong screening limit, the Fermi energy dependence of the dc conductivities for the anisotropic graphene follows that of the isotropic graphene given by Eqs. (B.39) and (B.40).

Near the van Hove singularities, where the energy dispersion can be expanded as $\varepsilon(\boldsymbol{k})/\varepsilon_0 \approx |\Delta| - \tilde{k}_x^2 + \frac{c^2\tilde{k}_y^2}{2|\Delta|}$, the DOS diverges logarithmically [67], dominating the overall power-law behavior of the conductivity. Therefore, for short-range impurities, the conductivity becomes

$$\sigma_{xx} \sim [-\log(|\Delta| - \varepsilon_{\mathrm{F}})]^{-1}, \tag{B.49a}$$

$$\sigma_{yy} \sim [-\log(|\Delta| - \varepsilon_{\mathrm{F}})]^{-1}. \tag{B.49b}$$

For the charged impurities near the van Hove singularities, the conductivity becomes

$$\sigma_{xx} \sim [\log(|\Delta| - \varepsilon_{\mathrm{F}})]^{2}, \tag{B.50a}$$

$$\sigma_{yy} \sim [\log(|\Delta| - \varepsilon_{\mathrm{F}})]^{2}. \tag{B.50b}$$

Note that, as the Fermi energy or the carrier density increases, the power-law dependence of the dc conductivity follows that of the semi-Dirac transition point, as in the gapped insulator case.

B.4 Temperature dependence of chemical potential and Thomas–Fermi wave vector in black phosphorus

In this section, we derive the temperature-dependent chemical potential and Thomas–Fermi wave vector of few-layer BP. When the temperature is finite, the chemical potential μ deviates from the Fermi energy ε_{F} due to the broadening of the Fermi distribution function $f^{(0)}(\varepsilon,\mu) = \left[e^{\beta(\varepsilon-\mu)}+1\right]^{-1}$ where $\beta = \frac{1}{k_{\mathrm{B}}T}$. As the charge carrier density n does not vary under the temperature change,

we have

$$\begin{aligned} n &= \int_{-\infty}^{\infty} d\varepsilon D(\varepsilon) f^{(0)}(\varepsilon, \mu) \\ &= \int_{0}^{\infty} d\varepsilon D(\varepsilon) \left[f^{(0)}(\varepsilon, \mu) + f^{(0)}(-\varepsilon, \mu) \right] \\ &\equiv \int_{-\infty}^{\varepsilon_{\mathrm{F}}} d\varepsilon D(\varepsilon). \end{aligned} \tag{B.51}$$

Thus, the carrier density measured from the charge neutral point, $\Delta n \equiv n|_{\mu} - n|_{\mu=0}$, is given by

$$\begin{aligned} \Delta n &= \int_{0}^{\infty} d\varepsilon D(\varepsilon) \left[f^{(0)}(\varepsilon, \mu) - f^{(0)}(\varepsilon, -\mu) \right] \\ &\equiv \int_{0}^{\varepsilon_{\mathrm{F}}} d\varepsilon D(\varepsilon), \end{aligned} \tag{B.52}$$

where the first and second lines represent the carrier density evaluated at the finite and zero temperatures, respectively. Here, we used $f(-\varepsilon, \mu) = 1 - f(\varepsilon, -\mu)$. By solving this equality in terms of μ, we can calculate the chemical potential of the system for a given temperature T. See the Supplemental Material in [70] for the simplified cases.

Subsequently, consider the temperature-dependent Thomas–Fermi wave vector $q_{\mathrm{TF}}(T)$. Note that, in 3D, $q_{\mathrm{TF}}(0) = \frac{2\pi e^2}{\kappa} D(\varepsilon_{\mathrm{F}})$ and at finite T, $q_{\mathrm{TF}}(T) = \frac{2\pi e^2}{\kappa} \frac{\partial n}{\partial \mu}$. Thus, we have

$$\begin{aligned} \frac{q_{\mathrm{TF}}(T)}{q_{\mathrm{TF}}(0)} &= \frac{\beta}{2D(\varepsilon_{\mathrm{F}})} \int_{0}^{\infty} d\varepsilon D(\varepsilon) \\ &\times \left[\frac{1}{1 + \cosh \beta(\varepsilon - \mu)} + \frac{1}{1 + \cosh \beta(\varepsilon + \mu)} \right]. \end{aligned} \tag{B.53}$$

For a given T, the chemical potential is calculated using the density invariance in Eq. (B.52), and subsequently, $q_{\mathrm{TF}}(T)$ is obtained from the above relation.

When the DOS is given by a simple power law with respect to energy, we can analytically obtain the temperature dependence of the chemical potential

and Thomas–Fermi wave vector, and their asymptotic behaviors at low and high temperatures.

Consider a gapless electron–hole system with a DOS given by $D(\varepsilon) = C_\alpha |\varepsilon|^{\alpha-1}\Theta(\varepsilon)$, where C_α is a constant and $\Theta(\varepsilon)$ is a step function. Using the results from the Supplemental Materials in Ref. [70], we can obtain

$$\frac{\mu}{\varepsilon_{\rm F}} = \begin{cases} 1 - \frac{\pi^2}{12}\left(\frac{T}{T_{\rm F}}\right)^2 & (T \ll T_{\rm F}), \\ \frac{1}{2\eta(\alpha-1)\Gamma(\alpha+1)}\left(\frac{T_{\rm F}}{T}\right)^{\alpha-1} & (T \gg T_{\rm F}), \end{cases} \tag{B.54}$$

where $T_{\rm F} = \varepsilon_{\rm F}/k_{\rm B}$ is the Fermi temperature, η is the Dirichlet eta function, and Γ is the gamma function [45]. For the temperature-dependent Thomas–Fermi wave vector $q_{\rm TF}(T)$, we obtain

$$\frac{q_{\rm TF}(T)}{q_{\rm TF}(0)} = \begin{cases} 1 - \frac{\pi^2}{6}(\alpha-1)\left(\frac{T}{T_{\rm F}}\right)^2 & (T \ll T_{\rm F}), \\ 2\eta(\alpha-1)\Gamma(\alpha)\left(\frac{T}{T_{\rm F}}\right)^{\alpha-1} & (T \gg T_{\rm F}), \end{cases} \tag{B.55}$$

For few-layer BP at the semi-Dirac transition point, the DOS is given by $D(\varepsilon) \propto \varepsilon^{\frac{1}{2}}$; thus, $\alpha = \frac{3}{2}$. Thus, we have

$$\frac{\mu}{\varepsilon_{\rm F}} = \begin{cases} 1 - \frac{\pi^2}{12}\left(\frac{T}{T_{\rm F}}\right)^2 & (T \ll T_{\rm F}), \\ \frac{1}{2\eta\left(\frac{1}{2}\right)\Gamma\left(\frac{5}{2}\right)}\left(\frac{T}{T_{\rm F}}\right)^{\frac{1}{2}} & (T \gg T_{\rm F}), \end{cases} \tag{B.56}$$

and

$$\frac{q_{\rm TF}(T)}{q_{\rm TF}(0)} = \begin{cases} 1 - \frac{\pi^2}{12}\left(\frac{T}{T_{\rm F}}\right)^2 & (T \ll T_{\rm F}), \\ 2\eta\left(\frac{1}{2}\right)\Gamma\left(\frac{3}{2}\right)\left(\frac{T}{T_{\rm F}}\right)^{\frac{1}{2}} & (T \gg T_{\rm F}), \end{cases} \tag{B.57}$$

where $q_{\rm TF}(0) = q_{\rm TF}$ is given by Eq. (A.8).

Figure B.1, Figure B.2, and Figure B.3 show the calculated temperature dependence of the chemical potential $\mu(T)$ and Thomas–Fermi wave vector $q_{\rm TF}(T)$ in various phases of BP using Eqs. (B.52) and (B.53), respectively.

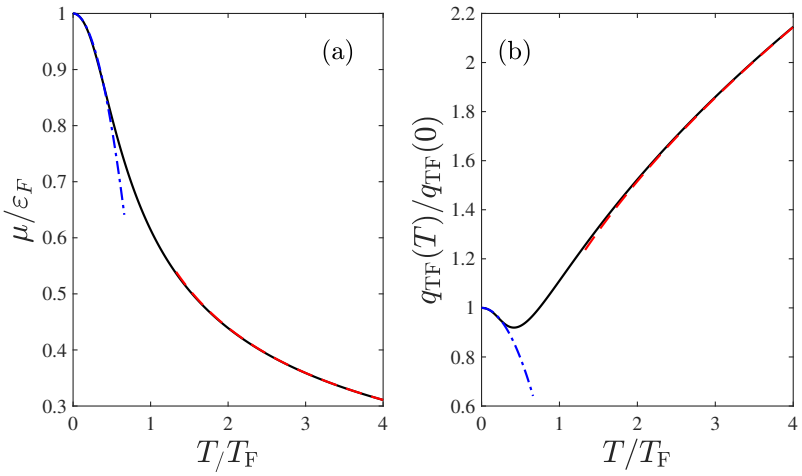

Figure B.1 Calculated temperature dependence of (a) chemical potential and (b) Thomas–Fermi wave vector for the semi-Dirac transition point ($\Delta = 0$). Here, the black solid lines represent the numerical result, and the red/blue dashed lines represent the high-/low-temperature asymptotic forms in Eqs. (B.56) and (B.57). If the chemical potential and temperature are normalized by $\varepsilon_{\rm F}$ and $T_{\rm F}$, respectively, the result is independent of $\varepsilon_{\rm F}$ at the semi-Dirac transition point.

B.5 Temperature dependence of dc conductivity at the semi-Dirac transition point

Using Eq. (4.10) in the main text, we can generalize the conductivity tensor at zero temperature to that at finite temperature. For $f^{(0)}(\varepsilon) = \left[z^{-1}e^{\beta\varepsilon} + 1\right]^{-1}$, where $z = e^{\mu}$ is the fugacity, $S^{(0)}(\varepsilon) = -\frac{\partial f^{(0)}(\varepsilon)}{\partial \varepsilon} = \beta f^{(0)}(\varepsilon)\left[1 - f^{(0)}(\varepsilon)\right] = \frac{\beta z^{-1}e^{\beta\varepsilon}}{(z^{-1}e^{\beta\varepsilon}+1)^2}$. Thus, the conductivity at finite temperature is given by

$$\begin{aligned}
\sigma_{ij}(T) &= ge^2 \sum_\alpha \int \frac{d^2k}{(2\pi)^2} \left(-\frac{\partial f^{(0)}(\varepsilon_{\boldsymbol{k}})}{\partial \varepsilon} \right) v^{(i)}_{\boldsymbol{k}\alpha} v^{(j)}_{\boldsymbol{k}\alpha} \tau^{(j)}_{\boldsymbol{k}\alpha} \\
&= ge^2 \sum_\alpha \int_0^\infty dr \int_r' d\phi \frac{k_0^2 r}{2c\sqrt{r\cos\phi - \Delta}} \frac{\beta z^{-1} e^{\beta\varepsilon_0 r}}{(z^{-1}e^{\beta\varepsilon_0 r}+1)^2} v^{(i)}_{\boldsymbol{k}\alpha} v^{(j)}_{\boldsymbol{k}\alpha} \tau^{(j)}_{\boldsymbol{k}\alpha} \\
&= \sigma_0 \sum_\alpha \int_0^\infty dr \int_r' \frac{d\phi}{2\pi} \frac{r}{2\sqrt{r\cos\phi - \Delta}} \frac{\beta\varepsilon_0 z^{-1} e^{\beta\varepsilon_0 r}}{(z^{-1}e^{\beta\varepsilon_0 r}+1)^2} \tilde{v}^{(i)}_{\boldsymbol{k}\alpha} \tilde{v}^{(j)}_{\boldsymbol{k}\alpha} \tilde{\tau}^{(j)}_{\boldsymbol{k}\alpha}.
\end{aligned} \tag{B.58}$$

Thus, from Eq. (B.7), we have

$$\sigma_{xx}(T) = 2\sigma_0 \sum_\alpha \int_0^\infty dr \, \frac{\beta\varepsilon_0 z^{-1} e^{\beta\varepsilon_0 r}}{(z^{-1}e^{\beta\varepsilon_0 r}+1)^2} \int_r' \frac{d\phi}{2\pi} r\cos^2\phi \sqrt{r\cos\phi - \Delta} \tilde{\tau_\alpha}^{(x)}(\phi), \tag{B.59a}$$

$$\sigma_{yy}(T) = c^2\sigma_0 \sum_\alpha \int_0^\infty dr \, \frac{\beta\varepsilon_0 z^{-1} e^{\beta\varepsilon_0 r}}{(z^{-1}e^{\beta\varepsilon_0 r}+1)^2} \int_r' \frac{d\phi}{2\pi} \frac{r\sin^2\phi}{2\sqrt{r\cos\phi - \Delta}} \tilde{\tau}^{(y)}_\alpha(\phi). \tag{B.59b}$$

To derive the asymptotic behaviors of $\sigma_{ii}(T)$ at low and high temperatures, assume that the relaxation time can be decomposed into energy- and temperature-dependent parts as $\tau^{(i)}(\varepsilon, T) = \tau^{(i)}(\varepsilon) g^{(i)}\left(\frac{T}{T_\mathrm{F}}\right)$ where $g^{(i)}\left(\frac{T}{T_\mathrm{F}}\right)$ is the energy-independent correction term from the temperature-dependent screening effect with $g^{(i)}(0) = 1$. For short-range impurities, $g^{(i)}\left(\frac{T}{T_\mathrm{F}}\right) = 1$. For charged Coulomb impurities, we expect $g\left(\frac{T}{T_\mathrm{F}}\right) \approx 1 - A^{(i)}\left(\frac{T}{T_\mathrm{F}}\right)^2$ at low temperatures, whereas at high temperatures, the energy averaging typically dominates over the screening contribution and we can assume $g\left(\frac{T}{T_\mathrm{F}}\right) \approx 1$. Suppose the following power-law dependence: $D(\varepsilon) \sim \varepsilon^{\alpha-1}$, $v^{(i)}(\varepsilon) \sim \varepsilon^\nu$, and $\tau^{(i)}(\varepsilon) \sim \varepsilon^\gamma$. Subsequently, by rewriting Eq. (B.58) as an energy-integral form, we obtain the asymptotic power-law behavior of the temperature-dependent conductivity at

low and high temperatures as

$$\frac{\sigma_{ii}(T)}{\sigma_{ii}(0)} = \begin{cases} 1+\left[\frac{\pi^2}{6}(\delta-\alpha)\delta - A^{(i)}\right]\left(\frac{T}{T_\mathrm{F}}\right)^2 & (T \ll T_\mathrm{F}), \\ \Gamma(\delta+1)\eta(\delta)\left(\frac{T}{T_\mathrm{F}}\right)^\delta & (T \gg T_\mathrm{F}), \end{cases} \tag{B.60}$$

where $\delta = \alpha - 1 + 2\nu + \gamma$. (See the Supplemental Material of Ref. [70] for the detailed derivation of the power-law analysis of the temperature-dependent dc conductivity.) For the semi-Dirac transition point ($\Delta = 0$), $\alpha = \frac{3}{2}$.

For short-range impurities, $g\left(\frac{T}{T_\mathrm{F}}\right) = 1$ and from the energy dependence of the relaxation time, $\gamma = -\frac{1}{2}$. Thus, from Eq. (B.59), the asymptotic behavior is given by

$$\frac{\sigma_{xx}(T)}{\sigma_{xx}(0)} = \begin{cases} 1-\frac{\pi^2}{12}\left(\frac{T}{T_\mathrm{F}}\right)^2 & (T \ll T_\mathrm{F}), \\ \log 2\left(\frac{T}{T_\mathrm{F}}\right) & (T \gg T_\mathrm{F}), \end{cases} \tag{B.61a}$$

$$\frac{\sigma_{yy}(T)}{\sigma_{yy}(0)} = \begin{cases} 1-e^{-T_\mathrm{F}/T} & (T \ll T_\mathrm{F}), \\ \frac{1}{2}+\frac{1}{8\eta\left(\frac{1}{2}\right)\Gamma\left(\frac{5}{2}\right)}\left(\frac{T}{T_\mathrm{F}}\right)^{-\frac{3}{2}} & (T \gg T_\mathrm{F}). \end{cases} \tag{B.61b}$$

Here, the extra terms in $\sigma_{yy}(T)/\sigma_{yy}(0)$ were obtained through the next-order expansion of the temperature corrections.

For charged impurities in the strong screening limit, $A^{(i)} = \frac{\pi^2}{6}$, which is two times the low-temperature coefficient $\frac{\pi^2}{12}$ in Eq. (B.57), and $\gamma = \frac{1}{2}$. Thus, we obtain

$$\frac{\sigma_{xx}(T)}{\sigma_{xx}(0)} = \begin{cases} 1 & (T \ll T_\mathrm{F}), \\ \frac{\pi^2}{6}\left(\frac{T}{T_\mathrm{F}}\right)^2 & (T \gg T_\mathrm{F}), \end{cases} \tag{B.62a}$$

$$\frac{\sigma_{yy}(T)}{\sigma_{yy}(0)} = \begin{cases} 1-\frac{\pi^2}{4}\left(\frac{T}{T_\mathrm{F}}\right)^2 & (T \ll T_\mathrm{F}), \\ \log 2\left(\frac{T}{T_\mathrm{F}}\right) & (T \gg T_\mathrm{F}). \end{cases} \tag{B.62b}$$

As the screening strength decreases, the low-temperature coefficient in Eq. (B.60) increases, because the screening coefficient $A^{(i)}$ decreases whereas the other part remains positive.

B.6 Temperature dependence of dc conductivity in the low-density approximate models for the insulator phase and Dirac semimetal phase

In this section, we present the temperature dependence of the chemical potential, Thomas–Fermi wave vector, and conductivity of the low-density approximate models for the insulator phase and Dirac semimetal phase, which are the gapped 2DEG and graphene, respectively.

B.6.1 Insulator phase

We introduce the gapped 2DEG model system with the energy dispersion given by $\varepsilon(\boldsymbol{k}) = \pm\varepsilon_0 \left[\Delta + (k/k_0)^2\right]$ with $\Delta > 0$, to account for the thermal excitation behavior involving the band gap between the valence and conduction bands, similar to the insulator phase. Note that the effects of the difference between the effective mass of each direction are canceled out by zero-temperature normalization.

Figure B.4 shows the calculated dc conductivities as a function of the temperature for the gapped 2DEG system in the low-density limit with $\varepsilon_{\mathrm{F}} = 1.1\varepsilon_0$ along with the result of the insulator phase with the same Fermi energy (see also Fig. 4.8 in the main text). At low temperatures, the calculated results of temperature-dependent conductivity in the insulator phase show a similar behavior as that of the low-density approximate model. However, as the temperature increases, the discrepancy between the two results increases, and in

the high-temperature limit, the conductivity becomes similar to that of the semi-Dirac transition point.

B.6.2 Dirac semimetal Phase

For graphene (which is an approximate model for the Dirac semimetal phase in the low-density limit) from Eqs. (B.54) and (B.55) with $\alpha = 2$, the low– and high–temperature asymptotic behaviors for chemical potential are given by

$$\frac{\mu}{\varepsilon_{\rm F}} = \begin{cases} 1 - \frac{\pi^2}{6}\left(\frac{T}{T_{\rm F}}\right)^2 & (T \ll T_{\rm F}), \\ \frac{1}{4\log 2}\left(\frac{T}{T_{\rm F}}\right)^{-1} & (T \gg T_{\rm F}), \end{cases} \tag{B.63}$$

whereas those for the Thomas–Fermi wave vector are given by

$$\frac{q_{\rm TF}(T)}{q_{\rm TF}(0)} = \begin{cases} 1 - \frac{\pi^2}{6}\left(\frac{T}{T_{\rm F}}\right)^2 & (T \ll T_{\rm F}), \\ 2\log 2\left(\frac{T}{T_{\rm F}}\right) & (T \gg T_{\rm F}). \end{cases} \tag{B.64}$$

As shown in Figs. B.3(a) and B.3(d), the result of the low-density approximate model and the numerically calculated result of the Dirac semimetal phase in the low-density limit are consistent with each other. For short-range impurities, the asymptotic form of the temperature-dependent conductivity becomes [Eq. (B.61) with $\gamma = 0$]

$$\frac{\sigma_{\rm gp}(T)}{\sigma_{\rm gp}(0)} = \begin{cases} 1 - e^{-T_{\rm F}/T} & (T \ll T_{\rm F}), \\ \frac{1}{2} + \frac{1}{16\log 2}\left(\frac{T}{T_{\rm F}}\right)^{-2} & (T \gg T_{\rm F}), \end{cases} \tag{B.65}$$

whereas for charged impurities in the strong screening limit, [Eq. (B.61) with $\gamma = 2$]

$$\frac{\sigma_{\rm gp}(T)}{\sigma_{\rm gp}(0)} = \begin{cases} 1 - \frac{\pi^2}{3}\left(\frac{T}{T_{\rm F}}\right)^2 & (T \ll T_{\rm F}), \\ \frac{\pi^2}{6}\left(\frac{T}{T_{\rm F}}\right)^2 & (T \gg T_{\rm F}). \end{cases} \tag{B.66}$$

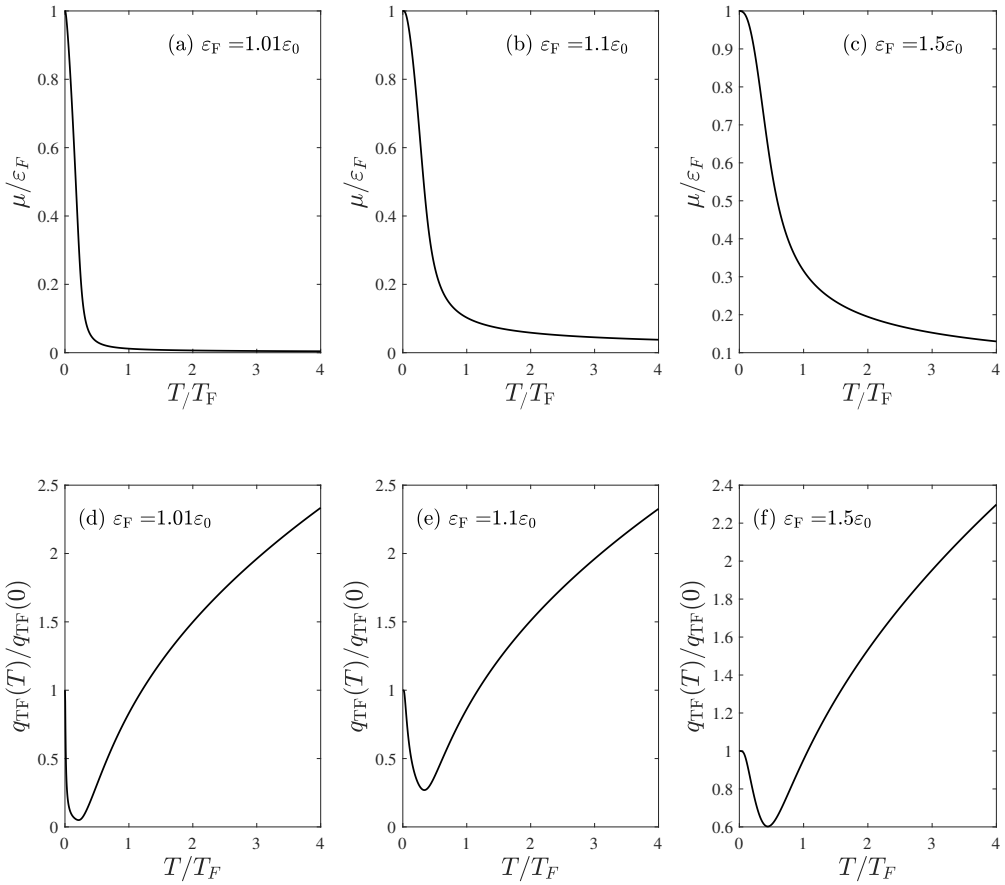

Figure B.2 Calculated temperature dependence of (a)-(c) chemical potential and (d)-(f) Thomas–Fermi wave vector for the gapped insulator phase with $\Delta = 1$ at (a), (d) $\varepsilon_{\rm F} = 1.01\varepsilon_0$, (b), (e) $\varepsilon_{\rm F} = 1.1\varepsilon_0$, and (c), (f) $\varepsilon_{\rm F} = 1.5\varepsilon_0$.

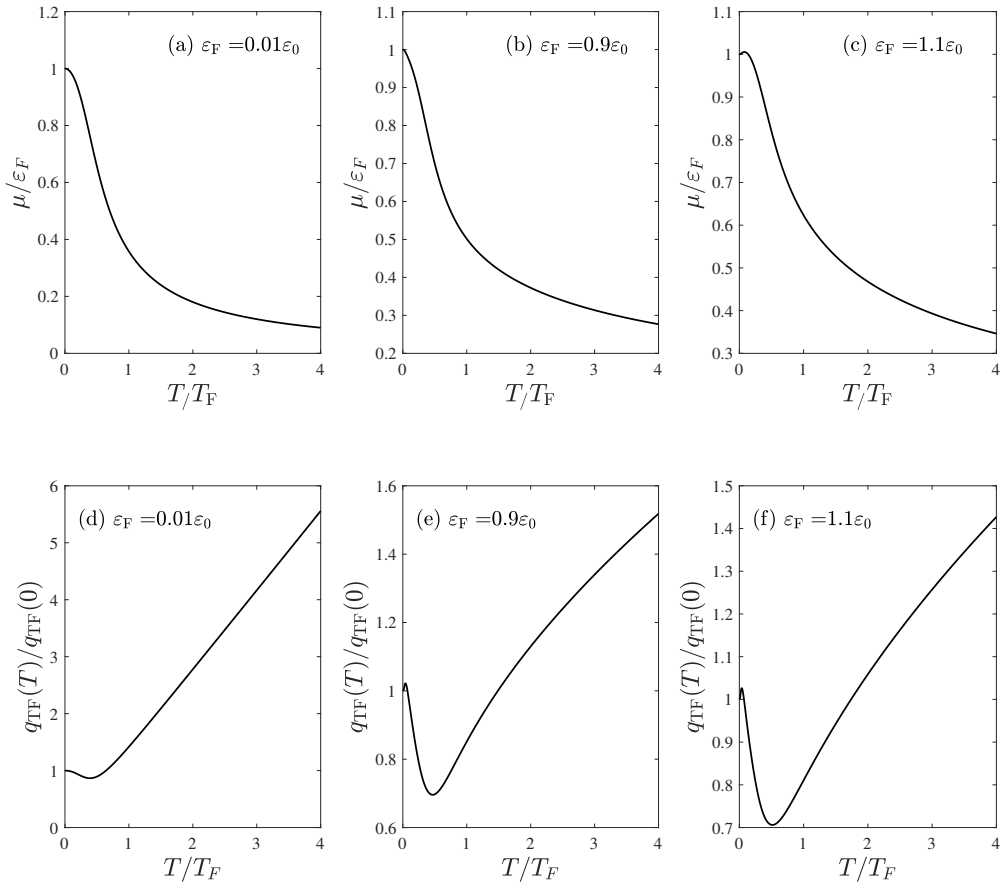

Figure B.3 Calculated temperature dependence of (a)-(c) chemical potential and (d)-(f) Thomas–Fermi wave vector for the Dirac semimetal phase with $\Delta = -1$ at (a), (d) $\varepsilon_{\rm F} = 0.01\varepsilon_0$, (b), (e) $\varepsilon_{\rm F} = 0.9\varepsilon_0$, and (c), (f) $\varepsilon_{\rm F} = 1.1\varepsilon_0$.

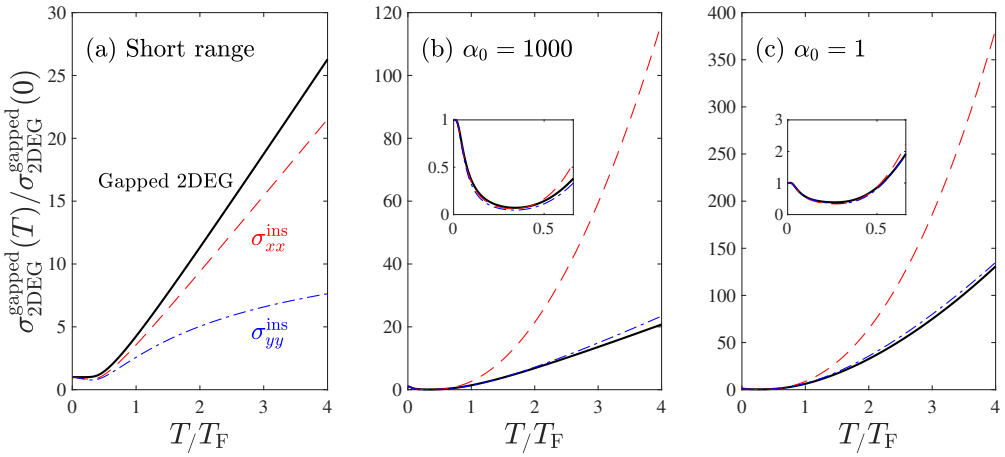

Figure B.4 Calculated dc conductivities as a function of the temperature for the gapped 2DEG system in the low-density limit with $\Delta = 1$ for (a) short-range impurities, (b) charged impurities with $\alpha_0 = 1000$, and (c) charged impurities with $\alpha_0 = 1$. Here, $\varepsilon_{\rm F} = 1.1\varepsilon_0$ is used for the calculation. The red dashed lines and blue dashed-dotted lines represent the conductivity of the insulator phase (with the same Fermi energy) $\sigma_{xx}^{\rm ins}$ and $\sigma_{yy}^{\rm ins}$, respectively.

Appendix C

Magneto-thermoelectric transport equation in anisotropic systems

When we take the thermal gradient into account, on top of $\boldsymbol{E}$ and $\boldsymbol{B}$, the equation of motion $\left(\frac{df}{dt}\right)$ would be modified as

$$\begin{aligned}
&\frac{df}{dt} = \dot{\boldsymbol{k}} \cdot \nabla_{\boldsymbol{k}} f_{\boldsymbol{kr}} + \dot{\boldsymbol{r}} \cdot \nabla_{\boldsymbol{r}} f_{\boldsymbol{kr}} \\
&\approx \hbar \dot{\boldsymbol{k}} \cdot \boldsymbol{v}_{\boldsymbol{k}} \frac{\partial f^{(0)}_{\boldsymbol{kr}}}{\partial \varepsilon_{\boldsymbol{k}}} + \dot{\boldsymbol{k}} \cdot \nabla_{\boldsymbol{k}} g_{\boldsymbol{k}} + \dot{\boldsymbol{r}} \cdot \left[\nabla_{\boldsymbol{r}} \mu \frac{\partial f^{(0)}_{\boldsymbol{kr}}}{\partial \mu} + \nabla_{\boldsymbol{r}} T \frac{\partial f^{(0)}_{\boldsymbol{kr}}}{\partial T} \right] \\
&= \left[-\hbar \dot{\boldsymbol{k}} \cdot \boldsymbol{v}_{\boldsymbol{k}} + \dot{\boldsymbol{r}} \cdot \left(\nabla_{\boldsymbol{r}} \mu + \frac{\varepsilon_{\boldsymbol{k}} - \mu}{T} \nabla_{\boldsymbol{r}} T \right) \right] S^{(0)}(\varepsilon) \\
&+ \dot{\boldsymbol{k}} \cdot \nabla_{\boldsymbol{k}} g_{\boldsymbol{k}},
\end{aligned} \tag{C.1}$$

where T is the temperature, and μ is the chemical potential. As the thermal gradient makes the system inhomogeneous, we can see that the position-dependent terms such as $\nabla_{\boldsymbol{r}} f_{\boldsymbol{kr}}$ were recovered.

Expanding the equation of motion Eq. (C.1), we get

$$
\begin{aligned}
\frac{df}{dt} &= \left[-\hbar\dot{\boldsymbol{k}}\cdot\boldsymbol{v}_{\boldsymbol{k}} + \dot{\boldsymbol{r}}\cdot\left(\nabla_{\boldsymbol{r}}\mu + \frac{\varepsilon_{\boldsymbol{k}}-\mu}{T}\nabla_{\boldsymbol{r}}T\right)\right] S^{(0)}(\varepsilon) + \dot{\boldsymbol{k}}\cdot\nabla_{\boldsymbol{k}}g_{\boldsymbol{k}} \\
&= \frac{S^{(0)}}{D_{\boldsymbol{k}}}\left[-q\boldsymbol{E}\cdot\boldsymbol{v}_{\boldsymbol{k}} + \frac{q^2}{\hbar c}(\boldsymbol{E}\cdot\boldsymbol{B})(\boldsymbol{\Omega}_{\boldsymbol{k}}\cdot\boldsymbol{v}_{\boldsymbol{k}})\right. \\
&\left. + \left(\boldsymbol{v}_{\boldsymbol{k}} - \frac{q}{\hbar}\boldsymbol{E}\times\boldsymbol{\Omega}_{\boldsymbol{k}} - \frac{q}{\hbar c}(\boldsymbol{v}_{\boldsymbol{k}}\cdot\boldsymbol{\Omega}_{\boldsymbol{k}})\boldsymbol{B}\right)\cdot\left(\nabla_{\boldsymbol{r}}\mu + \frac{\varepsilon_{\boldsymbol{k}}-\mu}{T}\nabla_{\boldsymbol{r}}T\right)\right] \\
&+ \frac{q}{\hbar c}\frac{(\boldsymbol{v}_{\boldsymbol{k}}\times\boldsymbol{B})\cdot\nabla_{\boldsymbol{k}}g_{\boldsymbol{k}}}{D_{\boldsymbol{k}}} \\
&= \frac{S^{(0)}}{D_{\boldsymbol{k}}}\left[-q\boldsymbol{\mathcal{E}}\cdot\boldsymbol{v}_{\boldsymbol{k}} + \frac{q^2}{\hbar c}(\boldsymbol{\mathcal{E}}\cdot\boldsymbol{B})(\boldsymbol{\Omega}_{\boldsymbol{k}}\cdot\boldsymbol{v}_{\boldsymbol{k}}) - \frac{q}{\hbar}(\boldsymbol{E}\times\boldsymbol{\Omega}_{\boldsymbol{k}})\cdot\nabla_{\boldsymbol{r}}\mu\right. \\
&+ \frac{\varepsilon_{\boldsymbol{k}}-\mu}{T}\boldsymbol{v}_{\boldsymbol{k}}\cdot\nabla_{\boldsymbol{r}}T - \frac{q}{\hbar}\frac{\varepsilon_{\boldsymbol{k}}-\mu}{T}(\boldsymbol{E}\times\boldsymbol{\Omega}_{\boldsymbol{k}})\cdot\nabla_{\boldsymbol{r}}T \\
&\left. - \frac{q}{\hbar c}\frac{\varepsilon_{\boldsymbol{k}}-\mu}{T}(\boldsymbol{v}_{\boldsymbol{k}}\cdot\boldsymbol{\Omega}_{\boldsymbol{k}})(\boldsymbol{B}\cdot\nabla_{\boldsymbol{r}}T)\right] + \frac{q}{\hbar c}\frac{(\boldsymbol{v}_{\boldsymbol{k}}\times\boldsymbol{B})\cdot\nabla_{\boldsymbol{k}}g_{\boldsymbol{k}}}{D_{\boldsymbol{k}}} \\
&= \frac{S^{(0)}}{D_{\boldsymbol{k}}}\left[\boldsymbol{v}_{\boldsymbol{k}}\cdot\left(-q\boldsymbol{\mathcal{E}} + \frac{\varepsilon_{\boldsymbol{k}}-\mu}{T}\nabla_{\boldsymbol{r}}T\right) - \frac{q}{\hbar}(\boldsymbol{E}\times\boldsymbol{\Omega}_{\boldsymbol{k}})\cdot\left(\nabla_{\boldsymbol{r}}\mu + \frac{\varepsilon_{\boldsymbol{k}}-\mu}{T}\nabla_{\boldsymbol{r}}T\right)\right. \\
&+ \frac{q^2}{\hbar c}(\boldsymbol{\mathcal{E}}\cdot\boldsymbol{B})(\boldsymbol{\Omega}_{\boldsymbol{k}}\cdot\boldsymbol{v}_{\boldsymbol{k}}) \\
&\left. - \frac{q}{\hbar c}\frac{\varepsilon_{\boldsymbol{k}}-\mu}{T}(\boldsymbol{v}_{\boldsymbol{k}}\cdot\boldsymbol{\Omega}_{\boldsymbol{k}})(\boldsymbol{B}\cdot\nabla_{\boldsymbol{r}}T)\right] + \frac{q}{\hbar c}\frac{(\boldsymbol{v}_{\boldsymbol{k}}\times\boldsymbol{B})\cdot\nabla_{\boldsymbol{k}}g_{\boldsymbol{k}}}{D_{\boldsymbol{k}}} \qquad \text{(C.2)} \\
&= -S^{(0)}\dot{\boldsymbol{r}}\cdot\left(q\boldsymbol{\mathcal{E}} + (\varepsilon_{\boldsymbol{k}}-\mu)\frac{-\nabla_{\boldsymbol{r}}T}{T}\right) + \frac{q}{\hbar c}\frac{(\boldsymbol{v}_{\boldsymbol{k}}\times\boldsymbol{B})\cdot\nabla_{\boldsymbol{k}}g_{\boldsymbol{k}}}{D_{\boldsymbol{k}}} \\
&= -S^{(0)}\dot{\boldsymbol{r}}\cdot\left(q\boldsymbol{\mathcal{E}} + (\varepsilon_{\boldsymbol{k}}-\mu)\frac{-\nabla_{\boldsymbol{r}}T}{T}\right) + \frac{q}{\hbar c}(\dot{\boldsymbol{r}}\times\boldsymbol{B})\cdot\nabla_{\boldsymbol{k}}g_{\boldsymbol{k}},
\end{aligned}
$$

where $\boldsymbol{\mathcal{E}} = \boldsymbol{E} - \nabla_{\boldsymbol{r}}\mu/q$, and we have further ignored the higher-order electric field terms for $\dot{\boldsymbol{k}}\cdot\nabla_{\boldsymbol{k}}g_{\boldsymbol{k}}$.

Using the modified ansatz for $g_{\boldsymbol{k}}$,

$$
\begin{aligned}
g_{\boldsymbol{k}} &= \sum_{i=1}^{d}\left[q\mathcal{E}^{(i)}\tau_{\boldsymbol{k}}^{(i)} + (\varepsilon_{\boldsymbol{k}}-\mu)\frac{-\nabla_{\boldsymbol{r}}T}{T}\tau_{\boldsymbol{k}}^{T(i)}\right]\dot{r}_{\boldsymbol{k}}^{(i)}S^{(0)}(\varepsilon) \\
&+ \frac{q}{\hbar c}\sum_{i,j,k}\epsilon_{ijk}\tau_{\boldsymbol{k}}^{(i)}\dot{r}_{\boldsymbol{k}}^{(i)}\frac{\partial g_{\boldsymbol{k}}}{\partial k^{(j)}}B^{(k)}, \qquad \text{(C.3)}
\end{aligned}
$$

where $\tau_{\boldsymbol{k}}^{(i)}$ and $\tau_{\boldsymbol{k}}^{T(i)}$, are the magneto-thermoelectric transport relaxation times.

It turns out that these relaxation times are equivalent for elastic scattering, i.e. $\tau_{\boldsymbol{k}}^{(i)} = \tau_{\boldsymbol{k}}^{T(i)}$. Then we can write

$$g_{\boldsymbol{k}} = \sum_{i=1}^{d} \dot{r}_{\boldsymbol{k}}^{(i)} \tau_{\boldsymbol{k}}^{(i)} G^{(i)}, \tag{C.4}$$

where

$$G^{(i)} = G_0^{(i)} + \frac{q}{\hbar c} \sum_{j,k}^{d} \epsilon_{ijk} \frac{\partial g_{\boldsymbol{k}}}{\partial k^{(j)}} B^{(k)}, \tag{C.5}$$

where $G_0^{(i)} = q \left[\mathcal{E}^{(i)} + (\varepsilon_{\boldsymbol{k}} - \mu) \boldsymbol{t} \right] S^{(0)}(\varepsilon)$, and $\boldsymbol{t} = \frac{-\nabla_{\boldsymbol{r}} T}{qT}$. Introducing the modified version of an inverse mass tensor $\tilde{\mathbb{M}}$, where

$$\tilde{\mathbb{M}}_{ij} = \frac{1}{\hbar} \frac{\partial \dot{r}_{\boldsymbol{k}}^{(j)}}{\partial k_i}, \tag{C.6}$$

then Eq. (5.27) becomes

$$G^{(i)} = G_0^{(i)} + \frac{q}{c} \sum_{j,k}^{d} \epsilon_{ijk} \tilde{\mathbb{M}}_{jl} \frac{\partial g_{\boldsymbol{k}}}{\partial v_{\boldsymbol{k}}^{\mathrm{mod}(l)}} B^{(k)}. \tag{C.7}$$

Again, we solve the Eq. (C.7) recursively (using an assumption that $G^{(i)}$ is independent of $\dot{r}$) to get

$$g_{\boldsymbol{k}} = \sum_{i=1}^{d} \dot{r}_{\boldsymbol{k}}^{(i)} \tau_{\boldsymbol{k}}^{(i)} G^{(i)} = \sum_{i,j=1}^{d} \dot{r}_{\boldsymbol{k}}^{(i)} \tau_{\boldsymbol{k}}^{(i)} \mathbb{N}_{ij} G_0^{(j)}, \tag{C.8}$$

where $\mathbb{N} = \left(\mathbb{1} - \mathbb{F} \frac{\boldsymbol{\mu}}{c} \right)^{-1}$ with its elements changed accordingly, from the definition in the main text.

Rewriting the equation of motion Eq. (C.2) in terms of $g_{\boldsymbol{k}}$, we get

$$\dot{\boldsymbol{k}} \cdot \nabla_{\boldsymbol{k}} f_{\boldsymbol{r},\boldsymbol{k}} + \dot{\boldsymbol{r}} \cdot \nabla_{\boldsymbol{r}} f_{\boldsymbol{r},\boldsymbol{k}} = \sum_{i,j=1}^{d} \dot{r}_{\boldsymbol{k}}^{(i)} \mathbb{N}_{ij} G_0^{(j)}. \tag{C.9}$$

Finally, we arrive at the Boltzmann equaion (assuming $\boldsymbol{G} = \boldsymbol{G}'$)

$$\begin{aligned} \frac{df}{dt} &= \sum_{i,j=1}^{d} \dot{r}_{\boldsymbol{k}}^{(i)} \mathbb{N}_{ij} G_0^{(j)} \\ &= \sum_{i,j=1}^{d} \int \frac{d^d k'}{(2\pi)^d} D_{\boldsymbol{k}'} W_{\boldsymbol{k}'\boldsymbol{k}} \left(\dot{r}_{\boldsymbol{k}}^{(i)} \tau_{\boldsymbol{k}}^{(i)} - \dot{r}_{\boldsymbol{k}'}^{(i)} \tau_{\boldsymbol{k}'}^{(i)} \right) \mathbb{N}_{ij} G_0^{(j)}. \end{aligned} \tag{C.10}$$

Since we are only considering the terms that are linear in $\boldsymbol{E}$, we ignore the terms in $\dot{\boldsymbol{r}}$ and $\mathbb{N}$ that depends on $\boldsymbol{E}$. Then $\dot{\boldsymbol{r}} \to \boldsymbol{v}_{\boldsymbol{k}}^{\mathrm{mod}}$. Carrying out the rest of the equation, we get

$$\int \frac{d^d k'}{(2\pi)^d} D_{\boldsymbol{k}'} W_{\boldsymbol{k}'\boldsymbol{k}} \left(\tau_{\boldsymbol{k}}^{(i)} - \frac{v_{\boldsymbol{k}'}^{\mathrm{mod}(i)}}{v_{\boldsymbol{k}}^{\mathrm{mod}(i)}} \tau_{\boldsymbol{k}'}^{(i)} \right) = 1, \tag{C.11}$$

which is the same form as Eq. (5.38) in the main text.

Appendix D

Diluted magnetic Dirac-Weyl materials: Susceptibility and ferromagnetism in three-dimensional chiral gapless semimetals

D.1 Cutoff dependence of the range function

To derive the asymptotic behavior of Eq. (6.6) at zero temperature, we use the fact that the zero-temperature intrinsic polarization function $\chi(\boldsymbol{q}, T = 0)$ is proportional to the DOS, which is given by

$$\chi(\boldsymbol{q}, T = 0) \propto q^{d-N}, \tag{D.1}$$

where d is the dimension of the system. Then, the range function $\chi(\boldsymbol{r}) \equiv \chi(\boldsymbol{r}, T = 0)$ becomes

$$\chi(\boldsymbol{r}) = C \int_0^{q_c} dq q^{2d-N-1} f_d(qr), \tag{D.2}$$

where C is a momentum- and position-independent constant. Here, $f_d(qr)$ is defined by

$$f_d(qr) = \begin{cases} J_0(qr) & (d=2), \\ j_0(qr) & (d=3), \end{cases} \tag{D.3}$$

where $J_0(x)$ and $j_0(x) = \frac{\sin x}{x}$ are the Bessel and spherical Bessel functions of the first kind, respectively.

First, consider the 3D case. Using the following integral (see Eq. (3.761) in Ref. [161])

$$\int_0^1 dx x^{\mu-1} \sin(ax) = \frac{-i}{2\mu} \left[M(\mu, \mu+1, ia) - \text{c.c.} \right], \tag{D.4}$$

where $a > 0$, $\mathrm{Re}(\mu) > -1$, $\mu \neq 0$, and $M(a,b,z) = {}_1F_1(a;b;z)$ is the Kummer's confluent hypergeometric function, we obtain $\chi(\boldsymbol{r})$ as

$$\chi(\boldsymbol{r}) = \frac{C}{r^{6-N}} \frac{-i(q_c r)^{5-N}}{2(5-N)} \left[M(5-N, 6-N, iq_c r) - \text{c.c.} \right]. \tag{D.5}$$

The asymptotic behavior of $M(a,b,z)$ at a large z is given by (see p. 508 in Ref. [40])

$$M(a,b,z) \approx \Gamma(b) \left[\frac{e^z z^{a-b}}{\Gamma(a)} + \frac{(-z)^{-a}}{\Gamma(b-a)} \right]. \tag{D.6}$$

Therefore, at large distances ($q_c r \gg 1$), $\chi(\boldsymbol{r})$ in 3D can be expressed as follows:

$$\chi(\boldsymbol{r}) \approx \frac{A\cos(q_c r)}{r^2} + \frac{B}{r^{6-N}}, \tag{D.7}$$

where A and B are constants. When $6 - N \leq 2$, i.e., $N \geq 4$, the second term in Eq. (D.7) dominates over the first term. Since the magnitude of the oscillating term is smaller than that of the monotonic decaying term, the oscillation of the range function mostly occurs at positive values. In contrast, for $N \leq 3$, the oscillating first term dominates. Therefore, the range function oscillates with a period $2\pi/q_c$, and its amplitude decays as $1/r^2$.

Similarly, for 2D, we find that when $4-N \leq \frac{3}{2}$, i.e., $N = 3, 4, \cdots$, the range function decays as $1/r^{4-N}$, while for $N = 1, 2$, it oscillates with a period $2\pi/q_{\rm c}$, and its amplitude decays as $1/r^{\frac{3}{2}}$. This result is consistent with Min *et al.* [158] for 2D gapless semimetals.

D.2 Effective RKKY coupling with the exponential disorder cutoff

From Eq. (6.9) in the main text, the normalized effective RKKY coupling with exponential damping is given by

$$\begin{aligned}
\frac{J_{\rm eff}(T)}{J_{\rm eff}^{(0)}} &= \int_0^{R/a} \tilde{r}^2 d\tilde{r} \tilde{\chi}(\boldsymbol{r}, T) \\
&+ \left(\int_0^{\infty} - \int_0^{R/a} \right) \tilde{r}^2 d\tilde{r} \tilde{\chi}(\boldsymbol{r}, T) e^{-\frac{r-R}{R}} \\
&= \int_0^{R/a} \tilde{r}^2 d\tilde{r} \tilde{\chi}(\boldsymbol{r}, T) \left(1 - e^{-\frac{r-R}{R}} \right) + F(T),
\end{aligned} \tag{D.8}$$

where $\tilde{r} = r/a$, $\tilde{\chi}(\boldsymbol{r}, T) = \chi(\boldsymbol{r}, T)/D_0$, and

$$F(T) \equiv \int_0^{\infty} \tilde{r}^2 d\tilde{r} \tilde{\chi}(\boldsymbol{r}, T) e^{-\frac{r-R}{R}}, \tag{D.9}$$

which can be rewritten as (see Eq. (6.623) in Ref. [161])

$$\begin{aligned}
F(T) &\equiv \int_0^{\infty} \tilde{r}^2 d\tilde{r} \tilde{\chi}(\boldsymbol{r}, T) e^{-\frac{r-R}{R}} \\
&= \int_0^{q_{\rm c} a} \frac{\tilde{q}^2 d\tilde{q}}{2\sqrt{2\tilde{q}\pi^3}} \frac{2e\,(2q)^{\frac{1}{2}}\,\Gamma(2)}{R\sqrt{\pi}\,(1/R^2 + q^2)^2} \tilde{\chi}(\boldsymbol{q}, T) \\
&= \int_0^{q_{\rm c} a} \frac{\tilde{q}^2 d\tilde{q}}{\pi^2} \frac{e\tilde{R}^3 \tilde{\chi}(\boldsymbol{q}, T)}{\left(1 + \tilde{q}^2 \tilde{R}^2\right)^2},
\end{aligned} \tag{D.10}$$

where $\tilde{q} = qa$, $\tilde{R} = R/a$, $\tilde{\chi}(\boldsymbol{q}, T) = \chi(\boldsymbol{q}, T)/D_1(a^{-1})$, and Γ is the gamma function.

Bibliography

[1] M. Z. Hasan and C. L. Kane, "Colloquium: topological insulators", Rev. Mod. Phys. **82**, 3045 (2010).

[2] L. Fu, "Topological crystalline insulators", Phys. Rev. Lett. **106**, 106802 (2011).

[3] A. A. Burkov, "Topological semimetals", Nature Materials **15**, 1145 (2016).

[4] N. Armitage, E. Mele, and A. Vishwanath, "Weyl and dirac semimetals in three-dimensional solids", Rev. Mod. Phys **90**, 015001 (2018).

[5] F. Schindler, A. M. Cook, M. G. Vergniory, Z. Wang, S. S. P. Parkin, B. A. Bernevig, and T. Neupert, "Higher-order topological insulators", Science Advances **4** (2018).

[6] C. Fang, M. J. Gilbert, X. Dai, and B. A. Bernevig, "Multi-weyl topological semimetals stabilized by point group symmetry", Phys. Rev. Lett. **108**, 266802 (2012).

[7] G. Rui, S. Zdenek, and P. Martin, "Black phosphorus rediscovered: from bulk material to monolayers", Angew. Chem. Int. Ed. **56**, 8052 (2017).

[8] A. Chaves, W. Ji, J. Maassen, T. Dumitrică, and T. Low, in *2d materials: properties and devices*, edited by P. Avouris, T. Low, and T. F. Heinz (Cambridge University Press, Cambridge, 2017), pp. 381–412.

[9] R. Roldán and A. Castellanos-Gomez, "A new bandgap tuning knob", Nature Photonics **11**, 407 (2017).

[10] J. Yang, R. Xu, J. Pei, Y. W. Myint, F. Wang, Z. Wang, S. Zhang, Z. Yu, and Y. Lu, "Optical tuning of exciton and trion emissions in monolayer phosphorene", Light: Science & Applications **4**, e312 (2015).

[11] D. Çakır, C. Sevik, and F. M. Peeters, "Significant effect of stacking on the electronic and optical properties of few-layer black phosphorus", Phys. Rev. B **92**, 165406 (2015).

[12] J. Quereda, P. San-Jose, V. Parente, L. Vaquero-Garzon, A. J. Molina-Mendoza, N. Agraït, G. Rubio-Bollinger, F. Guinea, R. Roldán, and A. Castellanos-Gomez, "Strong Modulation of Optical Properties in Black Phosphorus through Strain-Engineered Rippling", Nano Lett. **16**, 2931 (2016).

[13] Z. J. Xiang, G. J. Ye, C. Shang, B. Lei, N. Z. Wang, K. S. Yang, D. Y. Liu, F. B. Meng, X. G. Luo, L. J. Zou, Z. Sun, Y. Zhang, and X. H. Chen, "Pressure-Induced Electronic Transition in Black Phosphorus", Phys. Rev. Lett. **115**, 186403 (2015).

[14] B. Deng, V. Tran, Y. Xie, H. Jiang, C. Li, Q. Guo, X. Wang, H. Tian, S. J. Koester, H. Wang, J. J. Cha, Q. Xia, L. Yang, and F. Xia, "Efficient electrical control of thin-film black phosphorus bandgap", Nature Communications **8**, 14474 (2017).

[15] Y. Liu, Z. Qiu, A. Carvalho, Y. Bao, H. Xu, S. J. R. Tan, W. Liu, A. H. Castro Neto, K. P. Loh, and J. Lu, "Gate-Tunable Giant Stark Effect in Few-Layer Black Phosphorus", Nano Lett. **17**, 1970 (2017).

[16] L. L. Li, B. Partoens, and F. M. Peeters, "Tuning the electronic properties of gated multilayer phosphorene: a self-consistent tight-binding study", Phys. Rev. B **97**, 155424 (2018).

[17] J. Kim, S. S. Baik, S. H. Ryu, Y. Sohn, S. Park, B.-G. Park, J. Denlinger, Y. Yi, H. J. Choi, and K. S. Kim, "Observation of tunable band gap and anisotropic Dirac semimetal state in black phosphorus", Science **349**, 723 (2015).

[18] J. Kim, S. S. Baik, S. W. Jung, Y. Sohn, S. H. Ryu, H. J. Choi, B.-J. Yang, and K. S. Kim, "Two-dimensional dirac fermions protected by space-time inversion symmetry in black phosphorus", Phys. Rev. Lett. **119**, 226801 (2017).

[19] N. Ehlen, A. Sanna, B. V. Senkovskiy, L. Petaccia, A. V. Fedorov, G. Profeta, and A. Grüneis, "Direct observation of a surface resonance state and surface band inversion control in black phosphorus", Phys. Rev. B **97**, 045143 (2018).

[20] P. Di Pietro, M. Mitrano, S. Caramazza, F. Capitani, S. Lupi, P. Postorino, F. Ripanti, B. Joseph, N. Ehlen, A. Grüneis, A. Sanna, G. Profeta, P. Dore, and A. Perucchi, "Emergent dirac carriers across a pressure-induced lifshitz transition in black phosphorus", Phys. Rev. B **98**, 165111 (2018).

[21] G. Xu, H. Weng, Z. Wang, X. Dai, and Z. Fang, "Chern Semimetal and the Quantized Anomalous Hall Effect in $HgCr_2Se_4$", Phys. Rev. Lett. **107**, 186806 (2011).

[22] S.-M. Huang, S.-Y. Xu, I. Belopolski, C.-C. Lee, G. Chang, T.-R. Chang, B. Wang, N. Alidoust, G. Bian, M. Neupane, D. Sanchez, H. Zheng, H.-T. Jeng, A. Bansil, T. Neupert, H. Lin, and M. Z. Hasan, "New type of weyl semimetal with quadratic double weyl fermions", Proceedings of the National Academy of Sciences **113**, 1180 (2016).

[23] X. Wan, A. M. Turner, A. Vishwanath, and S. Y. Savrasov, "Topological semimetal and fermi-arc surface states in the electronic structure of pyrochlore iridates", Phys. Rev. B **83**, 205101 (2011).

[24] P. Hosur, S. A. Parameswaran, and A. Vishwanath, "Charge transport in weyl semimetals", Phys. Rev. Lett. **108**, 046602 (2012).

[25] R. R. Biswas and S. Ryu, "Diffusive transport in weyl semimetals", Phys. Rev. B **89**, 014205 (2014).

[26] Y. Ominato and M. Koshino, "Quantum transport in a three-dimensional weyl electron system", Phys. Rev. B **89**, 054202 (2014).

[27] B. Sbierski, G. Pohl, E. J. Bergholtz, and P. W. Brouwer, "Quantum transport of disordered weyl semimetals at the nodal point", Phys. Rev. Lett. **113**, 026602 (2014).

[28] B. Skinner, "Coulomb disorder in three-dimensional dirac systems", Phys. Rev. B **90**, 060202 (2014).

[29] Y. Ominato and M. Koshino, "Quantum transport in three-dimensional weyl electron system in the presence of charged impurity scattering", Phys. Rev. B **91**, 035202 (2015).

[30] S. Das Sarma, E. H. Hwang, and H. Min, "Carrier screening, transport, and relaxation in three-dimensional dirac semimetals", Phys. Rev. B **91**, 035201 (2015).

[31] N. Ramakrishnan, M. Milletari, and S. Adam, "Transport and magnetotransport in three-dimensional weyl semimetals", Phys. Rev. B **92**, 245120 (2015).

[32] B. Roy, R.-J. Slager, "Global phase diagram of a dirty weyl liquid and emergent superuniversality", Phys. Rev. X **8**, 031076 (2018).

[33] P. Goswami and A. H. Nevidomskyy, "Topological Weyl superconductor to diffusive thermal Hall metal crossover in the B phase of UPt_3", Phys. Rev. B **92**, 214504 (2015).

[34] S. Bera, J. D. Sau, and B. Roy, "Dirty weyl semimetals: stability, phase transition, and quantum criticality", Phys. Rev. B **93**, 201302 (2016).

[35] B. Sbierski, M. Trescher, E. J. Bergholtz, and P. W. Brouwer, "Disordered double weyl node: comparison of transport and density of states calculations", Phys. Rev. B **95**, 115104 (2017).

[36] Q. Chen and G. A. Fiete, "Thermoelectric transport in double-weyl semimetals", Phys. Rev. B **93**, 155125 (2016).

[37] S. Ahn, E. H. Hwang, and H. Min, "Collective modes in multi-weyl semimetals", Scientific Reports **6**, 34023 (2016).

[38] B. Q. Lv, H. M. Weng, B. B. Fu, X. P. Wang, H. Miao, J. Ma, P. Richard, X. C. Huang, L. X. Zhao, G. F. Chen, Z. Fang, X. Dai, T. Qian, and H. Ding, "Experimental discovery of weyl semimetal taas", Phys. Rev. X **5**, 031013 (2015).

[39] S.-Y. Xu, I. Belopolski, N. Alidoust, M. Neupane, G. Bian, C. Zhang, R. Sankar, G. Chang, Z. Yuan, C.-C. Lee, S.-M. Huang, H. Zheng, J. Ma, D. S. Sanchez, B. Wang, A. Bansil, F. Chou, P. P. Shibayev, H. Lin,

S. Jia, and M. Z. Hasan, "Discovery of a weyl fermion semimetal and topological fermi arcs", Science **349**, 613 (2015).

[40] N. W. Ashcroft and N. D. Mermin, *Solid State Physics*, Vol. 8 (Brooks Cole, 1976), p. 031076.

[41] J. Schliemann and D. Loss, "Anisotropic transport in a two-dimensional electron gas in the presence of spin-orbit coupling", Phys. Rev. B **68**, 165311 (2003).

[42] K. Výborný, A. A. Kovalev, J. Sinova, and T. Jungwirth, "Semiclassical framework for the calculation of transport anisotropies", Phys. Rev. B **79**, 045427 (2009).

[43] T. Ando, A. B. Fowler, and F. Stern, "Electronic properties of two-dimensional systems", Rev. Mod. Phys. **54**, 437 (1982).

[44] S. Das Sarma, S. Adam, E. H. Hwang, and E. Rossi, "Electronic transport in two-dimensional graphene", Rev. Mod. Phys. **83**, 407 (2011).

[45] G. B. Arfken, H. J. Weber, and F. E. Harris, *Mathematical methods for physicists*, 7th ed, Vol. 8 (Academic Press, 2012), p. 031076.

[46] A. H. Castro Neto, F. Guinea, N. M. R. Peres, K. S. Novoselov, and A. K. Geim, "The electronic properties of graphene", Rev. Mod. Phys. **81**, 109 (2009).

[47] S. Banerjee, R. R. P. Singh, V. Pardo, and W. E. Pickett, "Tight-binding modeling and low-energy behavior of the semi-dirac point", Phys. Rev. Lett. **103**, 016402 (2009).

[48] V. Pardo and W. E. Pickett, "Half-Metallic Semi-Dirac-Point Generated by Quantum Confinement in TiO_2/VO_2 Nanostructures", Phys. Rev. Lett. **102**, 166803 (2009).

[49] V. Pardo and W. E. Pickett, "Metal-insulator transition through a semi-Dirac point in oxide nanostructures: VO_2 (001) layers confined within TiO_2", Phys. Rev. B **81**, 035111 (2010).

[50] F. Xia, H. Wang, and Y. Jia, "Rediscovering black phosphorus as an anisotropic layered material for optoelectronics and electronics", Nature Communications **5**, 4458 (2014).

[51] A. Mishchenko, Y. Cao, G. L. Yu, C. R. Woods, R. V. Gorbachev, K. S. Novoselov, A. K. Geim, and L. S. Levitov, "Nonlocal response and anamorphosis: the case of few-layer black phosphorus", Nano Lett. **15**, 6991 (2015).

[52] T. Li, Z. Zhang, X. Li, M. Huang, S. Li, S. Li, and Y. Wu, "High field transport of high performance black phosphorus transistors", Applied Physics Letters **110**, 163507 (2017).

[53] Y. Y. Illarionov, M. Waltl, G. Rzepa, J.-S. Kim, S. Kim, A. Dodabalapur, D. Akinwande, and T. Grasser, "Long-term stability and reliability of black phosphorus field-effect transistors", ACS Nano **10**, 9543 (2016).

[54] J. Qiao, X. Kong, Z.-X. Hu, F. Yang, and W. Ji, "High-mobility transport anisotropy and linear dichroism in few-layer black phosphorus", Nature Communications **5**, 4475 (2014).

[55] Y. Liu, T. Low, and P. P. Ruden, "Mobility anisotropy in monolayer black phosphorus due to scattering by charged impurities", Phys. Rev. B **93**, 165402 (2016).

[56] Y. Liu and P. P. Ruden, "Temperature-dependent anisotropic charge-carrier mobility limited by ionized impurity scattering in thin-layer black phosphorus", Phys. Rev. B **95**, 165446 (2017).

[57] F. W. Han, W. Xu, L. L. Li, C. Zhang, H. M. Dong, and F. M. Peeters, "Electronic and transport properties of n-type monolayer black phosphorus at low temperatures", Phys. Rev. B **95**, 115436 (2017).

[58] M. Zare, B. Z. Rameshti, F. G. Ghamsari, and R. Asgari, "Thermoelectric transport in monolayer phosphorene", Phys. Rev. B **95**, 045422 (2017).

[59] P. Adroguer, D. Carpentier, G. Montambaux, and E. Orignac, "Diffusion of dirac fermions across a topological merging transition in two dimensions", Phys. Rev. B **93**, 125113 (2016).

[60] A. N. Rudenko and M. I. Katsnelson, "Quasiparticle band structure and tight-binding model for single- and bilayer black phosphorus", Phys. Rev. B **89**, 201408 (2014).

[61] D. J. P. de Sousa, L. V. de Castro, D. R. da Costa, J. M. Pereira, and T. Low, "Multilayered black phosphorus: from a tight-binding to a continuum description", Phys. Rev. B **96**, 155427 (2017).

[62] S. S. Baik, K. S. Kim, Y. Yi, and H. J. Choi, "Emergence of two-dimensional massless dirac fermions, chiral pseudospins, and berry's phase in potassium doped few-layer black phosphorus", Nano Lett. **15**, 7788 (2015).

[63] H. Doh and H. J. Choi, "Dirac-semimetal phase diagram of two-dimensional black phosphorus", 2D Materials **4**, 025071 (2017).

[64] G. Montambaux, F. Piéchon, J.-N. Fuchs, and M. O. Goerbig, "Merging of dirac points in a two-dimensional crystal", Phys. Rev. B **80**, 153412 (2009).

[65] G. Montambaux, F. Piéchon, J.-N. Fuchs, and M. O. Goerbig, "A universal hamiltonian for motion and merging of dirac points in a two-dimensional crystal", The European Physical Journal B **72**, 509 (2009).

[66] R. de Gail, J.-N. Fuchs, M. Goerbig, F. Piéchon, and G. Montambaux, "Manipulation of dirac points in graphene-like crystals", Physica B: Condensed Matter **407**, Proceedings of the International Workshop on Electronic Crystals (ECRYS-2011), 1948 (2012).

[67] M. P. Marder, *Condensed matter physics, 2nd edition*, Vol. 8 (John Wiley & Sons, Oct. 25, 2010), p. 031076, 982 pp.

[68] E. D. Siggia and P. C. Kwok, "Properties of electrons in semiconductor inversion layers with many occupied electric subbands. i. screening and impurity scattering", Phys. Rev. B **2**, 1024 (1970).

[69] S. Woo, E. H. Hwang, and H. Min, "Large negative differential transconductance in multilayer graphene: the role of intersubband scattering", 2D Materials **4**, 025090 (2017).

[70] S. Park, S. Woo, E. J. Mele, and H. Min, "Semiclassical Boltzmann transport theory for multi-Weyl semimetals", Phys. Rev. B **95**, 161113 (2017).

[71] S. Adam, E. H. Hwang, V. M. Galitski, and S. Das Sarma, "A self-consistent theory for graphene transport", Proceedings of the National Academy of Sciences **104**, 18392 (2007).

[72] Q. Li, E. H. Hwang, and S. Das Sarma, "Disorder-induced temperature-dependent transport in graphene: puddles, impurities, activation, and diffusion", Phys. Rev. B **84**, 115442 (2011).

[73] J. Jang, S. Ahn, and H. Min, "Optical conductivity of black phosphorus with a tunable electronic structure", arXiv:1811.07529 **8**, 031076 (2018).

[74] K. v. Klitzing, G. Dorda, and M. Pepper, "New method for high-accuracy determination of the fine-structure constant based on quantized hall resistance", Phys. Rev. Lett. **45**, 494 (1980).

[75] H.-J. Kim, K.-S. Kim, J.-F. Wang, M. Sasaki, N. Satoh, A. Ohnishi, M. Kitaura, M. Yang, and L. Li, "Dirac versus weyl fermions in topological insulators: adler-bell-jackiw anomaly in transport phenomena", Phys. Rev. Lett. **111**, 246603 (2013).

[76] K.-S. Kim, H.-J. Kim, and M. Sasaki, "Boltzmann equation approach to anomalous transport in a weyl metal", Phys. Rev. B **89**, 195137 (2014).

[77] H. Li, H. He, H.-Z. Lu, H. Zhang, H. Liu, R. Ma, Z. Fan, S.-Q. Shen, and J. Wang, "Negative magnetoresistance in Dirac semimetal Cd_3As_2", Nature Communications **7**, 10301 (2016).

[78] C.-L. Zhang, S.-Y. Xu, I. Belopolski, Z. Yuan, Z. Lin, B. Tong, G. Bian, N. Alidoust, C.-C. Lee, S.-M. Huang, T.-R. Chang, G. Chang, C.-H. Hsu, H.-T. Jeng, M. Neupane, D. S. Sanchez, H. Zheng, J. Wang, H. Lin, C. Zhang, H.-Z. Lu, S.-Q. Shen, T. Neupert, M. Zahid Hasan, and S. Jia, "Signatures of the adler-bell-jackiw chiral anomaly in a weyl fermion semimetal", Nature Communications **7**, 10735 (2016).

[79] X. Huang, L. Zhao, Y. Long, P. Wang, D. Chen, Z. Yang, H. Liang, M. Xue, H. Weng, Z. Fang, X. Dai, and G. Chen, "Observation of the chiral-anomaly-induced negative magnetoresistance in 3d weyl semimetal taas", Phys. Rev. X **5**, 031023 (2015).

[80] J. Xiong, S. K. Kushwaha, T. Liang, J. W. Krizan, M. Hirschberger, W. Wang, R. J. Cava, and N. P. Ong, "Evidence for the chiral anomaly in the Dirac semimetal Na_3Bi", Science **350**, 413 (2015).

[81] C.-Z. Li, L.-X. Wang, H. Liu, J. Wang, Z.-M. Liao, and D.-P. Yu, "Giant negative magnetoresistance induced by the chiral anomaly in individual Cd_3As_2 nanowires", Nature Communications **6**, 10137 (2015).

[82] C. Zhang, E. Zhang, W. Wang, Y. Liu, Z.-G. Chen, S. Lu, S. Liang, J. Cao, X. Yuan, L. Tang, Q. Li, C. Zhou, T. Gu, Y. Wu, J. Zou, and F. Xiu, "Room-temperature chiral charge pumping in dirac semimetals", Nature Communications **8**, 13741 (2017).

[83] Q. Li, D. E. Kharzeev, C. Zhang, Y. Huang, I. Pletikosić, A. Fedorov, R. Zhong, J. Schneeloch, G. Gu, and T. Valla, "Chiral magnetic effect in $ZrTe_5$", Nature Physics **12**, 550 (2016).

[84] F. Arnold, C. Shekhar, S.-C. Wu, Y. Sun, R. D. dos Reis, N. Kumar, M. Naumann, M. O. Ajeesh, M. Schmidt, A. G. Grushin, J. H. Bardarson, M. Baenitz, D. Sokolov, H. Borrmann, M. Nicklas, C. Felser, E. Hassinger, and B. Yan, "Negative magnetoresistance without well-defined chirality in the weyl semimetal tap", Nature Communications **7**, 11615 (2016).

[85] X. Yang, Y. Li, Z. Wang, Y. Zhen, and Z. an Xu, *Observation of negative magnetoresistance and nontrivial π berrys phase in 3d weyl semi-metal nbas*, 2015.

[86] H. Wang, C.-K. Li, H. Liu, J. Yan, J. Wang, J. Liu, Z. Lin, Y. Li, Y. Wang, L. Li, D. Mandrus, X. C. Xie, J. Feng, and J. Wang, "Chiral anomaly and ultrahigh mobility in crystalline $HfTe_5$", Phys. Rev. B **93**, 165127 (2016).

[87] E. Zhang, R. Chen, C. Huang, J. Yu, K. Zhang, W. Wang, S. Liu, J. Ling, X. Wan, H.-Z. Lu, and F. Xiu, "Tunable Positive to Negative Magnetoresistance in Atomically Thin WTe_2", Nano Lett. **17**, 878 (2017).

[88] S. Nishihaya, M. Uchida, Y. Nakazawa, K. Akiba, M. Kriener, Y. Kozuka, A. Miyake, Y. Taguchi, M. Tokunaga, and M. Kawasaki, "Negative magnetoresistance suppressed through a topological phase transition in $(Cd_{1-x}Zn_x)_3As_2$ thin films", Phys. Rev. B **97**, 245103 (2018).

[89] B. Wan, F. Schindler, K. Wang, K. Wu, X. Wan, T. Neupert, and H.-Z. Lu, "Theory for the negative longitudinal magnetoresistance in the quantum limit of kramers weyl semimetals", Journal of Physics: Condensed Matter **30**, 505501 (2018).

[90] Q. H. Wang, K. Kalantar-Zadeh, A. Kis, J. N. Coleman, and M. S. Strano, "Electronics and optoelectronics of two-dimensional transition metal dichalcogenides", Nature Nanotechnology **7**, 699 (2012).

[91] H. T. He, H. C. Liu, B. K. Li, X. Guo, Z. J. Xu, M. H. Xie, and J. N. Wang, "Disorder-induced linear magnetoresistance in (221) topological insulator Bi_2Se_3 films", Appl. Phys. Lett. **103**, 031606 (2013).

[92] S. Wiedmann, A. Jost, B. Fauqué, J. van Dijk, M. J. Meijer, T. Khouri, S. Pezzini, S. Grauer, S. Schreyeck, C. Brüne, H. Buhmann, L. W. Molenkamp, and N. E. Hussey, "Anisotropic and strong negative magnetoresistance in the three-dimensional topological insulator Bi_2Se_3", Phys. Rev. B **94**, 081302 (2016).

[93] L.-X. Wang, Y. Yan, L. Zhang, Z.-M. Liao, H.-C. Wu, and D.-P. Yu, "Zeeman effect on surface electron transport in topological insulator bi2se3 nanoribbons", Nanoscale **7**, 16687 (2015).

[94] O. Breunig, Z. Wang, A. A. Taskin, J. Lux, A. Rosch, and Y. Ando, "Gigantic negative magnetoresistance in the bulk of a disordered topological insulator", Nature Communications **8**, 15545 (2017).

[95] B. A. Assaf, T. Phuphachong, E. Kampert, V. V. Volobuev, P. S. Mandal, J. Sánchez-Barriga, O. Rader, G. Bauer, G. Springholz, L. A. de Vaulchier, and Y. Guldner, "Negative longitudinal magnetoresistance from the anomalous $N = 0$ landau level in topological materials", Phys. Rev. Lett **119**, 106602 (2017).

[96] H.-C. Chen, Z.-F. Lou, Y.-X. Zhou, Q. Chen, B.-J. Xu, S.-J. Chen, J.-H. Du, J.-H. Yang, H.-D. Wang, and M.-H. Fang, "Negative Magnetoresistance in Antiferromagnetic Topological Insulator $EuSn_2As_2$EuSn2As2 *", Chinese Physics Letters **37**, 047201 (2020).

[97] R. Singh, V. K. Gangwar, D. D. Daga, A. Singh, A. K. Ghosh, M. Kumar, A. Lakhani, R. Singh, and S. Chatterjee, "Unusual negative magnetoresistance in bi2se3-ysy topological insulator under perpendicular magnetic field", Appl. Phys. Lett. **112**, 102401 (2018).

[98] B. Bhattacharyya, B. Singh, R. P. Aloysius, R. Yadav, C. Su, H. Lin, S. Auluck, A. Gupta, T. D. Senguttuvan, and S. Husale, "Spin-dependent scattering induced negative magnetoresistance in topological insulator Bi_2Te_3 nanowires", Scientific Reports **9**, 7836 (2019).

[99] X. Dai, Z. Z. Du, and H.-Z. Lu, "Negative magnetoresistance without chiral anomaly in topological insulators", Phys. Rev. Lett. **119**, 166601 (2017).

[100] A. V. Andreev and B. Z. Spivak, "Longitudinal negative magnetoresistance and magnetotransport phenomena in conventional and topological conductors", Phys. Rev. Lett. **120**, 026601 (2018).

[101] H. Ishizuka and N. Nagaosa, "Robustness of anomaly-related magnetoresistance in doped weyl semimetals", Phys. Rev. B **99**, 115205 (2019).

[102] H.-Z. Lu and S.-Q. Shen, "Quantum transport in topological semimetals under magnetic fields", Frontiers of Physics **12**, 127201 (2017).

[103] J. Behrends and J. H. Bardarson, "Strongly angle-dependent magnetoresistance in weyl semimetals with long-range disorder", Phys. Rev. B **96**, 060201 (2017).

[104] H.-W. Wang, B. Fu, and S.-Q. Shen, "Intrinsic magnetoresistance in three-dimensional dirac materials with low carrier density", Phys. Rev. B **98**, 081202 (2018).

[105] B. Fu, H.-W. Wang, and S.-Q. Shen, "Quantum magnetotransport in massive dirac materials", Phys. Rev. B **101**, 125203 (2020).

[106] M.-X. Deng, G. Y. Qi, R. Ma, R. Shen, R.-Q. Wang, L. Sheng, and D. Y. Xing, "Quantum oscillations of the positive longitudinal magnetoconductivity: a fingerprint for identifying weyl semimetals", Phys. Rev. Lett. **122**, 036601 (2019).

[107] A. A. Burkov, "Chiral anomaly and transport in weyl metals", Journal of Physics: Condensed Matter **27**, 113201 (2015).

[108] A. A. Zyuzin and A. A. Burkov, "Topological response in weyl semimetals and the chiral anomaly", Phys. Rev. B **86**, 115133 (2012).

[109] D. Xiao, J. Shi, and Q. Niu, "Berry phase correction to electron density of states in solids", Phys. Rev. Lett. **95**, 137204 (2005).

[110] D. Xiao, "Berry phase modification to electron density of states and its applications", PhD thesis (University of Texas, 2007), p. 031076.

[111] D. Xiao, M.-C. Chang, and Q. Niu, "Berry phase effects on electronic properties", Rev. Mod. Phys. **82**, 1959 (2010).

[112] H. K. Pal and D. L. Maslov, "Necessary and sufficient condition for longitudinal magnetoresistance", Phys. Rev. B **81**, 214438 (2010).

[113] R. Lundgren, P. Laurell, and G. A. Fiete, "Thermoelectric properties of weyl and dirac semimetals", Phys. Rev. B **90**, 165115 (2014).

[114] Y. Gao, S. A. Yang, and Q. Niu, "Intrinsic relative magnetoconductivity of nonmagnetic metals", Phys. Rev. B **95**, 165135 (2017).

[115] M. A. Stephanov and Y. Yin, "Chiral kinetic theory", Phys. Rev. Lett. **109**, 162001 (2012).

[116] D. T. Son and N. Yamamoto, "Berry curvature, triangle anomalies, and the chiral magnetic effect in fermi liquids", Phys. Rev. Lett. **109**, 181602 (2012).

[117] D. T. Son and B. Z. Spivak, "Chiral anomaly and classical negative magnetoresistance of weyl metals", Phys. Rev. B **88**, 104412 (2013).

[118] V. A. Zyuzin, "Magnetotransport of weyl semimetals due to the chiral anomaly", Phys. Rev. B **95**, 245128 (2017).

[119] A. Sekine, D. Culcer, and A. H. MacDonald, "Quantum kinetic theory of the chiral anomaly", Phys. Rev. B **96**, 235134 (2017).

[120] J. C. Olson and P. Ao, "Nonequilibrium approach to bloch-peierls-berry dynamics", Phys. Rev. B **75**, 035114 (2007).

[121] K. Das and A. Agarwal, "Linear magnetochiral transport in tilted type-i and type-ii weyl semimetals", Phys. Rev. B **99**, 085405 (2019).

[122] R. M. A. Dantas, F. Peña-Benitez, B. Roy, and P. Surówka, "Magneto-transport in multi-weyl semimetals: a kinetic theory approach", Journal of High Energy Physics **2018**, 69 (2018).

[123] A. Johansson, J. Henk, and I. Mertig, "Chiral anomaly in type-i weyl semimetals: comprehensive analysis within a semiclassical fermi surface harmonics approach", Phys. Rev. B **99**, 075114 (2019).

[124] J. M. Ziman, *Electrons and phonons : the theory of transport phenomena in solids*, Vol. 8 (Clarendon Press Oxford University Press, Oxford New York, 2001), p. 031076.

[125] T. Thonhauser, D. Ceresoli, D. Vanderbilt, and R. Resta, "Orbital magnetization in periodic insulators", Phys. Rev. Lett. **95**, 137205 (2005).

[126] D. Ceresoli, T. Thonhauser, D. Vanderbilt, and R. Resta, "Orbital magnetization in crystalline solids: multi-band insulators, chern insulators, and metals", Phys. Rev. B **74**, 024408 (2006).

[127] I. Souza and D. Vanderbilt, "Dichroic f-sum rule and the orbital magnetization of crystals", Phys. Rev. B **77**, 054438 (2008).

[128] W. Yao, D. Xiao, and Q. Niu, "Valley-dependent optoelectronics from inversion symmetry breaking", Phys. Rev. B **77**, 235406 (2008).

[129] G. Sundaram and Q. Niu, "Wave-packet dynamics in slowly perturbed crystals: gradient corrections and berry-phase effects", Phys. Rev. B **59**, 14915 (1999).

[130] S. Woo, S. Min, and H. Min, "Manuscript in preparation", Phys. Rev. X **8**, 031076 (2021).

[131] S. Park, S. Woo, and H. Min, "Semiclassical boltzmann transport theory of few-layer black phosphorus in various phases", 2D Materials **6**, 025016 (2019).

[132] S. Kim, S. Woo, and H. Min, "Vertex corrections to the dc conductivity in anisotropic multiband systems", Phys. Rev. B **99**, 165107 (2019).

[133] T. Kawamura and S. Das Sarma, "Phonon-scattering-limited electron mobilities in $Al_xGa_{1-x}As$/GaAs heterojunctions", Phys. Rev. B **45**, 3612 (1992).

[134] A. Bansil, H. Lin, and T. Das, "Colloquium: topological band theory", Rev. Mod. Phys **88**, 021004 (2016).

[135] A. A. Burkov, M. D. Hook, and L. Balents, "Topological nodal semimetals", Phys. Rev. B **84**, 235126 (2011).

[136] A. A. Burkov and L. Balents, "Weyl semimetal in a topological insulator multilayer", Phys. Rev. Lett. **107**, 127205 (2011).

[137] H.-R. Chang, J. Zhou, S.-X. Wang, W.-Y. Shan, and D. Xiao, "RKKY interaction of magnetic impurities in dirac and weyl semimetals", Phys. Rev. B **92**, 241103(R) (2015).

[138] M. V. Hosseini and M. Askari, "Ruderman-kittel-kasuya-yosida interaction in weyl semimetals", Phys. Rev. B **92**, 224435 (2015).

[139] Y. Sun and A. Wang, "RKKY interaction of magnetic impurities in multi-weyl semimetals", Journal of Physics: Condensed Matter **29**, 435306 (2017).

[140] R. Yu, W. Zhang, H.-J. Zhang, S.-C. Zhang, X. Dai, and Z. Fang, "Quantized anomalous hall effect in magnetic topological insulators", Science **329**, 61 (2010).

[141] D. Kurebayashi and K. Nomura, "Weyl semimetal phase in solid-solution narrow-gap semiconductors", Journal of the Physical Society of Japan **83**, 063709 (2014).

[142] Y. Araki and K. Nomura, "Spin textures and spin-wave excitations in doped dirac-weyl semimetals", Phys. Rev. B **93**, 094438 (2016).

[143] J. Zhou and H.-R. Chang, "Dynamical correlation functions and the related physical effects in three-dimensional weyl/dirac semimetals", Phys. Rev. B **97**, 075202 (2018).

[144] A. Thakur, K. Sadhukhan, and A. Agarwal, "Dynamic current-current susceptibility in three-dimensional dirac and weyl semimetals", Phys. Rev. B **97**, 035403 (2018).

[145] Y. Ominato and K. Nomura, "Spin susceptibility of three-dimensional dirac-weyl semimetals", Phys. Rev. B **97**, 245207 (2018).

[146] M. A. Ruderman and C. Kittel, "Indirect exchange coupling of nuclear magnetic moments by conduction electrons", Phys. Rev. **96**, 99 (1954).

[147] T. Kasuya, "A theory of metallic ferro- and antiferromagnetism on zener's model", Progress of Theoretical Physics **16**, 45 (1956).

[148] K. Yosida, "Magnetic properties of cu-mn alloys", Phys. Rev. **106**, 893 (1957).

[149] C. Kittel, "Solid state physics", in, Vol. 22, edited by F. S. D. T. H. Ehrenreich (Academic, New York, 1969) Chap. Indirect Exchage Interactions in Metals, p. 031076.

[150] H. Min and A. H. MacDonald, "Electronic structure of multilayer graphene", Progress of Theoretical Physics Supplement **176**, 227 (2008).

[151] H. Min and A. H. MacDonald, "Chiral decomposition in the electronic structure of graphene multilayers", Phys. Rev. B **77**, 155416 (2008).

[152] K. Kobayashi, T. Ohtsuki, K.-I. Imura, and I. F. Herbut, "Density of states scaling at the semimetal to metal transition in three dimensional topological insulators", Phys. Rev. Lett. **112**, 016402 (2014).

[153] J. H. Pixley, D. A. Huse, and S. Das Sarma, "Rare-region-induced avoided quantum criticality in disordered three-dimensional dirac and weyl semimetals", Phys. Rev. X **6**, 021042 (2016).

[154] J. H. Pixley, D. A. Huse, and S. Das Sarma, "Uncovering the hidden quantum critical point in disordered massless dirac and weyl semimetals", Phys. Rev. B **94**, 121107 (2016).

[155] S. D. Sarma and E. H. Hwang, "Charge transport in gapless electron-hole systems with arbitrary band dispersion", Phys. Rev. B **91**, 195104 (2015).

[156] D. J. Priour, E. H. Hwang, and S. D. Sarma, "Disordered RKKY lattice mean field theory for ferromagnetism in diluted magnetic semiconductors", Phys. Rev. Lett. **92**, 117201 (2004).

[157] D. J. Priour, E. H. Hwang, and S. D. Sarma, "Quasi-two-dimensional diluted magnetic semiconductor systems", Phys. Rev. Lett. **95**, 037201 (2005).

[158] H. Min, E. H. Hwang, and S. Das Sarma, "Ferromagnetism in chiral multilayer two-dimensional semimetals", Phys. Rev. B **95**, 155414 (2017).

[159] C. Kittel, *Introduction to solid state physics*, 8th ed., Vol. 8 (Wiley, New Jersey, 2005), p. 031076.

[160] S. D. Sarma, E. H. Hwang, and A. Kaminski, "Temperature-dependent magnetization in diluted magnetic semiconductors", Phys. Rev. B **67**, 155201 (2003).

[161] I. S. Gradshteyn and I. M. Ryzhik, *Tables of integrals, series and products*, edited by D. Zwillinger, 8th ed., Vol. 8 (Academic, New York, 2015), p. 031076.

국문초록

위상적 준금속은 많은 흥미로운 성질을 가진 새로운 물질으로서, 최근까지 응집물질물리학 연구의 화제의 중심이 되어 왔다. 이는 전자띠가 만나는 지점에서 나타나는 준입자 활성이 드루드 자유전자 모델을 따르지 않기 때문이기도 하다. 그리고 위상적 준금속은 위상적인 성질 덕분에 그러한 준입자 활성이 외부 섭동에 대하여 안정적이기 때문에 여기서 나오는 일반적이지 않은 활성에 대한 다양한 물리적 현상을 시험해보기 위한 훌륭한 시험대이기도 하다. 이러한 동기를 가지고, 해당 학위논문은 디락 물질에서 준고전적인 전자 수송 이론 및 전자 스핀에 의하여 매개되는 자화 현상에 대해 다룬다.

먼저 우리는 본 학위논문 전반에 걸쳐 사용되는 비등방적이고 다층전자띠 물질에 적용가능한 준고전적인 볼츠만 수송 이론을 유도한다.

그런 다음 우리는 다중 바일 준금속과 다층 흑린의 전자수송현상을 앞서 유도한 비등방, 다층전자띠 물질에 적용가능한 볼츠만 수송 이론을 통하여 연구한다. 다중 바일 준금속은 비등방적인 전자띠 구조를 가진 위상적 준금속으로서 (한 쪽 방향으로는 선형, 나머지 방향으로는 비선형적인 관계를 가진다) 카이랄 전하 값이 1보다 큰 물질이다. 흑린은 통상적으로는 반도체 물질이나, 최근 연구로 전자띠 간격을 자유롭게 조절 가능하며 이에 따른 여러 가지 상을 가질 수 있음이 밝혀지게 되었다 (부도체 상, 반디락 상, 디락 상). 우리는 이러한 물질들을 비등방적, 다층띠 물질에 적용가능한 볼츠만 수송 이론을 통하여 연구하였으며, 각 물질들의 특징적인 카이랄 전하값, 전자띠 구조, 그리고 전자띠 간격의 부호에 따라서 전하 밀도 및 온도에 따른 전기 전도도의 변화를 계산하였다.

우리는 또한 자기장이 준고전적인 전자 수송에 미치는 영향에 대해서도 연구하였다. 즉 외부 자기장이 물질의 베리곡률과 결합되어 발생하는 비등방성이 전자 수송에 미치는 영향을 조사하였다.

마지막으로, 우리는 등방적인 3차원 카이랄 준금속 예시 물질에서 루더만-키텔-카즈야-요시다 (RKKY) 상호작용을 연구하였다. 우리는 성기게 배치된 자기적 불순물들이 전자의 스핀에 의하여 매개되는 자화 현상및 자화 감수성, 임계 온도를 멱수에 대하여 계산하였고, 멱법칙에 관계없이 해당 물질은 강자성을 띤다는 사실을 발견하였다.

주요어: 전기 전도도, 준고전적 볼츠만 수송 이론, 다층 흑린, 바일 준금속, 다중 바일 준금속, RKKY 상호작용
학번: 2014-22366

Acknowledgements

My deepest gratitude goes to my advisor Hongki Min, who has always been hugely supportive and understanding, and has done his best to make me a proper physicist. He motivated me to strengthen my advantages and overcome my shortcomings with countless efforts, and it has been a great honor and privilege to be able to be under his supervision.

I also would like to thank my other committee members, Prof. Cheol-Hwan Park, Prof. Changyoung Kim, Prof. Bohm Jung Yang and Prof. Euyheon Hwang from SKKU, for their insightful comments and encouragements.

My colleagues, graduated seniors and juniors, Yunsu Jang, Seongjin Ahn, Seungchan Woo, Changhee Lee, Chiho Yoon, Jiho Jang, Sunghoon Kim, Taehyeok Kim, and Jeong Hyeon Seo, who provided valuable discussions and kept my company during my time in the grad school, are the ones that I am sincerely thankful too.

Finally, I want to appreciate all my friends and family members. Especially my parents, who have supported my journey through the graduate school in so many ways. I do not think that I would have made it through the doctoral research period without them. No amount of words could possibly be enough to express how grateful I am.